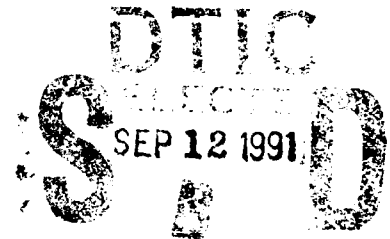WL-TR-91-3065

AD-A240 256

‖‖‖‖‖‖‖‖‖‖‖‖‖

EXPERIMENTAL INVESTIGATION OF THE EFFECTS OF
BLOWING ON BURSTING OF STRAKE VORTICES

Robert Allen Roach
John M. Kulham

West Virginia University
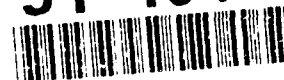Mechanical and Aerospace Engineering Department
Morgantown WV 26506-6101

July 1991

Final report for period July 1989 - Apr 1991
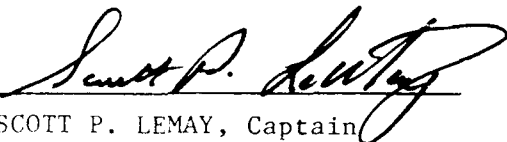
DTIC
SEP 12 1991

91-10436

‖‖‖‖‖‖‖‖‖‖‖‖‖

NOTICE

When Government drawings, specifications, or other data are used for any purpose other than in connection with a definitely Government-related procurement, the United States Government incurs no responsibility or any obligation whatsoever. The fact that the government may have formulated or in any way supplied the said drawings, specifications, or other data, is not to be regarded by implication, or otherwise in any manner construed, as licensing the holder, or any other person or corporation; or as conveying any rights or permission to manufacture, use, or sell any patented invention that may in any way be related thereto.

This report is releasable to the National Technical Information Service (NTIS). At NTIS, it will be available to the general public, including foreign nations.

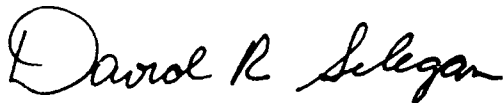This technical report has been reviewed and is approved for publication.

SCOTT P. LEMAY, Captain
Program Manager
Airframe & Aerodynamics Group

DENNIS SEDLOCK
Chief
Aerodynamics & Airframe Branch

FOR THE COMMANDER

DAVID R. SELEGAN
Actg Chief
Aeromechanics Division

If your address has changed, if you wish to be removed from our mailing list, or if the addressee is no longer employed by your organization please notify WL/FIMM , WPAFB, OH 45433- 6553 to help us maintain a current mailing list.

Copies of this report should not be returned unless return is required by security considerations, contractual obligations, or notice on a specific document.

REPORT DOCUMENTATION PAGE

1. AGENCY USE ONLY *(Leave blank)*	2. REPORT DATE July 1991	3. REPORT TYPE AND DATES COVERED Final Report 12 Jul 89 – 22 Apr 91

4. TITLE AND SUBTITLE	5. FUNDING NUMBERS
Experimental Investigation of the Effects of Blowing on Bursting of Strake Vortices	C-F33615-89-C-3001 PE-62201F PR 2404 TA 10 WU B6

6. AUTHOR(S)

Robert Allen Roach
John M. Kulhman

7. PERFORMING ORGANIZATION NAME(S) AND ADDRESS(ES) West Virginia University Mechanical and Aerospace Engineering Department Morgantown WV 26506-6101	8. PERFORMING ORGANIZATION REPORT NUMBER N/A

9. SPONSORING/MONITORING AGENCY NAME(S) AND ADDRESS(ES) Capt Scott P. LeMay (513) 255-3413 Flight Dynamics Directorate (WL/FIMM) Wright Laboratory Wright-Patterson AFB, OH 45433-6553	10. SPONSORING/MONITORING AGENCY REPORT NUMBER WL-TR-91-3065

11. SUPPLEMENTARY NOTES

None

12a. DISTRIBUTION/AVAILABILITY STATEMENT Approved for public release; distribution is unlimited.	12b. DISTRIBUTION CODE

13. ABSTRACT *(Maximum 200 words)*

Laser light sheet flow visualization and laser Doppler Anememetry (LDA) have been utilized to study the effects of pneumatic jet blowing on the breakdown and coupling locations of the strake and wing vortices generated over a generic fighter aircraft model with 55 degree sweep cropped delta wing planform fitted with forebody strakes. Experiments were conducted at low speed (15 m/sec), corresponding to a chord Reynolds number of 270,000, over an angle of attack range of 20 to 36 degrees.

Flow visualization has been used to determine jet blowing locations and nozzle configurations which have the maximum beneficial effects of delaying both vortex breakdown and coupling of the strake and wing vortices. Significant reductions were observed both in vortex coupling interaction and in strake vortex breakdown at a blowing coefficient referenced to the wing area of 0.016. The LDA data indicated increases in the mean axial velocity above the vortices and increased turbulent velocities due to jet blowing.

14. SUBJECT TERMS Delta Wing, Vortex Flow, Vortex Flow Control, Jet Blowing, Vortex Interaction, Laser Doppler, Anemometer, Laser Light Sheet, Pneumatic			15. NUMBER OF PAGES 176
			16. PRICE CODE

17. SECURITY CLASSIFICATION OF REPORT Unclassified	18. SECURITY CLASSIFICATION OF THIS PAGE Unclassified	19. SECURITY CLASSIFICATION OF ABSTRACT Unclassified	20. LIMITATION OF ABSTRACT DTIC users

FOREWORD

EXPERIMENTAL INVESTIGATION OF THE EFFECTS OF BLOWING ON
BURSTING OF STRAKE VORTICES

The following final report has been prepared under the sponsorship of the

Wright Laboratories/FDD under Contract F33615-89-C-3001, Capt Scott P. LeMay,

Technical Monitor. This report consists of the Master's thesis prepared by

the first author, under the direction of the second author.

ACKNOWLEDGEMENTS

TABLE OF CONTENTS

APPENDIX

LIST OF FIGURES

LIST OF TABLES

SYMBOLS

ENGLISH LETTERS

b	Wing span
C	Root chord of wing
e	Natural exponential function
f	Focal length of transmitting lens
$\dot{m}$	Mass flow rate
P	Pressure
q	Freestream dynamic pressure
S	Surface area of wing
T	Temperature
V	Velocity
x	Coordinate axis
X	Distance along wing chord
y	Coordinate axis
z	Coordinate axis

GREEK LETTERS

λ	Wavelength of laser light; also taper ratio
Λ_{LE}	Wing leading edge sweep angle
φ	Angle between laser beams of three component LDA

SUBSCRIPT LETTERS

c_r	Wing root chord
c_t	Wing tip chord
c_m	Wing mean chord
c_μ	Blowing coefficient
d_e-2	Dimension of the edges of measuring volume

D_e-2	Diameter of laser beam entering transmitting lens
d_f	Fringe spacing in probe volume
d_m	Measuring volume dimension
f_D	Doppler frequency of scattered laser light
l_m	Measuring volume dimension
S_{ref}	Wing surface reference area
V_J	Velocity of blowing jet

1.0 INTRODUCTION

The ability to predict and control the performance of aircraft at high angles of attack has been of particular importance in recent years. Many modern fighter aircraft are designed to generate a flow field which is characterized by sets of counter rotating vortices above the lifting surfaces at high angles of attack. These vortices produce large increments in the lift on the aircraft, and are capable of augmenting the maneuverability of an aircraft when conventional control surfaces have become ineffective. Vortices are created when fluid on the lower surface of the wing flows outward toward the sharp leading edge and separates, forming a rolled up vortex sheet with high vorticity over the upper side of the wing. Cropped, delta wing planforms with leading edge extensions or highly swept strakes have become very common on modern fighter aircraft due to their ability to create vortices over the upper surface of the wing.

The lift produced by a vortical flow field is limited by breakdown or bursting of the vortices, which often occurs asymmetrically. Vortex breakdown or bursting is characterized by a decrease in the axial velocity in the core of the vortex, a sudden expansion in the cross sectional area, and a related reduction in swirl velocity of the vortex. Breakdown of vortices results in a large loss of lift and can create severe stability problems for an aircraft. It has been shown that blowing a jet of air spanwise along the top surface of the wing

can delay vortex breakdown and can result in a restoration of the vortical flow field.

The present investigation studies the effectiveness of pneumatic blowing in controlling the breakdown of a vortical flow. A generic fighter aircraft model with a 55 degree sweep, cropped delta wing planform in conjunction with forebody strakes in a low, subsonic flow has been used to generate the desired vortical flow. Flow visualization and laser Doppler anemometry have been used to determine the details of the vortex flow velocity field. Comparisons have been made between vortex behavior without blowing and of vortex behavior with blowing. This comparison focuses on how blowing alters the vortical flow field by delaying bursting and by delaying or eliminating the interaction of the vortices created by the forebody strake and wing leading edge.

2.0 LITERATURE REVIEW

There have been investigations of vortex breakdown behavior over highly swept delta wing planforms for over three decades. Polhamus (1) and (2) was the first to develop an analytical model to predict the lift increment, drag due to lift, and pitching moment of delta wings. This method used a leading edge suction analogy for vortex lift, and showed the importance of vortex lift in predicting the drag and lift characteristics of delta wings at high angles of attack. Many experimental studies have verified Polhamus' analytical method, but many have also shown that the prediction of lift over delta wings is severely limited by vortex breakdown.

An article in Aviation Week and Space Technology in 1989 by Scott (3) stressed the recent importance and priority placed on high angle of attack research. This article also discussed some of the recent and future studies being done by NASA on an F/A-18 aircraft in the high angle of attack regime. Recent studies on this aircraft have shown that at an angle of attack of 35 degrees, most of the aircraft's lift comes from the fuselage and leading edge extension. Future studies will deal with the addition of a strake on each side of the nose/forebody area in hopes that stable flight with the F/A-18 can be achieved up to angles of attack of 70 and 80 degrees. Also, vortex blowing and suction will be used to attempt to enhance the yaw control at high angles of attack.

The effect of combining a delta wing with a leading edge

extension on vortex breakdown has been widely investigated. Most of these studies focused their attention on using flow visualization and force measurements to document the effect of varying flight parameters such as angle of attack and sideslip on the position of the vortices and location of the breakdown of the vortices.

Wentz (4) in 1968 conducted systematic, low speed wind tunnel investigations of vortex breakdown on a number of different wing planforms. These planforms included 13 different, uncambered and untwisted delta wings with leading edge sweeps ranging from 45 to 85 degrees: two double delta planforms with an aft panel sweep of 65 degrees and forward panel sweeps of 75 and 80 degrees; a diamond wing; an arrow wing; and an ogee wing, such as that used on the Concorde supersonic transport. Among the findings of this investigation was that the forward progression of vortex breakdown for a given wing proceeds rapidly at first and then more slowly near the apex of the wing. Apex sweep was found to be more important than trailing edge geometry in determining initial breakdown, and the installation of strakes was shown to have a dominant influence on breakdown behavior. Polhamus' leading-edge suction analogy for predicting lift coefficients was also verified for wings of medium sweep operating below the critical angle for initial breakdown.

Wentz and Kohlman (5) investigated vortex breakdown on sharp-edged delta wings and modified delta wings with leading edge sweep angles from 45 to 85 degrees in a subsonic flow of

190 feet per second. Along with verifying Polhamus' leading edge suction analogy, it was again shown that apex sweep has a dominant influence on the location of vortex breakdown. Also, it was shown that radome strakes, ie, circular arc contour leading edge, with 75 and 80 degree sweeps in conjunction with a 65 degree sweep delta wing have a stabilizing influence on the wing vortex.

An assessment of the effect of sideslip on the vortex flow field interactions at high angle of attack was performed by Erickson and Gilbert (6) in 1983. This experimental investigation on a fighter type model with a leading edge extension showed that the flow field became more complex in sideslip. A reduction in wing flow separation and improved lateral stability was shown with radome strakes installed on the model, but penalties in yaw instability and the generation of lateral oscillations were also revealed.

A study examining the influence of forebody cross section on the position of wing vortex burst with and without sideslip was completed by Hall (7) in 1986. A 55 degree sweep, cropped delta wing model with three different cross sections for the fuselage was examined. The cross sections consisted of a circular cross section, a 7.5 degree chine, and a 90 degree chine cross section. A delay of the wing vortex burst location was shown with the chine cross sections, with the 7.5 degree chine being the most effective. Large asymmetries in the vortical flow were observed in sideslip.

Erickson and Brandon (8) examined the nonlinear aerodynamic

5

and stability characteristics of a fighter type configuration featuring a chine shaped forebody coupled to a slender, 60 degree sweep, cropped delta wing. Among the findings of this investigation was the observation that interaction of the chine and wing vortices promoted large nonlinear lift increments at moderate and high angles of attack, along with increased pitch instability. With the model in sideslip, the chine forebody developed a concentrated vortex along the windward side which induced large restoring yawing moments. A basis for future studies with passive and/or active "effectors" positioned in the region of the chine/wing junction was also established.

Two investigations of vortex flow aerodynamics over a generic research fighter configuration having a 55 degree sweep, cropped delta wing with chine-like strakes were completed by Erickson, Rogers, Schreiner, and Lee (9 and 10). These investigations had a Mach number range of 0.4 to 1.10. With the location of the forebody strakes slightly above and decoupled from the wings, the strake vortex energized the wing leading edge vortex, and no interaction between the vortices was present up to an angle of attack of 27 degrees. However, when the forebody strakes were located in the wing plane and faired into the wing leading edge, vortex interaction did occur below 27 degrees model angle of attack. Interaction of the vortices resulted in a large lift increment and lower induced drag but increased the pitch instability of the model. The second investigation used sideslip angles of -15 to 15 degrees. In sideslip, the highly coupled vortices were prone to core

trajectory and breakdown asymmetries which resulted in a loss of lateral and directional stability.

Erickson, Schreiner, and Rogers (11) in 1989 investigated vortex flows at subsonic, transonic, and supersonic speeds for a 65 degree sweep, cropped delta wing with and without a leading edge extension up to an angle of attack of 24 degrees. The subsonic speeds investigated included freestream Mach numbers of 0.4, 0.6, and 0.8. A stabilization of the wing vortex in the presence of the leading edge extension vortical flow eliminated the discontinuities in the lift, drag, and pitching moment curves that occurred on the wing alone configuration. For the angle of attack range where interaction of the vortex cores was observed, the wing vortex moved upward and inboard due to the leading edge extension vortex which caused an extensive region of separated and reversed flow near the wing tip. This separation resulted in reduced effectiveness of the lateral control surfaces. Also, vortex breakdown was shown to cause a reduction in lift and an unstable pitching moment

There have also been several experimental investigations focusing on the effect of blowing on vortical flows. These studies concentrate on the ability of blowing a jet spanwise or along the leading edge, parallel to the surface of the wing, to augment or control the vortical flow field. For these investigations, the magnitude of jet blowing was characterized by the blowing, or momentum, coefficient which was defined as the ratio of the blowing jet momentum to the freestream

momentum as referenced to the wing area.

In 1976, Campbell (12) evaluated the aerodynamic effects associated with blowing a jet spanwise over a wing upper surface in a direction parallel to the leading edge. A series of wing planforms were tested at a freestream Mach number of 0.2. The planforms consisted of delta, arrow, and diamond wings at leading edge sweep angles of 30 and 45 degrees. The full vortex sectional lift as estimated by Polhamus' leading edge suction analogy was achieved at inboard parts of the wing with small blowing coefficients. To achieve full vortex section lift at increased span distances larger blowing coefficients were necessary. A decrease in the wing leading edge sweep increased the vortex lift increment created by blowing. In conclusion, blowing was shown to cause large lift increments at high angles of attack, to improve the drag polars, and to extend the linear pitching moment to higher lifts.

Skow and Peake (13) used asymmetric air injection to control the forebody vortex orientation. Blowing was shown to induce an acceptable level of departure/spin recovery of a fighter type aircraft. Vortex shedding in the asymmetric vortex wake created by a slender conical forebody was prevented by injecting a small quantity of air from a single orifice near the nose.

Visser, Nelson, and Ng (14) conducted an experimental investigation to determine the effects on blowing spanwise on leading edge vortices. For this investigation, the desired

vortical flow field was generated by a 70 degree sweep, sharp edged delta wing, using both half and full span models. The optimal blowing position was found to be parallel and close to the leading edge, and tangential to the wing upper surface. Blowing at this position increased lift by 20 percent and drag by 17 percent. Visser, Nelson, and Ng postulated that the optimum blowing position was a function of vortex core position and that blowing possibly weakens the vortex strength. There were also significant differences between their full span and half span model results.

Experimental investigations studying the effects of spanwise blowing over a delta wing planform fitted with a strake or leading edge extension have also been performed to assess any alterations of the vortical flow field. The addition of a leading edge extension to an aircraft at high angles of attack leads to the production of an additional pair of counter rotating vortices to the vortical flow. These additional vortices shed from the leading edge extension tend to become coupled with the existing vortices shed from the leading edge of the wing. The coupling of the wing leading edge and leading edge extension vortices has been shown to cause premature vortex breakdown. In an investigation of a vortex flow field generated by a delta wing in conjunction with a leading edge extension, the focus of the study now also has to document the effects of spanwise blowing on the coupling of the wing leading edge and leading edge extension vortices.

An investigation of blowing a jet of high pressure air over

a swept wing surface in a direction parallel to the leading edge to verify any enhancement of the vortex system was conducted by Bradley and Wray (15). Three wing planforms were tested: a 60 degree sweep delta wing; a 40 degree sweep, cropped delta wing; and a 40 degree sweep, cropped delta wing in conjunction with an 80 degree sweep forebody strake. These planforms were tested in a subsonic flow with a freestream Mach number of 0.3. Blowing coefficients were ranged from 0.0 to 0.09. Among the findings of this investigation was that blowing over the top surface of the wing was best at low angles of attack, and blowing over the surface of the strake was best at high angles of attack. The best blowing location was at 0.10 chord on the wing, parallel to the leading edge. Blowing was found to delay vortex breakdown, improve the lift and drag polars where vortex breakdown occurs, and to increase the effective aspect ratio since the vortex was forced outboard from the wing tip. Also, it was found that for a low sweep wing, blowing aids in the development of the wing leading edge vortex system.

Bradley, Whitten, and Wray (16) explored the magnitude of possible enhancement of the leading edge vortex system by blowing. A model with a 40 degree sweep, cambered and twisted wing with a leading edge extension and leading edge flaps was used for this investigation. Two freestream Mach numbers of 0.3 and 0.75 were tested, with blowing coefficients ranging from 0.0 to 0.17. Blowing at a nozzle sweep of 5 to 10 degrees less than the leading edge sweep was found to be favorable in

augmenting the vortex flow. Blowing resulted in an improvement in the lift and drag polars, and gains in lift when the wing was influenced by flow separation. It was noted that when the leading edge flap was deflected the leading edge flow remained attached to the wing surface. As also shown in other investigations, blowing is ineffective unless the flow is separated from the wing surface.

Erickson (17) investigated the spanwise blowing concept and its ability to provide improved aerodynamic characteristics. In a flow with a freestream Mach number of 0.18, a 32 degree sweep wing with a leading edge extension was tested. Blowing was located at the junction of the wing and the leading edge extension at a sweep angle of 55 degrees. Blowing coefficients ranged from 0.02 to 0.12. Improvements in the aircraft flight characteristics created by blowing included: vortex-induced lift increments, improved drag polars, extension of linear pitching moments to high lift, and improvements in the lateral/directional characteristics by delaying wing stall and maintaining vertical tail effectiveness. Again it was noted that deflection of the leading edge flap and the subsequent reattachment of the flow on the surface of the wing delayed blowing-induced benefits.

Malcolm and Skow (18) conducted an experimental investigation on a generic fighter model to explore vortex manipulation as an effective means of enhancing aircraft control. This investigation used blowing in the upstream and downstream directions, and wing sweeps of 30, 40, 50, and 60

degrees in conjunction with several different sizes and shapes of leading edge extensions to evaluate their potential as flow control devices in the medium to high angle of attack range. It was found that modifiers to the apex of the leading edge extension had very little effect on the vortex position or breakdown location. Blowing on the leading edge extension was also ineffectual near the apex of the leading edge extension, but forebody blowing was effective in switching the forebody vortex asymmetry when applied at a radial position of 150 degrees from the windward stagnation line and perpendicular to the surface. Increasing the leading edge extension area was found to produce stronger leading edge extension vortices with breakdown positions located farther aft. Also, interaction of the leading edge extension and wing vortices, and the resulting breakdown locations were both strong functions of the leading edge extension size and wing sweep angle. In conclusion, vortex control was found to be feasible to pursue as a supplementary control mechanism.

The effects of blowing on chine/wing vortex interaction was investigated by LeMay and Rogers (19) in 1990. This investigation used a generic fighter configuration having a 55 degree sweep, cropped delta wing in conjunction with chine-like strakes to generate the desired flow field. This model was a smaller-scale model similar to that studied by Erickson, Rogers, Schreiner, and Lee (9 and 10). Blowing coefficients used for this study ranged from 0 to 0.03, and the model angle of attack ranged from 9 to 36 degrees, with and without a

sideslip angle of 5 degrees. Interaction of the vortices was shown to be initially favorable, delaying bursting of wing vortex up to 21 degrees angle of attack, and delaying bursting of the chine vortex up to 24 degrees. As the angle of attack was increased, the vortex interaction became unstable and burst due to an unfavorable interaction. An optimal blowing condition was established at approximately halfway down the chine using a jet angle of 35 degrees outboard and a jet inclination angle of 20 degrees upwards as measured from the chine reference plane. Blowing at this station eliminated interaction of the vortices up to 30 degrees angle of attack. Asymmetric blowing was also incorporated into this study and was shown to force or alter large flow asymmetries, in addition to decoupling of the vortices up to an angle of attack of 36 degrees. At a sideslip angle of 5 degrees, large asymmetries in the vortex core trajectories and breakdown locations were observed. Asymmetric blowing while in sideslip decoupled vortices on the windward side and delayed vortex breakdown up to 24 degrees angle of attack.

Other methods of controlling the location of breakdown of leading edge vortices have also been investigated. Parmenter and Rockwell (20) addressed the possibility of restabilizing the leading edge vortex on a delta wing by transient suction. A delta wing with a sweep angle of 75 degrees at an angle of attack of 35 degrees was used for this investigation. A suction probe was used to introduce the transient suction above the upper surface of the wing. Flow visualization showed four

identifiable stages leading to vortex breakdown. These four stages were: 1) downstream movement of the breakdown and an insignificant change of the radius of the breakdown spiral; 2) continued downstream movement of the spiral pattern, accompanied by a decrease in radius of the spiral; 3) rapid decrease in radius of the spiral, eventually becoming indiscernible and leaving a breakdown bubble upstream of a turbulent wake; and 4) stabilization of the turbulent breakdown regime as it was drawn into the probe. Hysteresis in the vortex breakdown position was shown to occur as the vortex returned to its no suction equilibrium position. Response time for stabilization of the vortex after the onset of suction was best at high suction coefficients, and the response time increased as the suction probe was moved downstream of the wing trailing edge. Parmenter and Rockwell suggested that moving the suction probe further upstream and closer to the onset of vortex breakdown would allow stabilization of the vortex flow with considerably lower suction coefficients.

Qualitative studies of the behavior of a complex flow field such as a vortical flow field can provide some of the information needed to understand this category of flows. To allow for a more in depth understanding of complex flows, a detailed quantitative data base is required. It is in this type of quantitative study where the laser Doppler anemometer becomes an invaluable tool in the study of complex flows. A laser Doppler anemometer has the ability to provide detailed three-dimensional flow field information. Limited

documentation using laser Doppler anemometry to obtain data in the vortex flow field is in existence.

Meyers and Hepner (21) demonstrated the capabilities of a three component laser velocimeter to provide a detailed experimental database for a vortex flow field above a 75 degree sweep delta wing at angles of attack of 20.5 and 40.0 degrees. Mean velocity measurements were shown to be accurate to within 0.5 percent and turbulence intensities to be accurate above twice the residual value of 1.0 percent. Meyers and Hepner displayed mean velocity and turbulence intensity contours for the 20.5 degree angle of attack case along with contours of the burst vortices at 40 degrees angle of attack. The streamwise velocity component increased to twice the freestream value within the core for the unburst vortices, but reversed flow was present in the core of the burst vortices.

Kegelman and Roos (22) obtained laser Doppler anemometry data for the flow field over a 70 degree sweep delta wing to determine the effects of leading edge shape and vortex breakdown. Leading edge shape was found to significantly affect the location of leading edge vortex breakdown. Laser Doppler anemometry showed a loss of velocity of the core of the vortices as a result of vortex breakdown.

Laser velocimetry measurements of the flow field above a delta wing in conjunction with a leading edge extension have been obtained by Novak, Huie, and Cornelius (23), and Sellers, Meyers, and Hepner (24). Novak, Huie, and Cornelius obtained three-dimensional velocity surveys using a two by

15

two-dimensional laser velocimetry method. A generic fighter configuration with a forebody strake sweep of 77 degrees and a wing sweep of 56 degrees was used to generate the vortex flow field in a 150 feet per second flow. Cross flow velocity vector plots showed a chordwise development of the leading edge wing vortex at an angle of attack of 10 degrees. Plots of the velocity vectors, also at 10 degrees angle of attack, showed only a single center of vorticity. Vortex breakdown near mid chord at an angle of attack of 18 degrees showed a dramatic change in axial velocity with reverse axial velocities near the center of the vortex. Plots of vortex breakdown and trajectory were obtained for both angles of attack of 10 and 18 degrees.

Sellers, Meyers, and Hepner conducted an investigation using a laser Doppler velocimetry survey of the vortex flow field over a 3 percent scale model of a Northrop YF-17. Vortex breakdown was found at an angle of attack of 25 degrees in the vicinity of the wing/leading edge extension intersection. Reverse flow in the core of the burst leading edge extension vortex was obtained with the magnitude of the reverse flow being up to 10 percent of the freestream value. Root mean square velocity fluctuations reached maximum levels of 40, 35, and 30 percent for the respective streamwise, lateral, and vertical velocity components.

An experimental investigation of delta wing vortex flow with and without blowing using laser Doppler anemometry was performed by Iwanski, Ng, and Nelson (25). The flow field was measured over a 70 degree sweep delta wing at 30 degrees angle

of attack. Blowing was generated by an external jet blowing parallel to and at the leading edge of the wing at blowing coefficients ranging from 0.0 to 0.04. Blowing was shown to delay vortex breakdown. The blowing jet was found to be entrained by wrapping around the outer portion of the vortex. Root mean square velocities contained vortex centerline peaks prior to vortex breakdown. A reduction in the peaks of the root mean square velocities, a reduction of the outer core velocity, a reduction in the swirl angle, and a widening of the vortex region were shown to be the major effects of breakdown. Iwanski, Ng, and Nelson estimated the outer core swirl angle to be 40 degrees at vortex breakdown.

3.0 EXPERIMENTAL APPARATUS

3.1 INTRODUCTION

The experimental apparatus used in the present investigation of the vortical flow field created over a generic fighter aircraft model consisted of:

1) The generic fighter aircraft model,

2) The laser Doppler anemometer, and

3) The wind tunnel and associated flow visualization, smoke generator systems.

3.2 DESCRIPTION OF MODEL

The model used for this experimental investigation was of a wing-body, generic fighter configuration constructed completely of aluminum. The wing and strake planforms were made of 0.32 cm thick aluminum plate, and the fuselage of the model was constructed from 6.35 cm diameter aluminum round, 55.7 cm in length. A full span model rather than a half span model was chosen for this investigation to better represent a completely developed vortical flow field, and because some questions remain unanswered about the validity of results obtained using half span models. The models used in the investigations by LeMay and Rogers (19) and Erickson, et. al. (9 and 10) were used as a guide during the design and construction of this model, with the differences between the present model and the

models of references 9, 10, and 19 essentially being only in the scaled sizes of the models. The similarity in the design of the models allows for an excellent basis for comparison between the different experiments, and provides more detail to the data base for this specific configuration. Three views of the general configuration of the model are shown in Figure 3.2.1.

The fuselage of the model consisted of two parts: the nose and the main fuselage. The first 14.48 cm of the fuselage was used for the nose of the model, and the remainder for the main fuselage. The main fuselage was constructed from aluminum round with an original diameter of 5.72 cm. The very tip of the nose of the fuselage had a part-spherical cross section which gave the nose a blunted tip, to minimize the effect of slight model asymmetries on the development of the forebody vortices. This part-spherical, blunted tip had a diameter of 0.5 cm. The expansion of the nose from the blunt tip to the 5.72 cm diameter circular cross section of the main fuselage was described by a tangent ogive curve. This tangent ogive curve followed a geometric equation whose coordinate origin was located at the tip of the nose. The geometric equation for the tangent ogive curve was as follows:

$$(x+35.25)^2 + y^2 = 38.11^2 \qquad (3.1.1)$$

where x and y are measured in centimeters. A threaded stud located on the centerline of the main fuselage and protruding from one end was used to attach the nose to the main fuselage.

The fuselage of the model was slabsided on both sides.

These slabsides were parallel to each other and were perpendicular to the plane of the wing. The slabsiding created 2.69 cm tall flat surfaces on both sides of the fuselage, that began 8.86 cm from the tip of the nose and ran the entire length of the fuselage. As a result of the slabsiding, the width of the fuselage was reduced to 5.03 cm. Slabsiding the fuselage allowed for access at any axial location on the fuselage to install blowing tubes at various locations for pneumatic blowing purposes. Pneumatic blowing required a source of pressurized air at each of the desired blowing locations. For the present investigation pneumatic blowing was oriented in the streamwise direction tangential to the wing surface at various chordwise locations. Accessing the model at various axial locations along the fuselage was required, necessitating the need for slabsiding of the fuselage.

Pressurized air was supplied to axial locations on the fuselage by means of two 1.91 cm diameter holes drilled inside the length of the fuselage. This pair of holes ran axially and parallel to one another, centered 0.7 cm above the centerline of the fuselage, and 1.27 cm off the centerline, from the aft end of the fuselage to 10.16 cm from the tip of the nose. An inability to drill a 45.54 cm long hole from the rear of the model necessitated making the fuselage with a detachable nose. By placing these axial holes slightly above the centerline of the fuselage, mounting the wings and the forebody strakes into the fuselage in close proximity to the centerline was still possible. To provide access of the pressurized air at the

desired axial locations on the fuselage, four circular holes were made in each slabside. These holes were deep enough to enter the existing holes inside the fuselage. These access holes were 1.51 cm in diameter and 1.27 cm deep, and were centered 0.24 cm below the centerline of the fuselage. The four axial locations of the access holes were 11.05 cm, 15.8 cm, 24.51 cm, and 33.4 cm aft from the tip of the nose, as shown in Figure 3.2.2, and listed in Table 3.2.1.

Mounting of the wings and the forebody strakes into the fuselage was accomplished by 0.32 cm wide by 1.27 cm deep rectangular slots made in the slabsides of the fuselage. The slots were centered 0.64 cm below the centerline of the fuselage, and began 4.29 cm from the tip of the nose and ended 3.1 cm from the tail of the fuselage. There were five slots in each side of the fuselage, with the axially located pneumatic blowing access holes separating the slots. The wings and forebody strakes were placed in the slots and locked in by set screws that were accessible from the bottom of the fuselage. Placement of the rectangular slots was such that the centers of the four pneumatic blowing access holes in each side of the fuselage were 0.16 cm above the surfaces of the wings and the forebody strakes. A complete drawing of the fuselage is shown in Figure 3.2.2.

The wing planform consisted of a flat plate, cropped delta wing with a 55 degree sweep. The underside of all edges of the wing were beveled at 45 degrees to produce a sharp edge on the upper surface of the wing. The root chord and tip chord

21

lengths were 31.75 cm and 6.35 cm, respectively, and the span of the wing was 35.56 cm. The resulting aspect ratio of the wing planform was 1.867 and the taper ratio was 0.20. The wing chord at the fuselage juncture began 24.61 cm from the tip of the nose and stopped 6.35 cm from the end of the fuselage, giving a wing chord at the juncture of the fuselage of 28.14 cm. As described previously, the wings and forebody strakes were mounted into the slabsides of the fuselage by securing them in the rectangular slots. To coincide with the slots, the wings were constructed with two rectangular tabs to produce a flush fit of the wings with the slabsides of the fuselage. A schematic of the wing planform is shown in Figure 3.2.3.

Two different pairs of forebody strakes were designed and constructed for use on the model. Both pairs of strakes had essentially identical spans or widths, and were designed to blend into the leading edge of the wings at the wing/strake intersection. The difference between the two pairs of strakes was in their length. The longer pair of strakes had a total reference area that was 7.54 percent of the total wing area, a length of 22.63 cm, and extended from the leading edge of the wing to 4.29 cm from the tip of the nose. The shorter pair of strakes had a reference area of 6.94 percent of the total wing area, was 17.93 cm in length, and extended upstream to 9.02 cm from the tip of the nose. This is approximately where the tangent ogive portion of the nose ends. The leading-edge geometries of both pairs of the forebody strakes were described by geometric equations whose origins were at the tip of the

22

nose of the fuselage. The equation describing the longer pair
of strakes was:

$$(x+20.18)^2 + (y-15.24)^2 = 24.33^2 \qquad (3.1.2)$$

The equation describing the shorter pair of strakes was as
follows:

$$(x+7.71)^2 + (y-15.24)^2 = 11.86^2 \qquad (3.1.3)$$

where x and y are measured in centimeters. Thus, both strake
designs had circular-arc leading edge contours. Both pairs of
forebody strakes were beveled at 45 degrees on the underside of
the leading edge to produce a sharp edge on the upper surface
of the strakes to match the wing. The strakes were also
constructed with rectangular tabs to allow for attachment and a
flush fit of the strakes into the fuselage of the model.
Schematics of the long and short strakes are shown in Figure
3.2.4.

As is evident in the design and construction of the
fuselage, wings, and strakes, the main focus of interest was to
design and construct a model which would be capable of
pneumatic blowing at several axial locations along the wings
and forebody strakes. These axial locations were selected and
constructed so that the three aft locations for this
investigation would match the three front locations of the
model used by LeMay and Rogers (19). The four axial locations
of the access holes were placed so as to coincide with specific
chord locations on the wings and forebody strakes. These chord
locations are listed in Table 3.2.1, where the percent of chord
of the locations as referenced to the individual lengths of the

long and short strakes, respectively, range from 11.3 to 89.3 percent.

To blow pneumatically at one location and not at the others, a series of blowing plugs were designed to fit in the access holes. Two types of blowing plugs were constructed, both with a diameter of 1.51 cm and a depth of 1.27 cm, and both fitted with properly sized O-rings to prevent any air leakage from around the outer diameter of the plugs. These plugs were locked in the access holes partly by set screws accessible from the bottom of the fuselage, and partly by wings and strakes also mounted in the fuselage. The difference between the two types of plugs was in the drilling of a 0.16 cm diameter hole through the centerline of one of the types of plugs. The size of the 0.16 cm diameter hole was chosen to allow the insertion of 0.16 cm outer diameter brass tubes. These brass tubes served as nozzles for the air jet and could be of any length or orientation, protruding out of the blowing plugs approximately one tube diameter above the surface of the wings and strakes. By using the plugs inserted with the brass tubes, small, high pressure jets of air could be injected from any of the four pairs of access holes. Pneumatic blowing at the four chordwise locations was possible at any angle of incidence above the surface of the wings or strakes, and at any angle of jet blowing as measured from the slabsides of the fuselage.

For this investigation, two types of nozzle orientations were used. One type consisted of the nozzles being located at

and parallel to the leading edge of the strakes. The second type consisted of a shorter tube length of approximately 0.95 cm at a jet angle of 35 degrees from the slabside of the fuselage. This second type of nozzle orientation was similar to that used in the investigation of LeMay and Rogers(19). Figure 3.2.5 contains schematics of the blowing plugs and the chosen nozzle orientations of the brass tubing.

The pressurization of the air fed into the axial holes inside the fuselage was controlled by a source located outside of the wind tunnel test section. Plastic tubing with an outside diameter of 0.64 cm was used to feed the pressurized air into the rear of the fuselage. The pressurized air was delivered by an air compressor located in the West Virginia University Aerodynamics Laboratory which was capable of supplying pressurized air at up to 29 KPa (200 psi). A 23.2 KPa (160 psi) pressure regulator and two pairs of Dwyer rotameters, 0 to 0.57 m^3/hour (0 to 20 scfh) and 0 to 2.83 m^3/hour (0 to 100 scfh), were used to control separately the flow of air into the 0.64 cm plastic tubing, and ultimately each of the blowing ports on each side of the fuselage of the model. With this flow control set-up, the blowing coefficient could be determined using the following relationship:

$$C_\mu = \dot{m} V_j / q S \qquad (3.1.4)$$

Where $\dot{m}$ is the mass flow of the jet, V_J is the jet velocity, S is the surface area of the wing, and q is the freestream dynamic pressure. A block diagram of the blowing flow control hardware is shown in Figure 3.2.6.

For this investigation, two methods were used to calculate the blowing coefficient, and both used the assumption of choked flow at the exit of the brass tubes. One method used a correction of the rotameters to indicate the true flow rate of the blowing jet, see Tse and Morse (26). This correction involved a recalculation of the density and flow rate for the increased pressure, and resulted in a blowing coefficient of 0.016. The second method calculated the mass flow rate of the blowing jet by using Fanno line flow techniques, see John (27). Using Fanno line flow, blowing coefficients were calculated for each of the nozzles used for this investigation and resulted in blowing coefficients ranging from 0.016 to 0.018. For simplicity, the blowing coefficient for the remainder of this investigation will be referred to as 0.016.

Mounting the model in the test section consisted of placing the model on a solid steel circular, "bent" sting. The "bent" sting consisted of two parts, a 2.54 cm diameter by 30.48 cm long circular cylinder sting, and a 1.27 cm thick solid steel flat plate. Three sets of holes were drilled in the flat plate at 10 degree intervals. By mounting the circular cylinder sting to the flat plate using the existing sets of holes, the sting could be placed at an angle of attack of 10, 20, or 30 degrees with respect to the freestream. For the present study, the 20 degree setting was used. The "bent" sting was connected to an angle of attack mechanism, also constructed of steel, giving a possible angle of attack range of the sting of -10 to 48 degrees angle of attack. A 2.54 cm diameter by 3.81 cm long

hole was drilled in the end of the fuselage of the model to accommodate the end of the circular cylinder sting. By sliding the model onto the sting and anchoring the model to the sting with the use of set screws located in the bottom of the model fuselage, the model could be placed at any angle of attack in the range of the angle of attack mechanism. The sting and the angle of attack mechanism are shown in Figure 3.2.7.

3.3   DESCRIPTION OF LASER DOPPLER ANEMOMETER

The laser Doppler anemometer (LDA) used for the present investigation was a three-component, five beam system made commercially by DANTEC.   The complete layout of the three-component LDA was described in a paper by Buchave (28). The LDA system had standard DANTEC 55X modular optics, and used a model 2020, five Watt Spectra Physics argon-ion laser, mounted to a three-dimensional computer controlled traversing system.   A schematic of the complete LDA system is shown in Figure 3.3.1, and a discussion of some basic principles of laser Doppler anemometry are included in Appendix A.

Independent one-channel and two-channel anemometers formed the three-dimensional system.   Both the two-channel and one-channel LDA systems used the standard DANTEC 55X modular optics which included a beam splitter, a 55N10 Bragg cell frequency shifter, a beam displacer, a back scatter section, photomultiplier optics and photomultiplier tubes, a pinhole section, a beam translator, and a beam expander.   The frequency shifters allowed for measurements in reversing flows, and the beam expanders increased the signal to noise ratio.

The three separate LDA channels were formed by the use of color separation, and consisted of three sets of beams with wavelengths of 476, 488, and 514.5 nanometers.   The two-channel anemometer used the 488 and 514.5 nanometer wavelength beams, and the single channel anemometer used the 476 nanometer wavelength beam.   Using the coordinate system shown in Figure

3.3.1, the vertical velocity component along the z-axis was measured using the 488 nanometer wavelength beam, the velocity component along a plane inclined 30 degrees above the y-axis was measured using the 514.5 nanometer wavelength beam, and the velocity component along a horizontal plane inclined 30 degrees below the y-axis was measured by the 476 nanometer wavelength beam. A vector transformation was used to transform the velocity components from the non-orthogonal to the orthogonal coordinate system.

The beams exiting each separate LDA system were focused to a single point using two pairs of front surfaced mirrors angled at 45 degrees and mounted in mirror cubes. One pair of the mirror cubes were the bottom, stationary cubes located directly in line with the LDA optical systems. These bottom, stationary mirrors deflected the horizontal and parallel beams exiting the beam expander sections vertically onto a second, top set of 45 degree front surfaced mirrors. The second, top set of 45 degree mirrors were mounted at ±75 degree angles from the x-axis, with 1.2 meter focal length lenses mounted on each. It was this top set of 45 degree mirror cubes with the 1.2 meter focal length lenses that were used to focus the beams of each LDA system into a single "point", or probe volume. Coincidence of the probe volumes of the two-channel LDA and the single channel LDA was obtained by manually adjusting the top mirror cubes. Coincidence of the three channels was necessary to ensure the signals from the three channels were due to a single seed particle. The top mirror cubes could be traversed

vertically with respect to the rest of the LDA system to traverse the probe volume along the z-axis. Traversing the probe volume along the x and y-axis was completed by moving the entire LDA system.

The signals collected by the photomultiplier tubes were sent to three DANTEC 55L90A counter processors, which were operated in the combined mode. From the counter processors, the output went to a DANTEC 57G20 buffer interface and a 57G149 coincidence filter. The buffer interface and the coincidence filter accepted the validated data from each channel, checked that the three velocity measurements were all measured within the selected coincidence window, and measured the time between each set of measurements of the three velocity components. The coincidence window was a user selected time window which was used to define the coincidence of the data. The validated, coincident data and the measured sample time interval were sent to a PDP 11/23 microcomputer for storage. For the data reduction procedure, the data files were uploaded from the PDP 11/23 to a VAX 11-785 computer. Maximum total throughput of data was nominally six to ten kiloHertz. The entire LDA system was controlled by DANTEC LDAMAP menu-driven interactive software.

3.4 DESCRIPTION OF WIND TUNNEL AND FLOW VISUALIZATION CAPABILITIES

The present experiments were conducted in the West Virginia University low speed wind tunnel. This tunnel is a closed return, atmospheric facility with a test section 81.28 cm by 114.3 cm in cross section, by 121.92 cm in length. Plexiglas windows and fluorescent lights are installed in the side walls of the test section to provide a wide field of view for flow visualization. Maximum test section velocity is 76.2 m/s with no turbulence screens installed, and test section turbulence intensities are approximately 0.4 percent. Three turbulence screens are available for use in the wind tunnel which may be installed in the settling chamber upstream of the test section. The turbulence intensity is reduced to 0.06 percent with all three turbulence screens installed. Figure 3.4.1 shows a schematic of the test section of the wind tunnel.

During the present study the capability of the injection of smoke into the tunnel was developed for use with flow visualization. Smoke injection could be originated from three separate locations: the settling chamber upstream of the test section, from the plenum of the tunnel, and at the beginning of the test section. A Rosco smoke generator was located on the floor of the settling chamber upstream of the test section. This smoke generator could create up to 42.48 cubic meters per minute of smoke and used a non-combustive, non-toxic smoke fluid to create the smoke.

Two smaller smoke generators capable of generating a small filament of smoke were located in the plenum and in the beginning of the test section of the tunnel. These smoke generators also used the non-combustive and non-toxic smoke fluid for the smoke generation. The smaller smoke generator placed in the plenum of the tunnel was connected to a 152.4 cm long, 2.54 cm diameter circular cross section rod that was mounted to a two-dimensional traverse on top of the wind tunnel. The 152.4 cm long rod entered the plenum via a sliding door in the roof of the plenum of the tunnel to prevent air leakage from the plenum. With the smoke generator mounted to the traverse, a filament of smoke could be injected from any point in a 58.52 cm by 55.78 cm area in the center of the plenum of the wind tunnel. This area coincides with a smaller area of 7.32 cm by 7.01 cm in the test section of the wind tunnel due to the 8 to 1 contraction ratio of the plenum to the test section. The remaining smaller smoke generator was mounted at the upstream end of the test section of the tunnel. This generator was connected to a circular cross section metal rod that entered the test section through a hole located on the centerline of the test section floor. With this method of mounting of the third smoke generator, only vertical movement of the smoke filament was possible, with a range of only 30.48 cm. However, with this 30.48 cm of vertical movement, a small filament of smoke could be placed in any streamline of the flow over the model. Figure 3.4.2 contains a schematic of the wind tunnel showing the locations of the smoke generators.

Flow visualization for this investigation consisted of the injection of smoke into the wind tunnel at the desired location and using a laser light sheet to illuminate the flow field in the test section. The light sheet was generated by using the five Watt Spectra Physics argon-ion laser and a 0.95 cm diameter by 5.08 cm long cylindrical glass rod. Directing the laser beam through the diameter of the glass rod created a light sheet that was directed along a plane perpendicular to the centerline of the glass cylinder. The light sheet was traversed in the x and y directions by mounting the glass rod to the traverse of the laser Doppler anemometer. With this set-up, a light sheet was generated to illuminate the test section of the tunnel at any location along the x or y-axis. The intensity of the light sheet could be controlled by varying the output of the five Watt laser. Also, the orientation of the light sheet could be altered by rotating the glass rod.

Seeding of the flow for laser Doppler anemometry was accomplished by using 0.8 micron diameter polystyrene microspheres as described by Nichols (29). These spherical plastic particles were suspended in a mixture of fifty percent distilled water and fifty percent pure ethanol. Injection of this water/ethanol/particle mixture into the freestream of the wind tunnel was accomplished by using an agricultural sprayer and an air atomizing nozzle fitted to the previously mentioned two-dimensional traverse located in the wind tunnel plenum. The agricultural sprayer was used to pressurize the mixture to approximately 34.47 KPa (5 psi) to transport the mixture to the

two-dimensional traverse and ultimately the air atomizing nozzle. The air atomizing nozzle was also supplied with a constant flow of air pressurized at 68.95 KPa (10 psi). Small adjustments were made with the air atomizing nozzle flow rate to obtain the desired output of seed particles into the flow.

4.0 EXPERIMENTAL PROCEDURE

4.1 FLOW VISUALIZATION

Flow visualization was used for the present investigation to qualitatively determine the position of vortex breakdown and to determine the degree of interaction of the strake and wing vortices, both with and without pneumatic jet blowing. Three different views of the vortex flow field above the fighter model were possible for this investigation. To obtain these views variations were made in the location of smoke injection and in the orientation of the light sheet. Due to the relatively close proximity of the vortices to the wing surface of the fighter model under most circumstances, viewing of the vortices on the side opposite of the origin of the light sheet was extremely difficult. This difficulty in viewing was due to the shadow cast on the wing due to the fuselage of the model. As a result, the flow visualization of the vortical flow field was usually limited to essentially a half-span investigation of a full span model.

The individual cores of the unburst wing and strake vortices were visualized as dark holes, or voids, in the light sheet when smoke was injected from the settling chamber upstream of the test section and the light sheet was in a position perpendicular to the plane of the wing surface. At breakdown, the cores of the vortices were no longer void of the smoke particles, and therefore were not visible. This

decreased visibility of the cores was due to the loss of velocity in the cores of the vortices at breakdown, and the resulting increase of smoke particles in the core of the vortices due to the decreased core circumferential velocity. The interaction of the wing and strake vortices was demonstrated using this flow visualization by noting the degree of coupling exhibited by the individual cores. The breakdown locations and degree of interaction of the vortices were found as a function of the wing chord position by traversing the light sheet along the chord of the wing and noting the corresponding chord locations.

Using the smaller smoke generator located at the upstream end of the test section made it possible to visualize individual streamlines of the vortex flow over the strake. This was accomplished by locating the smoke filament on the underside of the nose of the fuselage so as to allow the smoke filament to be entrained into the strake vortex. With an individual streamline of the strake vortex visually marked, the position of the vortex was found with respect to the wing surface and fuselage. This visualization did not require the use of the light sheet and was visible with the lights in the test section of the wind tunnel.

A cross-sectional view along the axis of the strake and wing vortices was accomplished by orienting the laser light sheet parallel to the wing surface and again injecting a smoke filament on the underside of the nose of the fuselage. Properly locating the smoke filament made it possible to place

smoke in both the wing and strake vortices. Use of this type of flow visualization created the cross-sectional views of the vortices at different heights above the model, and offered some assistance in determining the existence and degree of interaction of the vortices above the fuselage.

With these types of flow visualization, both a video camera and a 35 mm camera were used to document the vortical flow field generated by the fighter model mounted in the test section of the wind tunnel. The three different views of the vortical flow field allowed for a more in-depth look at the alterations of the flow field with and without pneumatic jet blowing. The effects of blowing were documented on video tape for changes in the model configuration, the blowing location and the blowing orientation, and in the angle of attack of the model. Care was taken to ensure that the model was always centered in the test section of the wind tunnel to reduce possible asymmetries in the vortex flow field. Changes in the configuration of the model consisted solely of installing either the long or short strakes, or using a wing-body configuration. The model angle of attack was varied from 20 to 36 degrees. The blowing coefficient and freestream velocity were kept at constant values of 0.016 and 15 m/s, respectively. The resulting chord Reynolds number was 270,000, based on a wing chord of 28.14 cm.

All of the flow visualization results for the different blowing variations were recorded on video tape, with eventually over 40 hours of flow visualization being permanently recorded.

The chosen best blowing variations were determined by viewing these video tapes, with the selected best blowing variations also being permanently recorded with 35mm photographs. The major portion of the results stored on the video tape consisted of flow visualization with the light sheet oriented perpendicular to the plane of the wing surface. Using this orientation of the light sheet in conjunction with the injection of smoke from the plenum of the wind tunnel, allowed for the cores of the vortices to be visualized as small dark holes or voids in the light sheet.

To select the best and most effective blowing variations, a method of judging the locations of wing and strake vortex breakdown and for judging the amount of strake and wing vortex coupling or interaction had to be created. The onset of vortex breakdown was defined visually as a sudden increase of the vortex core diameter. For this specific flow visualization method, the light sheet was traversed aft along the wing planform to determine the vortex flow field behavior at each desired X/C location. As the light sheet was traversed aft along the wing, beginning at the apex of the wing, the core diameters of the wing and strake vortices would first begin to slowly fluctuate from the small core diameter characteristic of the unburst vortices to a larger core diameter. At X/C locations farther aft, the fluctuations of the vortex core diameters would increase to the point that the vortex core diameters would approach diameters characteristic of the vortices at breakdown. The fluctuations would cease at

positions farther aft leaving the vortex cores at the larger core diameters characteristic of breakdown. At X/C locations approaching the trailing edge of the wing the cores of the vortices would often become no longer visible. The visual definition of the onset of vortex breakdown as a sudden increase in the vortex core diameter was a valid choice for this particular vortex flow field.

To determine the X/C location of vortex breakdown for the wing and strake vortices, the light sheet was traversed aft along the wing chord in increments of 1/20 chord. By maintaining a normal relationship between the light sheet and wing surface, the vortex breakdown locations at any angle of attack or model configuration were determined with an accuracy of approximately 5 percent of the wing chord.

Coupling of the wing and strake vortices was defined visually as the X/C location when the core of the strake vortex would pass directly underneath the core of the wing vortex. For a more precise definition, a right handed coordinate system was visually located at the center of the core of the wing vortex, where the wing vortex was in a position above the wing surface. The y-axis of this coordinate system was parallel to the plane of the wing, and positive in a direction away from the leading edge of the wing, while the z-axis was perpendicular to the plane of the wing and positive in a direction towards the surface of the wing. Using this coordinate reference frame, the y-axis coincided with the value of zero degrees rotation of the strake vortex about the wing

vortex. The z-axis represented a 90 degree rotation of the strake vortex about the wing vortex core. This coordinate system is shown in Figure 4.1.1. Thus coupling of the wing and strake vortices occurs when the strake vortex coincides or passes through the z-axis. To help prevent any future misunderstanding in the interpretation of the flow visualization results, it should be noted that the coupling location of the vortices were sometimes observed at X/C locations farther aft than the breakdown locations. By definition, the coupling of the wing and strake vortices could exist before or after the onset of vortex breakdown.

The flow visualization results recorded on videotape consisted of tests of the different blowing schemes (tube type, tube orientation, and blowing location) at each angle of attack of 20, 24, 26, 28, and 36 degrees for each of the different model configurations. The different blowing schemes consisted of using each of the four blowing port locations along the fuselage, in conjunction with the two different blowing nozzles. By using both of the nozzles at each blowing port, blowing was initiated both along the leading edge of the strake and angled 35 degrees from the fuselage inside the leading edge of the strake (see Figure 3.2.5). By testing the effectiveness of blowing using both of the nozzle configurations, the four blowing port locations, the long and short strakes, and the five test angles of attack of the model, 80 different blowing variations were tested. In conjunction with each of the 80 different variations of the blowing schemes, the blowing

nozzles were varied to five different blowing angles of incidence with respect to the wing plane. These blowing angles of incidence were measured from a plane parallel to and 0.16 cm above the wing and strake surface. The five angles of incidence of the blowing nozzles consisted of -10, 0, 10, 20, and 30 degrees. The -10 degree angle of incidence placed the tip of the blowing nozzles directly on the strake surface. For the 400 different blowing variations under investigation, only one blowing coefficient of 0.016 was used during this investigation. Due to the relatively low magnitude of the blowing coefficient, it was hoped that the results and application of any of the blowing schemes would prove feasible for a full-scale conventional aircraft without a major loss in efficiency.

4.2 LASER DOPPLER ANEMOMETRY

Laser Doppler anemometry was used during this investigation to obtain velocity measurements of the vortex flow field for specific blowing orientations, for one optimal blowing configuration as determined from the flow visualization. The three velocity measurements from the LDA system consisted of one vertical velocity and two horizontal velocities. The vertical component of velocity was measured directly while the two horizontal velocities were measured at positive and negative 15 degree angles with respect to the tunnel centerline. With this three component system, streamwise and spanwise velocities were then computed by transformation from the non-orthogonal measured velocities. This transformation was completed off-line during the data reduction procedure. All three channels of the laser Doppler anemometer were operated in the backscatter mode. Also, the three channels utilized beam expanders and frequency shifters to increase the signal to noise ratio and to allow for measurements in reversing flows, respectively. The frequency shifters were of particular importance to this experiment due to the need to determine the flow direction of the vortex flow field. The two-dimensional and one-dimensional laser Doppler anemometry probe volumes were manually focused to be coincident by placing all the five beams through a 100 micron pinhole mounted on a three-dimensional linear positioning stage. Standard DANTEC counter processors were used in conjunction with a DANTEC

buffer interface and coincidence filter.

During each data taking procedure, validated and coincident data were collected under computer control using DANTEC software installed on a PDP-11/23 microcomputer. Data were then uploaded to a VAX 11-785 computer for data reduction and plotting. It was during this data reduction procedure when the non-orthogonal horizontal velocity components were transformed to the streamwise and spanwise velocity components. In the data reduction process all the data were sorted into velocity histograms. The tails of these histograms were omitted as "spurious" data. Data outside approximately positive and negative 2.56 standard deviations of the mean were deleted in this fashion; this should have deleted approximately 1% of the data. As a check for evidence of velocity bias in the data set, the results were computed using both statistical averaging as well as sample interval time weighting. Only small differences were found in the use of either of these two methods for data reduction whenever particle seeding was maintained at a constant rate. As a result, all the resulting velocity data presented in the present work were calculated using statistical averaging without velocity bias corrections.

The data taking procedure used to obtain the velocity data consisted of measuring the data in a plane perpendicular to the wing surface. A grid pattern of points within the perpendicular plane was established and measurements were obtained at fixed locations within the plane. The resulting measurements were given in a wind axis system.

At the 0.45 X/C location of the wing, the distance along the spanwise direction from the leading edge of the wing to the wing/fuselage juncture was 8.87 cm. The measurement grid pattern used consisted of seven grid lines in the vertical direction and 11 grid lines along the span of the wing. The spacing of these grid lines in the vertical direction was 1.27 cm as measured perpendicular to the wing surface. The spacing along the wing span consisted of 0.81 cm intervals between the grid lines. At each grid intersection, three-dimensional laser velocimetry data were taken in 1856 point files, with a coincidence time window of 75 microseconds. Taking laser velocimetry data at each grid intersection allowed for an investigation of 77 locations in the perpendicular plane.

Planes of velocimetry data were taken both with and without blowing at the 0.45 X/C location at 20 degree angle of attack. The blowing configuration studied was the best blowing configuration for the long strakes, which consisted of using the short 35 degree blowing nozzles at blowing port number one (the most forward location) with the blowing nozzle located on the strake surface. As will be presented in Figures 5.1.3 and 5.1.11, blowing using this optimal configuration completely restores the vortical flow field at the 0.45 X/C location. All of the velocities determined have been given in a wind-axis system with the origin of this system located at the leading edge of the wing at the 0.45 X/C location. In this wind-axis system the x-axis and u-velocity were positive in the freestream direction. The y-axis and v-velocity were positive

44

in the spanwise direction from the leading edge of the wing towards the fuselage. Consistent with a right hand coordinate system, the z-axis and w-component of velocity were positive in the vertical direction perpendicular to the wing surface.

5.0 RESULTS AND DISCUSSION

5.1 FLOW VISUALIZATION

Flow visualization was used to qualitatively determine the effects of blowing on the bursting and coupling of the strake and wing vortices. The main goal was to determine specifically the blowing locations and orientations with the greatest beneficial effect on the breakdown and coupling locations of the wing and strake vortices. The blowing scheme with the greatest positive effects on the vortex flow field was then further investigated using laser Doppler anemometry.

To determine the blowing configurations with the greatest effect on the breakdown and coupling locations of the strake and wing vortices, each blowing case had to be judged for changes as compared to the appropriate baseline, or no blowing, case. The behavior of the vortex cores before and after breakdown remained consistent and repeatable for all tested angles of attack and for each model configuration. During the judging of each individual blowing case, some general observations were noted of the behavior of the vortex flow field. As the model angle of attack increased, the breakdown locations of the wing and strake vortices moved forward toward the apex of the wing. Blowing at locations in close proximity to the apex of the wing or strake was in general found to be much more effective than blowing at any other location on the strake or wing chord. For the short strakes, the blowing

46

configurations using the shorter 35 degree angled blowing nozzles were the most effective blowing variations in delaying vortex breakdown and coupling. However, this was not the case for the longer strakes. With the long strakes installed on the model, blowing along the leading edge of the strake was equally effective as blowing using the shorter 35 degree angled blowing nozzles. Due to the occurrence of vortex breakdown at positions nearer to the wing apex at angles of attack of 28 and 36 degrees, coupling of the wing and strake vortices was observed only at the lower angles of attack of 20, 24, and 26 degrees. Also, in general, the breakdown location of the wing vortex showed little or no change as a result of blowing even when the most effective blowing variations were used.

Before the actual rankings of the blowing variations could be determined, the breakdown and coupling locations for the no blowing cases for each model configuration had to be determined for each model angle of attack. The breakdown locations were determined as a function of the distance from the breakdown location over the wing to the wing apex and were non-dimensionalized by the root chord of the wing. Figure 5.1.1 shows the breakdown locations of the wing and strake vortices as a function of the model angles of attack. From this figure for the no blowing cases, it was seen that the vortices generated by the long strakes had breakdown locations farther aft than the vortices generated by the short strakes. At the model angles of attack of 20 and 24 degrees, the wing and strake breakdown positions were between 0.4 and 0.5 X/C.

47

As the angle of attack was increased, the breakdown positions for both sets of the strake vortices approached the wing apex and at 36 degrees angle of attack the strake vortices reached breakdown at the wing apex. Similarly, the breakdown positions of the wing vortices moved forward as the angle of attack increased with the breakdown position being the 0.25 X/C location at 36 degrees angle of attack. In general, the strake vortices with no blowing had breakdown positions farther aft than the wing vortices for angles of attack less than 28 degrees.

Comparisons with two investigations using similar models with a 55 degree swept wing fighter configuration with forebody strakes were completed to correlate the breakdown positions versus angle of attack. Figure 5.1.2 contains the breakdown locations as a function of angle of attack for the present investigation, an investigation by LeMay and Rogers (19), and for the investigation completed by Hall (7). The investigations by Hall and LeMay and Rogers were done in water tunnels with essentially identical chord Reynolds numbers of 1.1×10^4. In comparison, the breakdown locations for Hall's wing vortex and the present investigation wing vortex locations correlate well at all tested angles of attack from 20 to 36 degrees. The cause of the apparent differences between the investigations of LeMay and Rogers and Hall, both done in similar water tunnel flows, can be explained by differences in the models used for each experiment. Hall used a model with strakes that were shorter in length than the strakes used by

LeMay and Rogers resulting in a weaker vortex flow, and vortex breakdown locations closer to the wing apex.

A rough comparison between the breakdown locations of this investigation and that of Erickson et. al. (10) was made by approximating the breakdown and coupling locations from the photographs contained in the Erickson et. al. report. The Erickson et. al. investigation was completed in a wind tunnel with a Reynolds number flow of 7×10^4. This rough comparison showed that the results of Erickson et. al. were correlated well with that of LeMay and Rogers. Possible reasons for the discrepancies between the present investigation and that of LeMay and Rogers and Erickson et. al. can perhaps be related to the order of magnitude difference in Reynolds number and the resulting increase in the flow instabilities in a higher Reynolds number flow. It was hypothesized that the vortices could not resist breakdown in the more turbulent, higher Reynolds number flow of the present investigation.

The rankings to determine the most effective blowing variations were completed by examining the individual results for the various blowing cases and comparing with the corresponding results for no blowing. In terms of the breakdown and coupling locations, the four most effective blowing variations were chosen for the long and short strakes as a function of angle of attack with the results included in Figures 5.1.3 through 5.1.18. The results in these figures showed estimated average breakdown locations, with the estimated uncertainties included in each individual figure.

The uncertainties were determined as one-half the least count of the measuring device, which in this investigation corresponds with 5 percent of the wing chord. Presented in Figures 5.1.19 through 5.1.22 are the 35mm photographs of the two overall best blowing variations at selected X/C locations showing visually the effects of blowing at model angles of attack of 20 and 24 degrees using the long strakes.

The blowing variation with the largest effect on the breakdown and coupling locations for the long strakes was the blowing variation using the short 35 degree angled nozzles located on the strake surface at blowing port 1. Figure 5.1.3 shows the effects of this chosen blowing configuration on the breakdown locations versus angle of attack for the strake and wing vortices. The largest delay in the vortex breakdown location using this blowing scheme occurs with the model angle of attack at 20 degrees. At this angle of attack the strake vortex breakdown location was delayed to the trailing edge of the wing with blowing. Comparing to the no blowing breakdown location of 0.45 X/C, the delay in the strake vortex breakdown location was 0.55 X/C. For the wing vortex the breakdown locations with and without blowing were 0.5 X/C and 0.7 X/C respectively, a delay of 0.2 X/C. At the 24, 26, and 28 degree angle of attack cases the delay in the breakdown location of the strake vortices remained between 0.15 X/C and 0.2 X/C. However, the wing vortex showed little change in breakdown location for the 24, 26, 28, and 36 degree angle of attack cases.

The delay of the strake and wing vortex coupling locations for this best blowing configuration for the long strakes as a function of angle of attack has been shown in Figure 5.1.11. As with the breakdown locations, the largest effect on the coupling locations for this blowing variation occurred at 20 degrees angle of attack. This delay in coupling amounted to 0.6 X/C. The 24 and 26 degree angle of attack cases showed delays in the coupling locations of 0.35 X/C and 0.3 X/C, as compared with the baseline no blowing cases.

The second best blowing configuration for the long strakes used tangential to the leading edge blowing at blowing port 1 with a jet inclination angle of 10 degrees. This blowing variation had the largest effect of all the tested blowing variations on the breakdown locations of the wing vortices, as shown in Figure 5.1.4. Unlike the best blowing case discussed previously, the effects of blowing on the breakdown locations of the wing and strake vortices remained consistent throughout all the model angles of attack. For the strake vortices, the delay in the breakdown locations ranged from 0.15 X/C at 20 degrees to a high of 0.25 X/C at 36 degrees angle of attack. The minimum delay in breakdown location was 0.05 X/C for the wing vortex, with the maximum delay of 0.20 X/C being obtained at 20 degrees model angle of attack.

The delay in the coupling locations using this second best blowing variation for the wing and strake vortices is presented in Figure 5.1.12. The coupling locations of the wing and strake vortices were again significantly delayed using this

51

blowing configuration. At 20 degrees angle of attack, the coupling location was delayed 0.35 X/C from 0.4 X/C to 0.75 X/C. For the 24 and 26 degree angle of attack cases the delay in the coupling location remained consistent in value at 0.2 X/C.

Similar but smaller in magnitude delays in the vortex breakdown locations were obtained with the third and fourth best blowing variations for the long strakes. The third and fourth best blowing variations, respectively, consisted of blowing using the short 35 degree angled blowing nozzles at an inclination angle of 30 degrees at blowing port 2, and blowing tangential to the leading edge with the nozzle on the strake surface at blowing port 3. Figure 5.1.5 shows the blowing effects on vortex breakdown locations using the short blowing nozzles at an inclination angle of 30 degrees at blowing port 3. This third best blowing configuration had almost no effect on the wing vortex at any model angle of attack, which was characteristic of the majority of the blowing variations tested. Consistent delays in the strake vortex breakdown locations were observed over the angle of attack range, with the largest delay of 0.4 X/C being at the 20 degree angle of attack case. This blowing case also delayed the wing and strake vortex coupling locations by an average of 0.3 X/C, as shown in Figure 5.1.13.

For the fourth best blowing configuration for the long strakes, the most significant breakdown delays occurred in the wing vortex breakdown locations at model angles of attack of

20, 28, and 36 degrees as shown in Figure 5.1.6. This fourth best blowing case for the long strakes used blowing tangential to the leading edge of the strake with the blowing nozzles on the strake surface at blowing port 3, and delayed the wing vortex breakdown locations at the aforementioned angles of attack an average of 0.2 X/C. Delays in the strake vortex breakdown locations were also significant and ranged from a high of 0.3 X/C at 20 degrees angle of attack and showed a steady decrease to the low at 36 degrees of 0.1 X/C. However, this blowing variation was found to have only a moderate delay in the vortex coupling locations. Figure 5.1.14 shows this reduced effect on the coupling locations, with the average delay being only 0.05 X/C for the 24 and 26 degree angle of attack cases.

When comparing the best blowing configurations of the long and short strakes, the best blowing cases of the short strakes have a considerably lesser effect on the breakdown and coupling locations of the vortices. As noted previously, the most effective blowing cases for the short strakes consisted of blowing with any of the blowing configurations using the shorter 35 degree angled nozzles. The two best blowing configurations for the short strakes used these shorter nozzles located on the strake surface at blowing ports 1 and 2, respectively. Both of these best two blowing cases were more effective at the 20, 24, and 26 degree angle of attack cases in delaying the strake vortex breakdown locations.

Vortex breakdown results for the best blowing

configuration for the short strakes using the first blowing port have been shown in Figure 5.1.7. Blowing at blowing port one with the shorter 35 degree nozzles showed a maximum delay in the strake vortex breakdown location of 0.4 X/C at 20 degrees angle of attack. The delay in the strake vortex breakdown locations decreased steadily with increased angle of attack until no change in the strake breakdown location was found at 28 and 36 degrees angle of attack. The wing vortex breakdown locations ranged from 0.15 X/C to the wing apex at angles of attack of 20 and 36 degrees.

The effect on the coupling locations using this best blowing case for the short strakes has been shown in Figure 5.1.15. A considerable delay in the coupling location was observed at each of the three angles of attack. The coupling location of the strake and wing vortices was delayed until the trailing edge of the wing at the 20 degree angle of attack case, a delay of 0.6 X/C. At the 24 and 26 degree cases the delays were 0.30 X/C and 0.25 X/C respectively.

The second ranked blowing configuration for the short strakes used blowing port 2 with the short 35 degree angled blowing nozzles on the strake surface. Figure 5.1.8 displays the vortex breakdown delays due to blowing in the strake and wing vortex breakdown locations as a function of the model angle of attack. The maximum delay in the strake vortex breakdown location occurred at 20 degrees angle of attack with a delay of 0.25 X/C. At 26, 28, and 36 degree angles of attack the delay in the strake vortex breakdown location was a

consistent 0.1 X/C. Small delays in the wing vortex breakdown locations of 0.05 X/C existed at 20, 26, and 28 degrees.

The delay in the vortex coupling locations using this second ranked blowing configuration for the short strakes at 20 degrees angle of attack was 0.35 X/C (from 0.4 X/C to 0.75 X/C). At the 24 degree case the delay in the coupling location was 0.2 X/C. No coupling of the wing and strake vortices was found at the 26 degree model angle of attack. This was the result of the complete disappearance of the wing vortex immediately after breakdown at the 0.4 X/C location, thus not allowing any vortex coupling.

The third and fourth best blowing configurations for the short strakes consisted of blowing tangential to the leading edge of the strakes. The third best blowing case consisted of blowing at blowing port 3 with a jet inclination angle of 10 degrees; the vortex breakdown locations for this case have been shown in Figure 5.1.9. This blowing scheme had the largest effect on the vortex breakdown locations of the strake vortices at 24 degrees angle of attack. At this angle of attack, the strake vortex breakdown was delayed 0.15 X/C, from 0.45 X/C to 0.6 X/C. Delays in the wing vortex breakdown were consistent with 0.05 X/C changes at the lower angles of attack. The delays in the coupling locations of the vortices have been shown in Figure 5.1.17. For the tested angles of attack the delays in the coupling locations ranged from 0.25 X/C at 20 degrees to 0.1 X/C at 26 degrees angle of attack.

The fourth ranked blowing configuration for the short

strakes used blowing tangential to the leading edge of the strake. Blowing was initiated along the strake surface at blowing port number one. For this case, the vortex breakdown locations as a function of the model angle of attack have been shown in Figure 5.1.10. No change in the wing vortex breakdown locations were found over the tested angles of attack. The effect of this fourth ranked blowing case on the strake vortex breakdown locations revealed an increase in effectiveness at the two highest angles of attack. At 28 degrees angle of attack the strake vortex breakdown location was delayed 0.15 X/C, while at 36 degrees angle of attack the delay in the breakdown location increased to 0.2 X/C. Delays in the coupling locations have been shown in Figure 5.1.18. As expected, the delays in the coupling locations at each tested angle of attack remained consistent in magnitude with the minimum and maximum delays being 0.15 X/C and 0.25 X/C respectively. Table 5.1.1 contains a list of the geometries of the four best blowing configurations for both the long and short strakes.

In addition to the graphical evidence of the delays in the breakdown and coupling locations as determined from the video tapes of each individual blowing variation, also provided were 35mm photographs for the two best blowing variations of the long strakes. Photographs were taken at selected X/C locations at model angles of attack of 20 and 24 degrees. These photographs were taken from a 3/4 right side rear view of the fighter model, as shown schematically in Figure 5.1.19, and

show visually the vortex cores over the left wing of the model. This position behind the model allowed for a view of the strake and wing vortex cores over the entire chord of the wing. The cores of the vortices are observed as dark voids in the light sheet, as have been shown in Figures 5.1.20 and 5.1.21 for the 20 degrees angle of attack cases and in Figures 5.1.22 and 5.1.23 for the 24 degree angle of attack cases.

As previously discussed, the best two blowing configurations for the long strakes consisted of blowing at blowing port one. The top ranked blowing case used the shorter 35 degree angled nozzles and blowing on the strake surface. The second ranked blowing variation used the longer blowing nozzles that allowed for blowing tangential to the leading edge of the strakes, and a jet inclination angle of 10 degrees. Figures 5.1.3, 5.1.4, 5.1.11, and 5.1.12 show graphically the effects of these best two blowing variations for the long strakes on the breakdown and coupling locations of the wing and strake vortices.

The X/C locations which have been shown in the photographs for the best blowing variation at 20 degrees angle of attack are 0.4, 0.55, and 0.75 X/C. At each X/C location, photographs of the vortex flow field illuminated by the light sheet were taken both with and without blowing. Figure 5.1.20a shows a view of the 0.4 X/C location without blowing. In this photograph the strake and wing vortex cores are visible just above the left wing. The strake vortex was inboard of the wing vortex and closer to the wing surface. At this angle of attack

and X/C location the vortices are unburst and not coupled. Figure 5.1.20b shows the same X/C location with blowing for the top ranked blowing configuration for the long strakes. Blowing has moved the strake vortex upward and inboard while the wing vortex remained essentially stationary. The strake vortices were moved upward away from the wing surface enough to allow the strake vortex above the right wing to also be visible in the photograph.

Figures 5.1.20c and 5.1.20d show the no blowing and blowing cases for the best blowing case of the long strakes at an X/C location of 0.55. With no blowing, the cores of the vortices were barely visible. At this X/C location with no blowing, the strake and wing vortices were coupled and burst with the model angle of attack at 20 degrees. Thus in the photograph in Figure 5.1.20c, the strake vortex was the vortex that was farther outboard and closer to the leading edge of the wing. With blowing, the strake and wing vortices were not coupled and no longer at breakdown. In Figure 5.1.20d the strake vortex was restored to a position inboard and above its no blowing position while the wing vortex was restored to a position outboard of its baseline position at this X/C location and 20 degrees angle of attack. The motion of the two vortex cores about one another (coupling) was clearly visible in the video tape records.

Figure 5.1.20e contains the photograph of the vortex flow field with no blowing at an X/C location of 0.75. At this location both of the vortices are no longer visible, being well

beyond breakdown above the left wing. The strake and wing vortex cores were again visible, unburst, and uncoupled with blowing on, as shown in Figure 5.1.20f. In this photograph, the strake vortex was inboard and closer to the wing surface as compared with the wing vortex position.

Comparing the blowing cases using the top ranked blowing variation for the long strakes from Figures 5.1.20b, d, and f, reveals that the wing vortex remained in the same spanwise position, as referenced to the wing span with blowing, at each of the tested X/C locations of 0.4, 0.55, and 0.75 X/C. While the wing vortex remained at approximately the mid span position, the strake vortex moved outboard and closer to the wing surface as the trailing edge of the wing was approached. At the 0.4 X/C location with blowing the strake vortex was well above the wing surface and directly above the root chord of the wing. The strake vortex was closer to the wing surface than the wing vortex with blowing on at the 0.75 X/C location and had moved outboard about 1/10 of the wing span.

The effect of the second ranked blowing configuration for the long strakes on the vortex flow field at 20 degrees angle of attack has been shown in Figure 5.1.21. The X/C locations where photographs were taken of the illuminated vortex flow field were 0.35, 0.5, and 0.7 X/C. With no blowing at the 0.35 X/C location from Figure 5.1.21a, the vortex cores were visible with the strake vortex inboard and closer to the wing surface than the wing vortex core. Blowing moved the strake vortex core away from the wing surface while still remaining inboard

of the wing vortex core. In addition to moving the strake vortex upward, the strake vortex core also became less visible, as shown in Figure 5.1.21b. Possible reasons for the reduced visibility of the strake vortex core due to blowing could be manifested in a tightening of the vortex core as a result of the blowing jet becoming entrained and wrapped around the strake vortex, or perhaps that the blowing jet weakened the strake vortex instead.

Figures 5.1.21c and d are the no blowing and blowing cases for the 0.5 X/C location at 20 degrees angle of attack for the second ranked blowing variation for the long strakes. With no blowing, the vortices are coupled, with the strake vortex outboard of the wing vortex and the wing vortex in the midst of breakdown. Blowing caused the vortices to uncouple and the wing vortex to stabilize to its unburst state. As with the effect of blowing at the 0.35 X/C location, the strake vortex was no longer visible in the photograph of Figure 5.1.21d.

Both the strake and wing vortex were no longer visible and well beyond breakdown with no blowing at the 0.7 X/C location as shown in Figure 5.1.21e. Blowing fully re-established the wing vortex to its unburst state. Figure 5.1.20f shows the effect of blowing at the 0.7 X/C location, and again the strake vortex was not visible with or without blowing. With blowing, the wing vortex again remained in approximately the same mid-span position at each X/C location. Figure 5.1.21f concluded the 35mm photographs for the long strakes at 20 degrees angle of attack. Figures 5.1.22 and 5.1.23 show the

60

corresponding photographs taken of the vortex flow field at 24 degrees angle of attack for the long strakes for the baseline cases and for blowing using the best two blowing variations.

At 24 degrees angle of attack with the long strakes, the wing and strake vortex breakdown locations were respectively 0.4 and 0.5 X/C, while the coupling location was 0.45 X/C. With no blowing at the 0.35 X/C location as shown in Figure 5.1.22a, the strake vortex core was inboard of the wing vortex and closer to the wing surface as compared to the wing vortex core location. Blowing using the top ranked blowing configuration at the 0.35 X/C location moved the strake vortex core away from the wing surface while remaining inboard of the wing vortex core as shown in Figure 5.1.22b. In this photograph the strake vortex cores were visible above both the left and right wings.

Photographs of the vortex flow field at the 0.5 X/C location with and without blowing using the top ranked blowing case at 24 degrees angle of attack have been shown in Figure 5.1.22c and d. The vortex flow field at the 0.5 X/C location without blowing shows the vortices to be coupled and at breakdown. Due to breakdown both of the vortices were barely visible with the strake vortex core being the most visible and located just above the wing surface. With blowing, the strake and wing vortices were restored from breakdown and decoupled, as shown in Figure 5.1.22d. The strake vortex with blowing remained inboard of the wing vortex core and both the wing and strake vortex cores were equidistant from the wing surface.

The effects of using the second ranked blowing configuration for the long strakes on the vortex flow field at 24 degrees angle of attack have been presented in Figure 5.1.23. At the 0.35 X/C location blowing moved the strake vortex core from a position closer to the wing surface than the wing vortex core to a position farther away from the wing surface and above the wing vortex core. With blowing at the 0.35 X/C location, see Figure 5.1.23b, the strake vortex was inboard of the wing vortex core. Both of the cores of the vortices also appear to be smaller due to blowing, which as hypothesized previously could be due to a tightening of the vortex cores.

At the 0.5 X/C location without blowing the cores of the vortices were not visible in the photograph of Figure 5.1.23c. With blowing at the 0.5 X/C location as shown in Figure 5.1.23d both of the vortices were restored from breakdown and coupling. In the photograph the strake vortex core was inboard of the wing vortex core and closer to the wing surface as a result of using the second ranked blowing variation for the long strakes.

For the 24 degree angle of attack cases using the two top ranked blowing cases for the long strakes, the wing vortex core remained essentially stationary with blowing at each tested X/C location. This position of the wing vortex core was again at approximately the mid span position. The strake vortex core moved closer to the wing surface and outboard as the trailing edge of the wing was approached with blowing for both of the two best blowing configurations.

5.2   LASER DOPPLER ANEMOMETRY

Velocity data obtained through the use of laser Doppler anemometry have been concentrated in one plane of data perpendicular to the wing surface for one model blowing configuration. As a result of the relatively small amount of velocity data obtained, the resulting data set could only truly be described as a preliminary data set. The laser velocimetry data was obtained at the 0.45 X/C location along the wing surface. The single model configuration studied during the data taking consisted of the long strakes installed on the model with the optimal blowing tube configuration (35 degree angled blowing tubes on the strake surface) at a model angle of attack of 20 degrees. Using this model configuration, X/C location, and model angle of attack, the behavior of the vortex flow field could easily be investigated for the effects of vortex breakdown and vortex restoration by using pneumatic jet blowing. This is because, as discussed in the previous section, the strake and wing vortices are burst at the 0.45 X/C location with the long strakes at 20 degrees angle of attack with no blowing, while blowing using the best blowing configuration for the long strakes restores both the wing and strake vortices as shown in Figure 5.1.3.

Problems were encountered in obtaining complete files of velocity data in close proximity to the wing surface and model fuselage. The problems in obtaining the complete velocity files were directly related to two weaknesses in the data taking

procedure. One problem was caused by distortions in the Doppler signals due to reflections off of the surface of the model fuselage. Distortion of the laser signal was manifested in an increase in the width of the baseline signal, a resulting decrease in the signal to noise ratio, and eventually a saturation of the photomultiplier tubes. The other problem in the data taking procedure was due to the difficulty in placing seeding particles in the cores of the vortices, which as shown in the flow visualization results are generally also located in close proximity to the wing surface and model fuselage. As the number of seeding particles decreased, the data rate obtained with the laser Doppler anemometer also decreased and eventually approached zero.

Nine types of velocity data (3 mean components, 3 RMS components, and 3 cross correlations) were determined from the laser velocimetry data and presented as a function of the spanwise locations as referenced to the y-axis. Each of the nine calculated results have been given at six vertical locations along the z-axis and 11 locations along the y-axis, as presented in Figures 5.2.1 through 5.2.6. The vertical grid line locations were located at $z/(b/2)$ locations of 1.15, 0.86, 0.72, 0.57, 0.43, and 0.29 as referenced to the z-axis and measured normal to the wing surface. Here $(b/2)$ is the local exposed semispan. This measurement grid has been shown in Figure 5.2.7. Also shown in Figure 5.2.7 are the observed y-z locations of the wing and strake vortex cores both with and without blowing, as determined through flow visualization. Note

that much of the velocity data has been obtained at z/(b/2) locations which were above the observed vortex core locations.

To determine the effects of blowing on the vortical flow field, the blowing and baseline cases have been compared for each respective velocity component at each vertical location above the wing surface. Figure 5.2.1 contains the velocity profiles taken at z/(b/2)=1.15 for the baseline and blowing cases at 20 degrees angle of attack as a function of the spanwise location as referenced to the y-axis. The axial velocity, as a result of blowing, showed significant increases from the baseline case across the inboard and mid-span locations. Only slight variations from the baseline velocities are found for the mean spanwise and vertical velocities with blowing. These variations occurred across the inboard wing locations, and resulted in a slight increase in the spanwise velocity and a slight decrease in the vertical velocity.

The RMS turbulence velocities at z/(b/2)=1.15 are presented in Figures 5.2.1 d, e, and f. Blowing resulted in large increases in the axial and spanwise RMS velocities over approximately the inboard 80 percent of the wing span. Increases also occurred in the vertical RMS velocity, but these were smaller in magnitude than the axial and spanwise RMS velocities, and occurred over the inboard 50 percent of the wing span. Cross correlations are presented in Figures 5.2.1 g, h, and i and are not significant at this z location; units of the cross correlations are m^2/sec^2. As expected, due to the absence of shear flow in close proximity to the freestream, the uv, uw,

65

and vw Reynolds stresses were essentially zero across the wing span at this 0.45 X/C location without blowing and show little change as a result of blowing.

The velocity data taken at the $z/(b/2)=0.86$ location are presented in Figure 5.2.2. Virtually no change is observed in the mean axial, spanwise, and vertical mean velocities as a result of blowing, as shown in Figures 5.2.2a, b, and c. A small increase was found in the axial RMS velocity located on the inboard 40 percent of the wing span at the 0.45 X/C location. See Figures 5.2.2d, e, and f for the RMS velocity profiles. For the spanwise RMS velocities, blowing resulted in a significant increase in the velocity magnitude across 90 percent of the wing span. The region over which the blowing increased the spanwise RMS velocities included mainly the inboard and mid-span regions of the wing, but also included a small part of the outboard region of the wing span. Only a small inboard region of the wing span shows an increase for the vertical RMS velocity. The remaining regions of the wing span show no variation of the blowing case from the baseline case for the vertical RMS velocity profile. The cross correlations at the $z/(b/2) = 0.86$ location are contained in Figures 5.2.2g, h, and i. For the baseline cases the cross correlations were again zero across the wing span. Blowing causes the generation of small negative uv Reynolds stresses on the inboard 55 percent of the wing span. The uw and vw cross correlations show no variation from the baseline case with blowing.

The velocity profiles obtained at the $z/(b/2)=0.72$ location

have been shown in Figure 5.2.3 for the 0.45 X/C location with blowing using the optimal blowing configuration for the long strakes. Unlike the z/(b/2)=0.86 and 1.15 locations, blowing caused regions of decreased velocities in addition to regions of increased velocities from the baseline case as shown in the mean velocity profiles; see Figures 5.2.3a, b, and c. With blowing, the axial mean velocity profile had a small region of increased velocity across the inboard 35 percent of the wing span. As compared with the baseline case, the spanwise mean velocity profile had a region of increased velocity on the inboard 30 percent of the wing span and a region of decreased velocity over the remaining 70 percent of the wing span. For the vertical mean velocity, smaller magnitude increases occurred over the inboard mid-span of the wing while decreases occurred over the outboard mid-span of the wing.

Figures 5.2.3d, e, and f show the RMS velocity profiles for the z/(b/2)=0.72 location. The axial RMS velocities show no change as a result of blowing. Two regions of increased spanwise RMS velocities occur over the wing span due to blowing. These two regions are located on the outboard 35 percent and the inboard half span of the wing. A region of increased vertical RMS velocity existed over the mid-span of the wing. At z/(b/2) = 0.72, the cross correlations for the baseline case remained virtually zero across the wing span. The cross correlations are shown in Figures 5.2.3g, h, and i. Blowing induced small negative uv Reynolds stresses over a large region of the inboard and outboard locations of the wing span. Little or no variation

from the baseline case was found with blowing for the uw and vw Reynolds stresses.

Figure 5.2.4 shows the mean velocities, RMS velocities, and cross correlations taken at the $z/(b/2)=0.57$ location. The mean velocities are contained in Figures 5.2.4a, b, and c and are again plotted as a function of the wing span locations. With no blowing the axial velocities are constart across the wing span at the freestream velocity of 15 m/s. Blowing caused an increase in the axial mean velocity over the middle and inboard regions of the wing span. Three regions of variation from the baseline case velocities are found with blowing for the mean spanwise velocities. The three regions as measured in percentage of the wing span consist of a decrease over the inboard 10 percent region, an increase over the middle 30 percent, and a small decrease in the mean spanwise velocity over the outboard 60 percent of the wing span. For the vertical mean velocity, a region of increased velocity as a result cf blowing occurred on the inboard 20 percent of the wing span, while the remainder of the wing span experienced a decrease in the mean vertical velocity.

The RMS velocity profiles for $z/(b/2)=0.57$ are contained in Figures 5.2.4d, e, and f. A small increase in the axial RMS velocity profiles and a large increase in the spanwise RMS velocity profiles over the entire wing span were found as a result of blowing. For the vertical RMS velocities with blowing, a considerable increase was found over the mid-span region of the wing. The uv, uw, and vw Reynolds stresses found

at the $z/(b/2) = 0.57$ location above the wing surface are contained in Figures 5.2.4g, h, and i, respectively. As previously found at the $z/(b/2)=1.15$, 0.86, and 0.72 locations, the cross correlations for the baseline case show only small variations from the zero value across the wing span. For the uv Reynolds stresses, blowing creates larger negative cross correlations across the entire length of the wing span. No significant changes from the baseline case uw Reynolds stresses occurred with blowing. A small region of negative vw Reynolds stresses was found as a result of blowing across the mid-span region of the wing.

Results determined at the $z/(b/2)=0.43$ and 0.29 locations above the wing surface are presented in Figures 5.2.5 and 5.2.6. At both of these z locations difficulties in obtaining complete velocity data files were experienced due to their location close to the wing surface, as well as the close proximity of the cores of the vortices to these z locations. The $z/(b/2)=0.43$ location shows no velocity data for the blowing cases over the inboard 30 percent of the wing span. A probable explanation for this lack of data could be the location of the measurement location almost exactly between the location of the wing and strake vortices with blowing and the resulting difficulty in placing the seeding material in either vortex core. At the $z/(b/2)=0.29$ location, no velocity data could be obtained either with or without blowing for the inboard 80 percent of the wing span. This was directly attributed to the reflections of the laser beams off the model fuselage. As a result of the lack of data at the

69

z/(b/2)=0.29 location, no trends or conclusions could be determined for any of the velocity profiles presented in Figure 5.2.6, except to note that the spanwise mean velocity has changed sign relative to all other results, consistent with being located beneath the vortices.

Figures 5.2.5a, b, and c present the mean axial, spanwise, and vertical velocities for the z/(b/2)=0.43 location. No decisive trends between the blowing and baseline cases could be determined from the mean velocity profiles. However for the baseline case of the mean vertical velocity, the decrease in the velocities over the inboard region of the wing span could be attributed to the presence of the wing vortex directly below the z/(b/2)=0.43 location. From the RMS velocity profiles in Figures 5.2.5d, e, and f only small variations from the baseline cases were found for the axial and vertical RMS velocities as a result of blowing. The variations found with blowing in the spanwise RMS velocities consisted of a decrease over the mid-span region of the wing, and a decrease over the outboard region of the wing span. From the cross correlations for the z/(b/2)=0.43 location shown in Figures 5.2.5g, h, and i, the uw and vw Reynolds stresses were not significant. The uv Reynolds stresses showed uncharacteristic spikes in the baseline case over the mid-span of the wing. These spikes were not present in the blowing case for the uv Reynolds stresses. It is not known if these spikes are significant.

A review of the velocity profiles for the blowing cases for each of the six vertical locations revealed the characteristics

of a large single vortex structure. This single vortical structure with blowing was characterized by mean axial velocities greater than the freestream, by spanwise velocities over the left wing positive in a direction towards the fuselage centerline, by vertical velocities positive away from the wing surface on the outboard wing regions, by vertical velocities negative toward the wing surface on the inboard wing regions, and by a general increase in the magnitudes of the turbulent RMS velocities. The lack of evidence of the presence of the two vortex systems that actually exist is explained by the low density of velocimetry data below the $z/(b/2)=0.57$ location. The cores of the strake and wing vortices are found almost exclusively below the $z/(b/2) =0.57$ location at the 0.45 X/C location and 20 degrees angle of attack. Thus the velocity profiles measured during the present investigation are of the upper and outer regions of both the wing and strake vortices, giving the impression of a single vortical structure.

6.0 CONCLUSIONS

The main objective of this investigation was to determine the effects of blowing on the vortical flow field generated by a 55 degree sweep, cropped delta wing model with forebody strakes. Two independent sets of forebody strakes were available for installation on the wing-body model configuration. Flow visualization and laser Doppler anemometry were used to qualitatively and quantitatively evaluate the vortical flow field both with and without the use of blowing. Flow visualization allowed for the determination of the four best blowing configurations for the long and short strakes from the different blowing configurations which were investigated. A constant blowing coefficient referenced to the wing area of 0.016 was used. Laser Doppler anemometry was used to evaluate one plane of the vortex flow field perpendicular to the wing surface both without blowing and with blowing using the best blowing case for the long strakes.

Four hundred different blowing configuration geometries were investigated to determine the configurations with the largest effects on the vortex flow field. The blowing configuration geometries were defined in terms of the blowing port location; the orientation of the blowing (either tangential to the leading edge of the strake or at a 35 degree angle as measured from the plane of the fuselage sides) and the inclination angle of the blowing tube as measured from the plane of the wing and strake surfaces. The four best blowing cases for the long strakes as determined through the use of flow

72

visualization consisted of, respectively: blowing using the 35 degree jet angle at blowing port 1 (the most forward location) with jet on the strake surface, blowing tangential to the leading edge at blowing port 1 with jet inclination angle of 10 degrees, blowing using the 35 degree jet angle at blowing port 2 with jet inclination angle of 30 degrees, and blowing tangential to the leading edge at blowing port 3 with the jet on the strake surface. For the short strakes the four best blowing cases consisted of, respectively: blowing using the 35 degree jet angle at blowing port 1 with jet on the strake surface, blowing using the 35 degree jet angle at blowing port 2 with jet on strake surface, blowing tangential to the leading edge at blowing port 3 with jet inclination angle of 10 degrees, and blowing tangential to the leading edge at blowing port 1 with jet inclination angle of zero degrees.

Flow visualization has documented significant reductions in vortex coupling and significant delays in the strake vortex breakdown locations. The reductions in the vortex coupling as a result of blowing could be attributed to the movement of the strake vortex away from the wing surface and towards the model fuselage. This movement of the strake vortex delayed the vort coupling by inhibiting interaction between the strake vortex and wing vortex. The strake and wing vortex cores, as viewed through the use of the flow visualization, appeared in some of the optimum blowing cases to tighten and become more visually distinct as a direct result of blowing. Although the wing vortex did not experience the same magnitude of delays in the breakdown locations as the strake vortex, it was expected that a

tightening of the vortex cores would indicate a tightening of the general vortex structure and delays in the vortex breakdown locations. This restoration and tightening of the vortex cores as a result of blowing should lead to improvements in aircraft performance, such as increased stability and/or reduced pitch-up tendencies. Also, used asymmetrically, blowing could also result in enhanced control power.

The laser Doppler anemometry data obtained indicated differences between the velocity profiles of the flow field around the vortices experiencing vortex breakdown and the restored vortex flow field with blowing. An increase in the mean axial velocity profiles above the vortex positions was found due to jet blowing, in addition to an increase in the RMS turbulent velocities. These increases were expected to be due to the presence of the blowing jet above the strake vortex. Due to the low density of laser Doppler velocimetry data, velocity measurements both with and without blowing falsely indicated only the presence of a single large vortex structure over the wing; mean velocities were positive upwards near the wing tip, in a direction inboard above the vortex structure, downward near the fuselage, and in a direction outwards very near to the wing surface. The inwards spanwise mean velocity decreased at larger distances above the wing surface; and vertical mean velocity profiles changed sign near mid-span, again indicating a vortex structure. More detailed data in and around the strake and wing vortex cores would be needed to more clearly determine the effects of jet blowing on vortex structure.

7.0 RECOMMENDATIONS

Among the most obvious recommendations to extend the present investigation would be to obtain more detailed laser Doppler velocimetry results, especially in regions in close proximity to the locations of the vortex cores. If possible, a reduction of the laser beam reflections from the model fuselage and insertion of more seeding particles into the vortex cores would increase the quality of the data and the ease in obtaining the velocimetry data. Possible improvements in the laser and seeding techniques could include an off-axis view with the photomultiplier tubes to reduce the reflections, and the placing of seeding particles directly into the blowing jet. Improvements in the flow visualization procedure would include the use of a plastic grid to determine photographically the locations of the vortex cores at all the X/C locations. With the knowledge of the locations of the vortex cores, LDA data could be concentrated around the two vortices. Also, additional planes of LDA data taken at different X/C locations would be recommended, especially at X/C locations in close proximity to the breakdown locations to document the reversal in the axial flow in the vortex core after breakdown.

Changes in the existing fighter model configuration for future similar investigations could include the following: an addition of a vertical tail; changes in the wing and strake planforms; a modification of the model fuselage to install a strain gage balance to measure forces and moments; and adding

the capability of placing the model in yaw, or sideslip. Each of these model changes would allow for an extension of the present investigation to further investigate and quantify the effect of blowing on the vortex flow field, and to add further understanding to the actual physical effects on the vortex structure.

8.0 BIBLIOGRAPHY

1. Polhamus, Edward C., "Application of the Leading Edge Suction Analogy of Vortex Lift to the Drag Due to Lift of Sharp-Edged Delta Wings," NASA Technical Note D-4739, Aug. 1968.

2. Polhamus, Edward C., "Predictions of Vortex Lift Characteristics by a Leading Edge Suction Analogy," J. of Aircraft, Vol. 8, No. 4, 1971, pp. 193-199.

3. Scott, William B., "NASA Adds to Understanding of High Angle of Attack Regime," Aviation Week & Space Technology, May 22, 1989.

4. Wentz, W.H. Jr., "Wind Tunnel Investigations of Vortex Breakdown on Slender Sharp-Edged Wings," Ph. D. thesis, Univ. of Kansas, Lawrence, KS, 1968; also, NASA CR-98737, 1969.

5. Wentz, W.H. Jr., and Kohlman, D.L., "Vortex Breakdown on Slender Sharp-Edged Wings," J. of Aircraft, Vol. 8, No. 3, March 1971, pp. 156-161.

6. Erickson, G.E., and Gilbert, W.P., "Experimental Investigation of Forebody and Wing Leading Edge Vortex Interactions at High Angles of Attack," AGARD-CP-342, July 1983.

7. Hall, Robert M., "Influence of Forebody Cross Sectional Shape on Wing-Vortex Burst Location," AIAA Paper 86-1835, Presented at AIAA 4th Applied Aerodynamics Conference, San Diego, CA, June 9-11, 1986; also J. of Aircraft, Vol. 24, No. 9, Sept. 1987, pp. 645-652.

8. Erickson, G.E., and Brandon, J.M., "On the Nonlinear Aerodynamic and Stability Characteristics of a Generic Chine-Forebody Slender-Wing Fighter Configuration," NASA Technical Memorandum 89447, June 1987.

9. Erickson, G.E., Rogers, L.W., Schreiner, J.A., and Lee, D.G., "Subsonic and Transonic Vortex Aerodynamics of a Generic Forebody Strake Cropped Delta Wing Fighter," AIAA Paper 88-2596, Presented at AIAA 6th Applied Aerodynamics Conference, Williamsburg, VA, June 6-8, 1988.

10. Erickson, G.E., Rogers, L.W., Schreiner, J.A., and Lee, D.G., "Further Studies of the Subsonic and Transonic Vortex Flow Aerodynamics of a Close-Coupled Forebody-Slender Wing Fighter," AIAA Paper 88-4369, Presented at AIAA Atmospheric Flight Mechanics Conference, Minneapolis, MN, Aug. 15-17, 1988.

11. Erickson, G.E., Schreiner, J.A., and Rogers, L.W., "On the Structure, Interaction, and Breakdown Characteristics of Slender Wing Vortices at Subsonic, Transonic, and Supersonic Speeds," AIAA Paper 89-3345, AIAA Atmospheric Flight Mechanics Conference, Boston, MA, Aug. 14-16, 1989.

12. Campbell, James F., "Augmentation of Vortex Lift by Spanwise Blowing," J. of Aircraft, Vol. 13, No. 9, 1976, pp. 727-732.

13. Skow, A.M., and Peake, D.J., "Control of the Forebody Vortex Orientation by Asymmetric Air Injection: (Part A) Application to Enhance Departure/Spin Recovery of Fighter Aircraft and (Part B) Details of the Flow Structure," AGARD-N83-18693, December 1982.

14. Visser, K., Nelson, R., and Ng, T., "A Flow Visualization and Aerodynamic Force Data Evaluation of Spanwise Blowing on Full and Half Span Delta Wings," AIAA Paper 89-0192, Presented at 27th Aerospace Sciences Meeting, Reno, NV, Jan. 9-12, 1989.

15. Bradley, R.G., and Wray, W.O., "A Conceptual Study of Leading-Edge Vortex Enhancement by Blowing," J. of Aircraft, Vol. 11, No. 1, Jan. 1974, pp. 33-38.

16. Bradley, R.G., Whitten, P.D., and Wray, W.O., "Leading-Edge-Vortex Augmentation in Compressible Flow," J. of Aircraft, Vol. 13, No. 4, Apr. 1976, pp. 238-242.

17. Erickson, G.E., "Effect of Spanwise Blowing on the Aerodynamic Characteristics of the F-5E," J. of Aircraft, Vol. 16, No. 10, 1979, pp. 695-700.

18. Malcolm, G.N., and Skow, A.M., "Improved High-α Controllability Through Vortex Manipulation," Eidetics International Report TR-86-101, Jan. 1986.

19. LeMay, Scott P., and Rogers, L.W., "Pneumatic Vortex Flow Control on a 55 Degree Cropped Wing with Chined Forebody," AIAA Paper 90-1430, Presented at AIAA 16th Aerodynamics Ground Testing Conference, Seattle, WA, June 18-20, 1990.

20. Parmenter, K., and Rockwell, D., "Transient Response of Leading-Edge Vortices to Localized Suction," AIAA Journal, Vol. 28, No. 6, June 1990, pp. 1131-1133.

21. Meyers, James F., and Hepner, Timothy E., "Measurement of Leading Edge Vortices From a Delta Wing Using a Three Component Laser Velocimeter," AIAA Paper 88-2024, Presented at AIAA 15th Aerodynamic Testing Conference, San Diego, CA, May 18-20, 1988.

22. Kegelman, J., and Roos, F., "Effects of Leading Edge Shape and Vortex Burst on the Flowfield of a 70 Degree Sweep Delta Wing," AIAA Paper 89-0086, Presented at 27th Aerospace Sciences Meeting, Reno, NV, January 9-12, 1989.

23. Novak, Charles J., Huie, Charles R., and Cornelius, Kenneth C., "Laser Velocimetry in Highly Three Dimensional and Vortical Flows," NASA CP-2416, Vortex Flow Aerodynamics, Vol. 1, October 1985.

24. Sellers, William L. III, Meyers, James F., and Hepner, Timothy E., "LDV Surveys Over a Fighter Model at Moderate to High Angles of Attack," SAE Paper 881448, Presented at Aerospace Technology Conference and Exposition, Anaheim, CA, October 3-6, 1988.

25. Iwanski, K., Ng, T., and Nelson, R., "An Experimental Investigation of Delta Wing Vortex Flow With and Without External Jet Blowing," AIAA Paper 89-0084, Presented at 27th Aerospace Sciences Meeting, Reno, NV, Jan. 9-12, 1989.

26. Tse, Francis S., and Morse, Ivan E., "Measurement and Instrumentation in Engineering," New York, Marcel Dekker, Inc., 1989.

27. John, James E. A., "Gas Dynamics," Boston, Allyn and Bacon, March 1972.

28. Buchave, P., "Three-component LDA Measurements," DISA Information No. 29, Jan. 1984, pp. 3-9.

29. Nichols, C. E., Jr.,"Preparation of Polystyrene Microspheres for Laser Velocimetry in Wind Tunnels," NASA-TM-89163, June 1987.

30. Durst, F., Melling, A., and Whitelaw, J., "Principles and Practices of Laser Doppler Anemometry," 2nd. Edition, New York, Academic Press, 1981.

TABLE 3.2.1   WING GEOMETRY DETAILS

$$AR \qquad 1.867$$

$$b \qquad 35.56 \text{ cm}$$

$$c_r \qquad 28.14 \text{ cm}$$

$$c_t \qquad 6.35 \text{ cm}$$

$$c_m \qquad 17.25 \text{ cm}$$

$$S_{ref} \qquad 0.068 \text{ m}^2$$

$$\Lambda_{LE} \qquad 55^\circ$$

$$\lambda \qquad 0.2$$

Wing Section - flat plate, 0.318 cm thickness

All Wing Edges Sharp with 45° Bevel on Underside

TABLE 3.2.2   LOCATIONS OF BLOWING PORTS

BLOWING PORTS	LONG STRAKES x/c	SHORT STRAKES x/c	FUSELAGE x/L
1	0.3	0.113	0.198
2	0.51	0.379	0.284
3	0.893	0.865	0.440
4	-----	-----	0.600

80

TABLE 5.1.1   **GEOMETRY DETAILS OF FOUR BEST BLOWING CONFIGURATIONS**

Long Strakes

	Blowing Port	Blowing Orientation	Jet Inclination Angle
1.	#1	$35°$ Jet Angle	$-10°$
2.	#1	Tangential to Leading Edge	$10°$
3.	#2	$35°$ Jet Angle	$30°$
4.	#3	Tangential to Leading Edge	$-10°$

Short Strakes

	Blowing Port	Blowing Orientation	Jet Inclination Angle
1.	#1	$35°$ Jet Angle	$-10°$
2.	#2	$35°$ Jet Angle	$-10°$
3.	#3	Tangential to Leading Edge	$10°$
4.	#1	Tangential to Leading Edge	$0°$
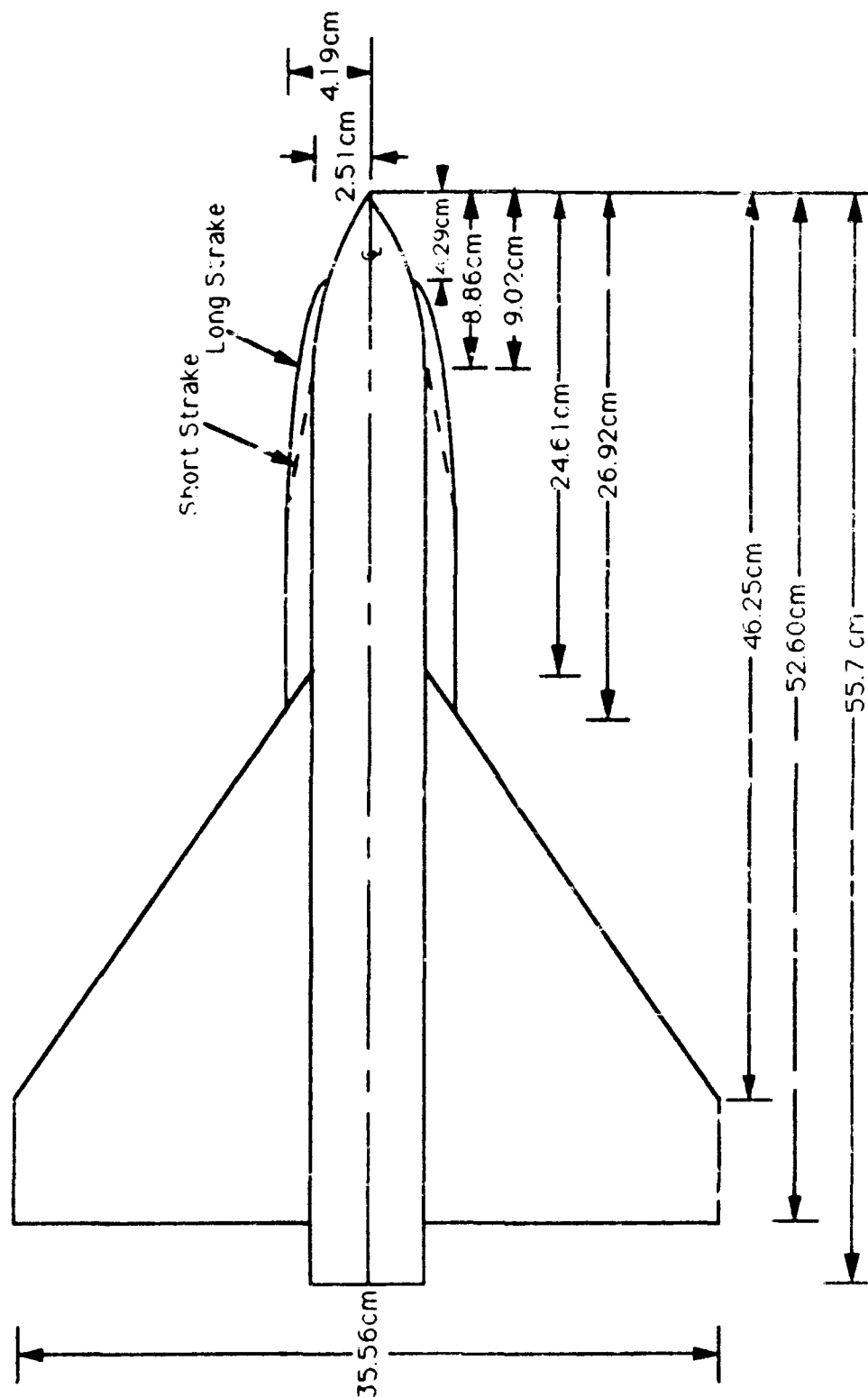
Figure 3.2.1. Schematic of Tailless, Generic Fighter Configuration Model.

(a) top view

82

Figure 3.2.1. Continued.

(b) side view

83

5.72cm

0.32cm

Blowing Tube

2.51cm

4.19cm

0.64cm below
₵ to ₵ of wing

0.24cm below ₵

17.79cm
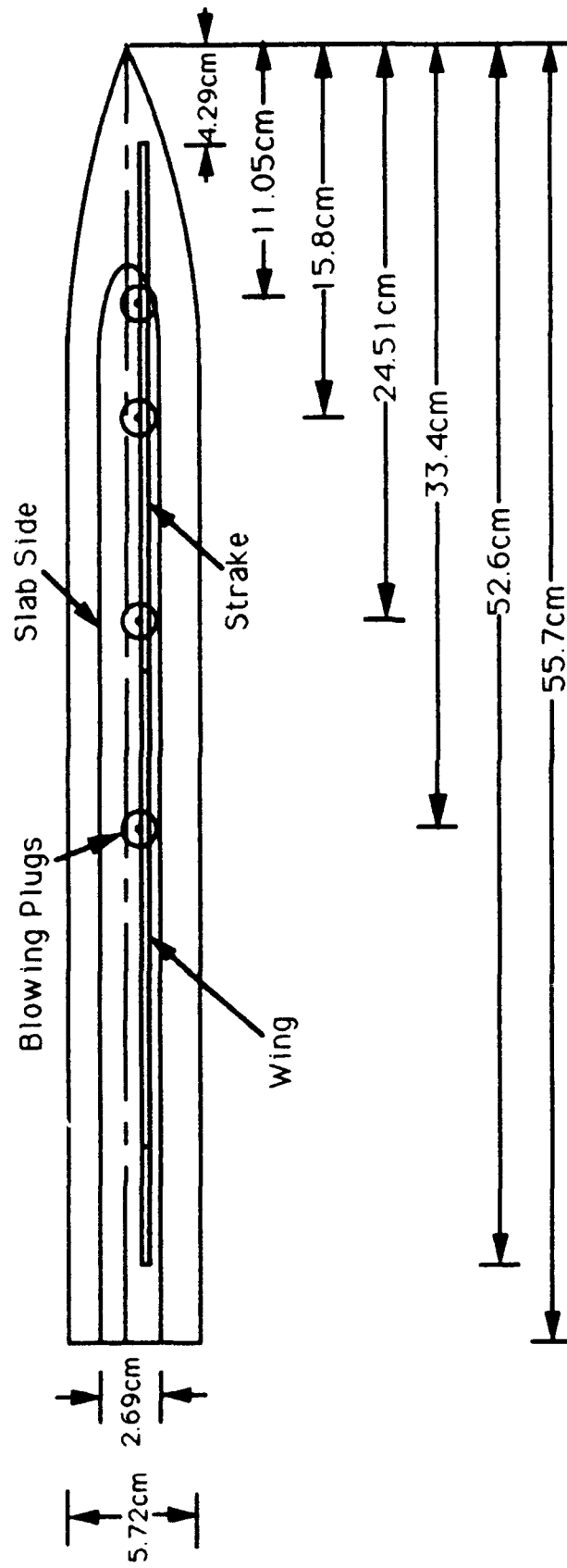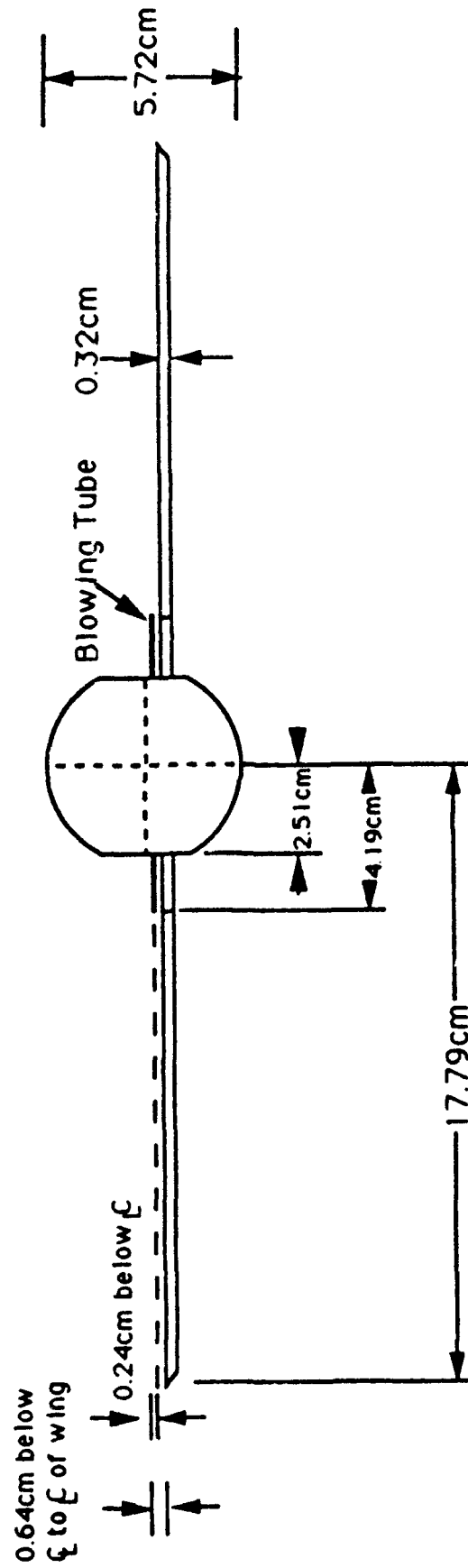
(c)   front view

Figure 3.2.1.   Concluded.
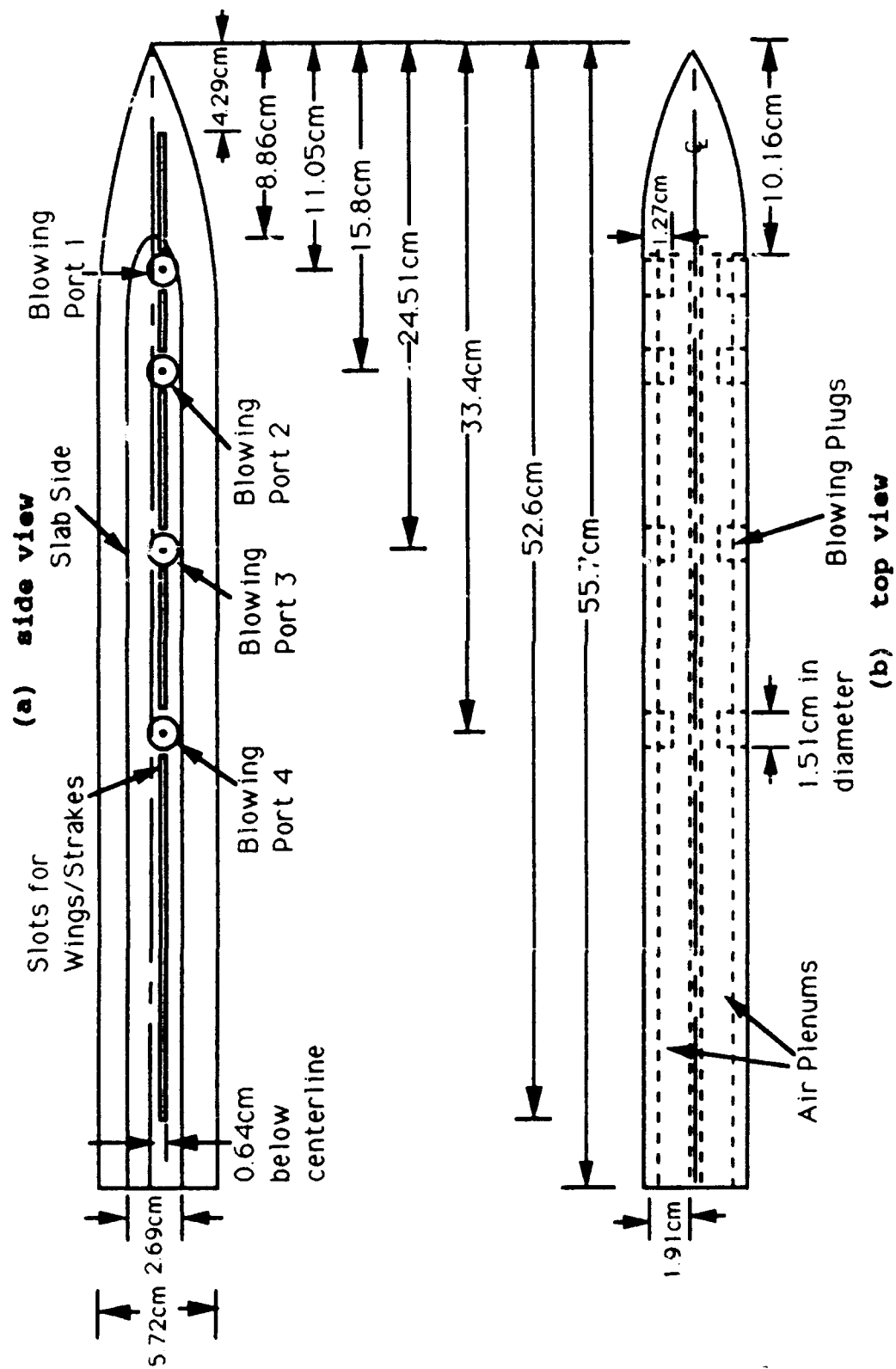
Figure 3.2.2. Schematic of Fuselage of Model.

85
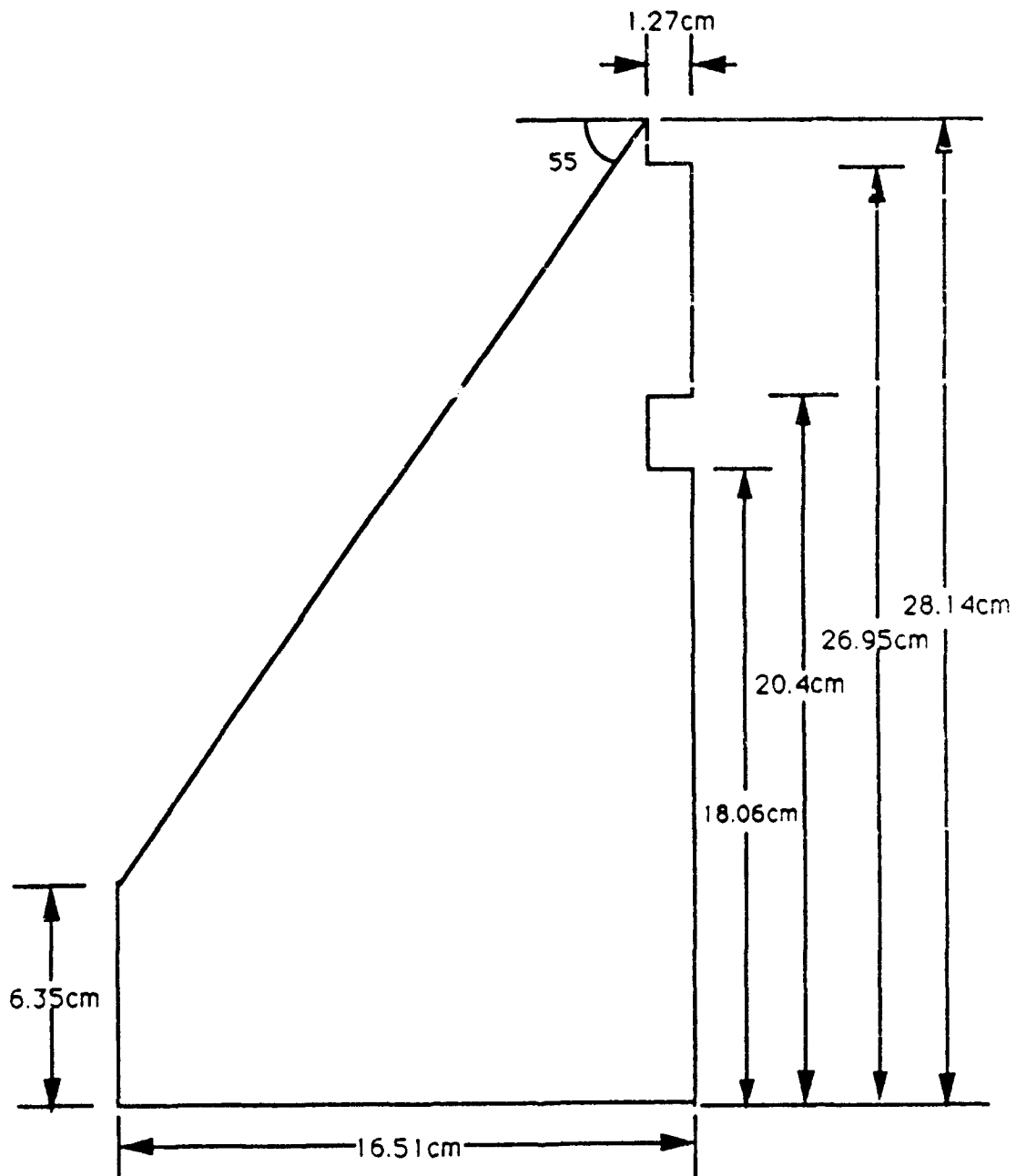
Figure 3.2.3. Schematic of Wing Planform for Model.
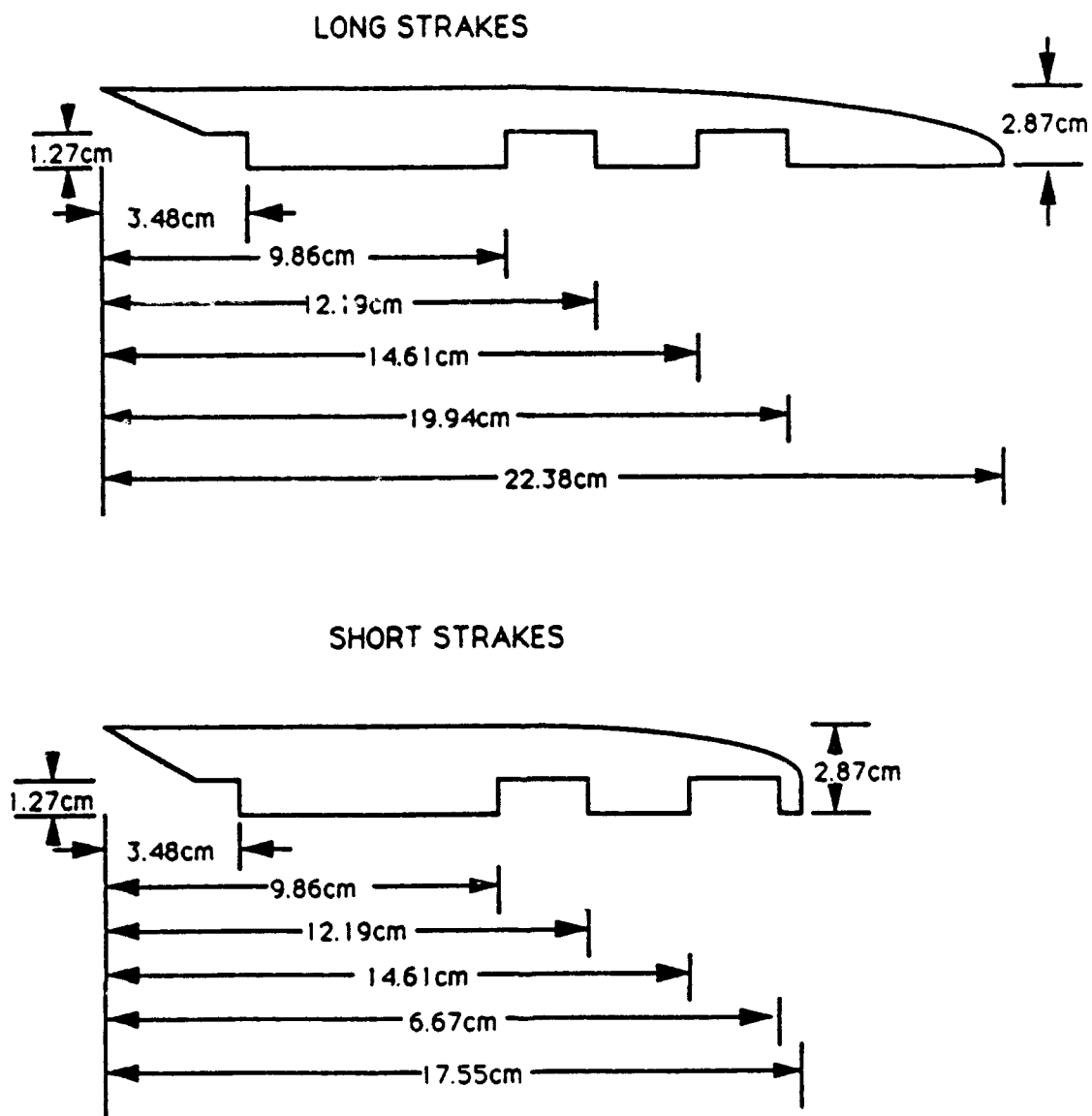
Figure 3.2.4. Schematics of Strake Planforms for Model.
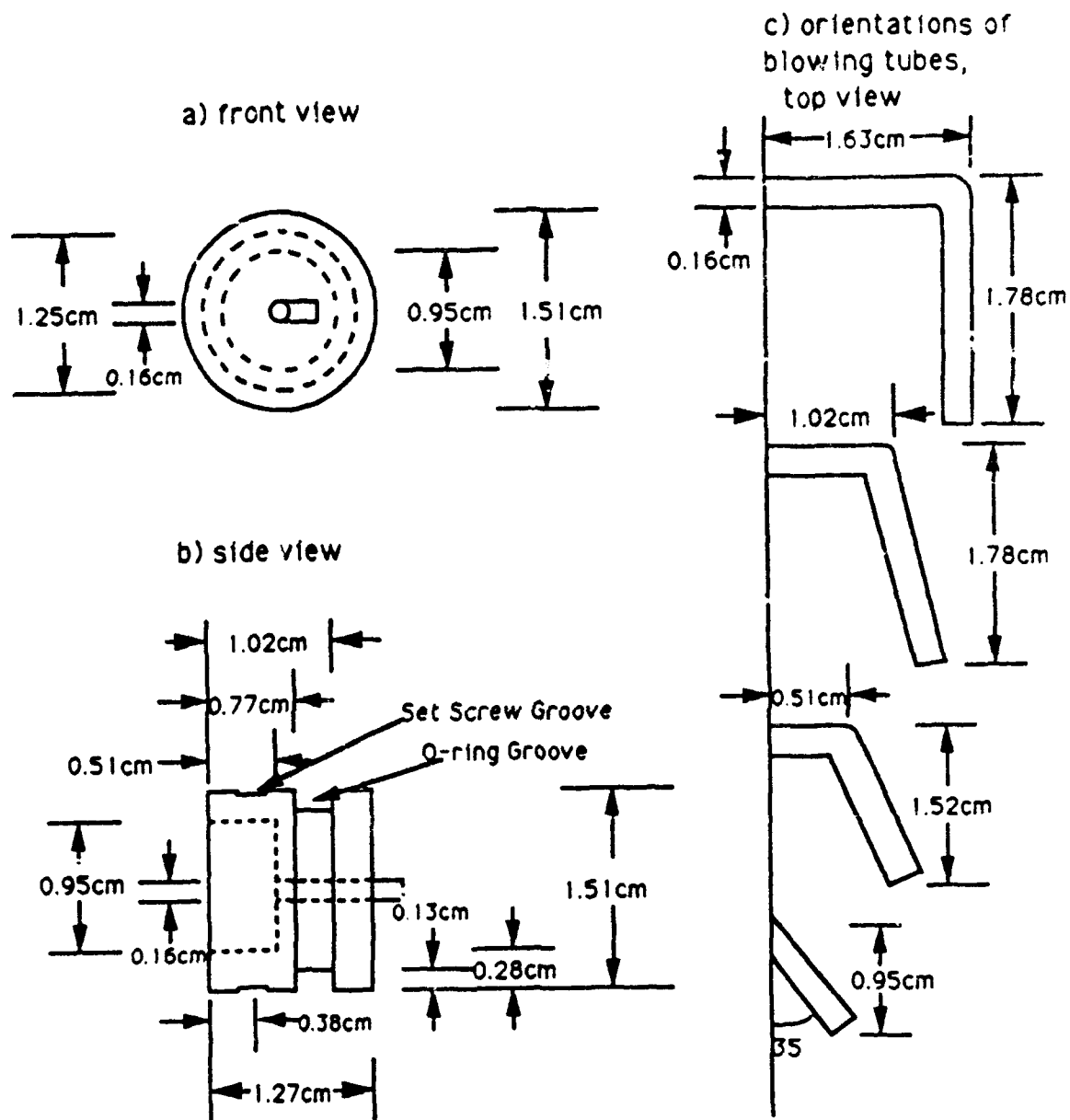
Figure 3.2.5. Schematic of Blowing Plugs and Orientations of Blowing Tubes.

88
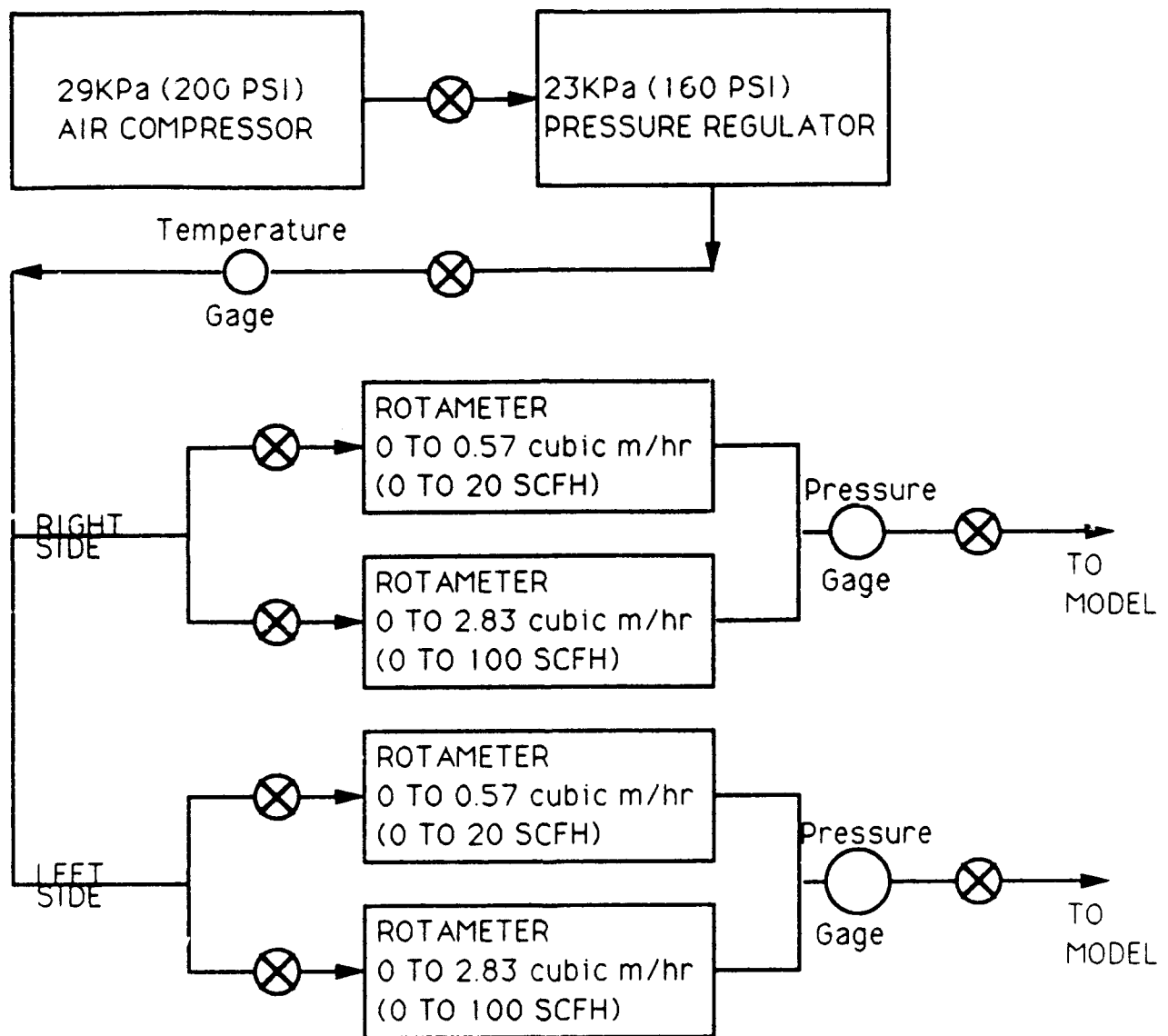
Figure 3.2.6. Block Diagram of Flow Control Hardware for Blowing.
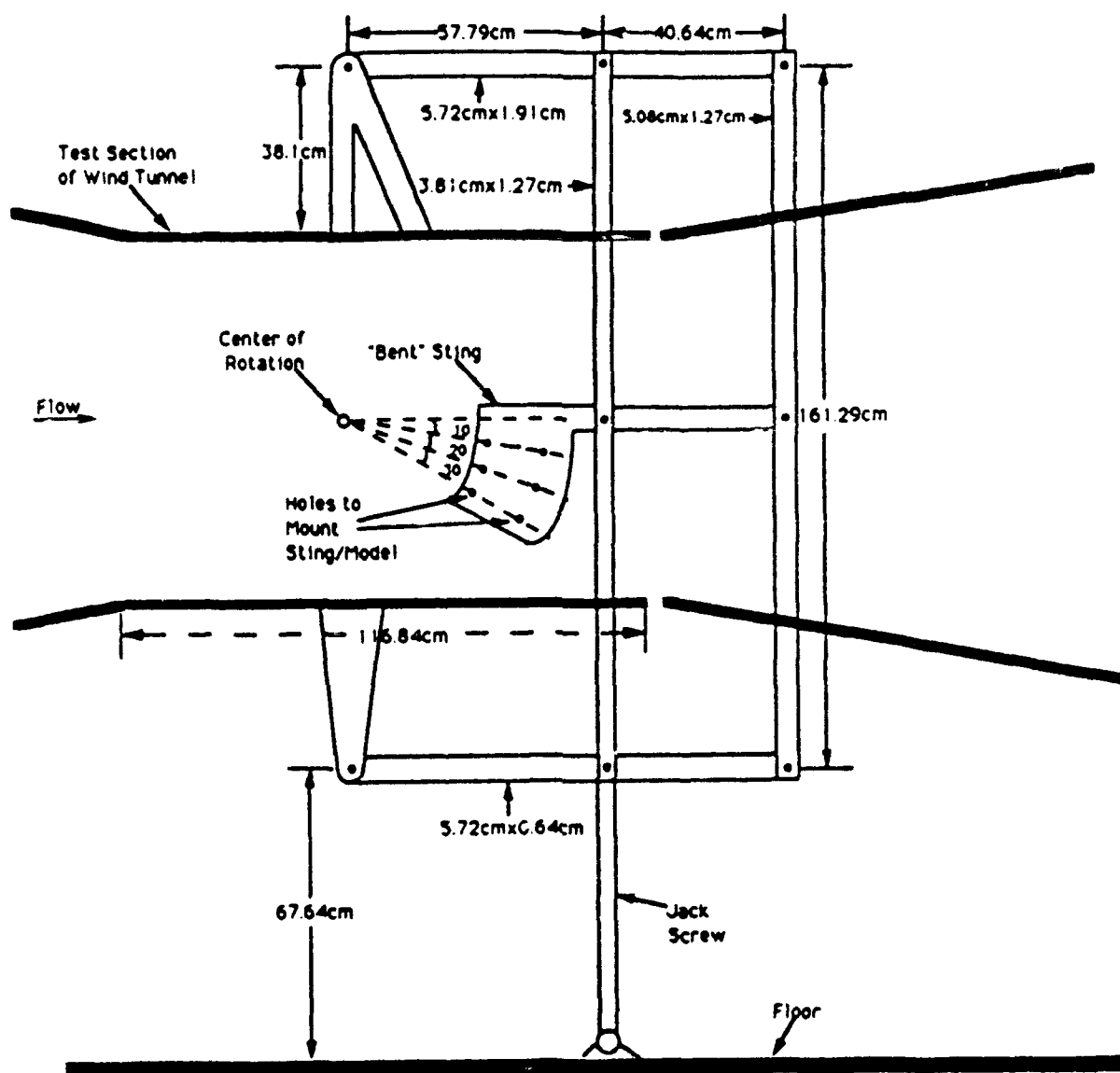
Figure 3.2.7. Schematic of Sting and Angle of Attack Mechanism Located in West Virginia University Low Speed Wind Tunnel.

90
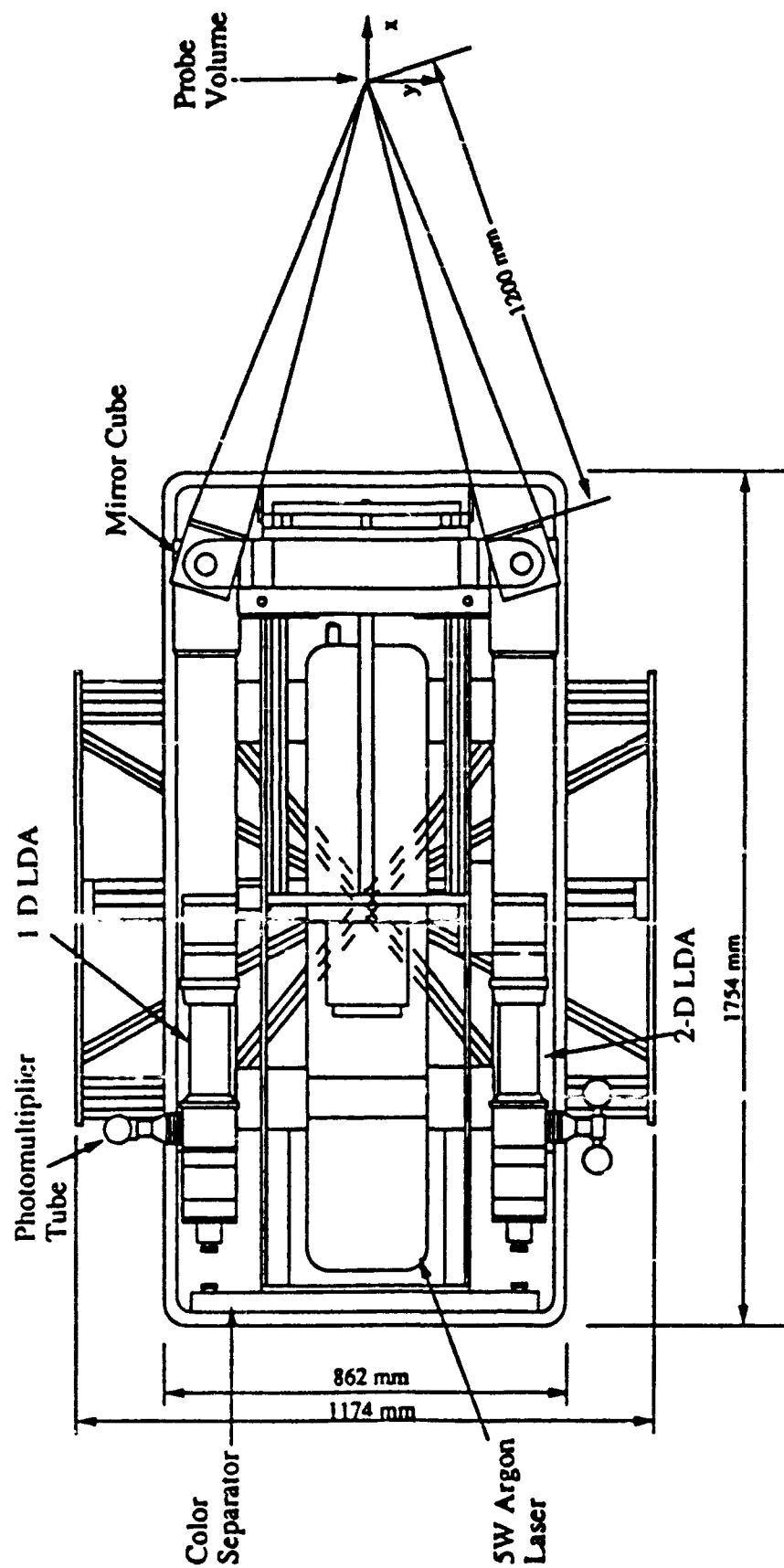
Figure 3.3.1. Schematic of Complete Three-Component Laser Doppler Anemometer System.
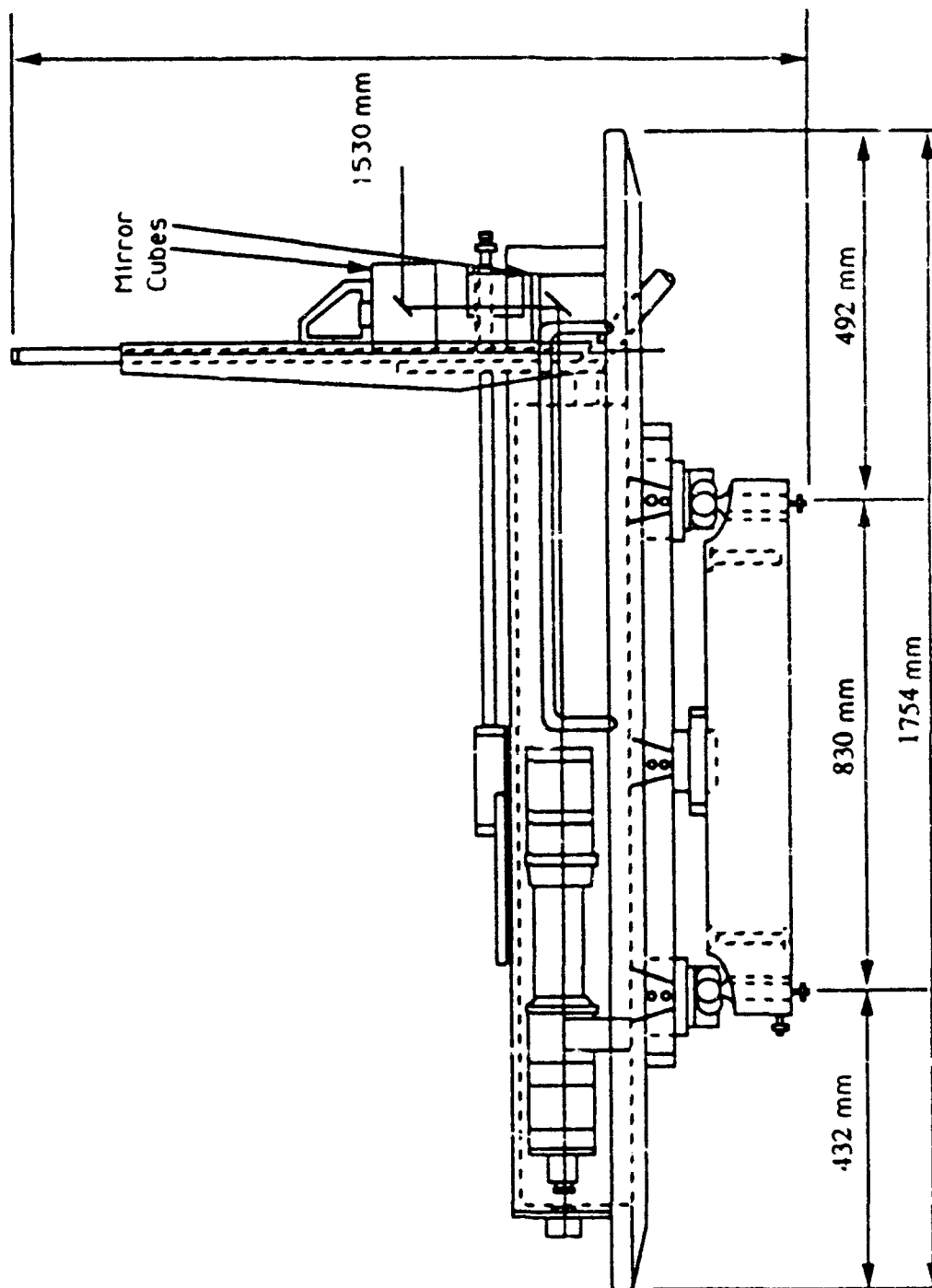
a) top view

Figure 3.3.1. Continued.

b) side view

1530 mm

Mirror Cubes

492 mm

830 mm

1754 mm

432 mm
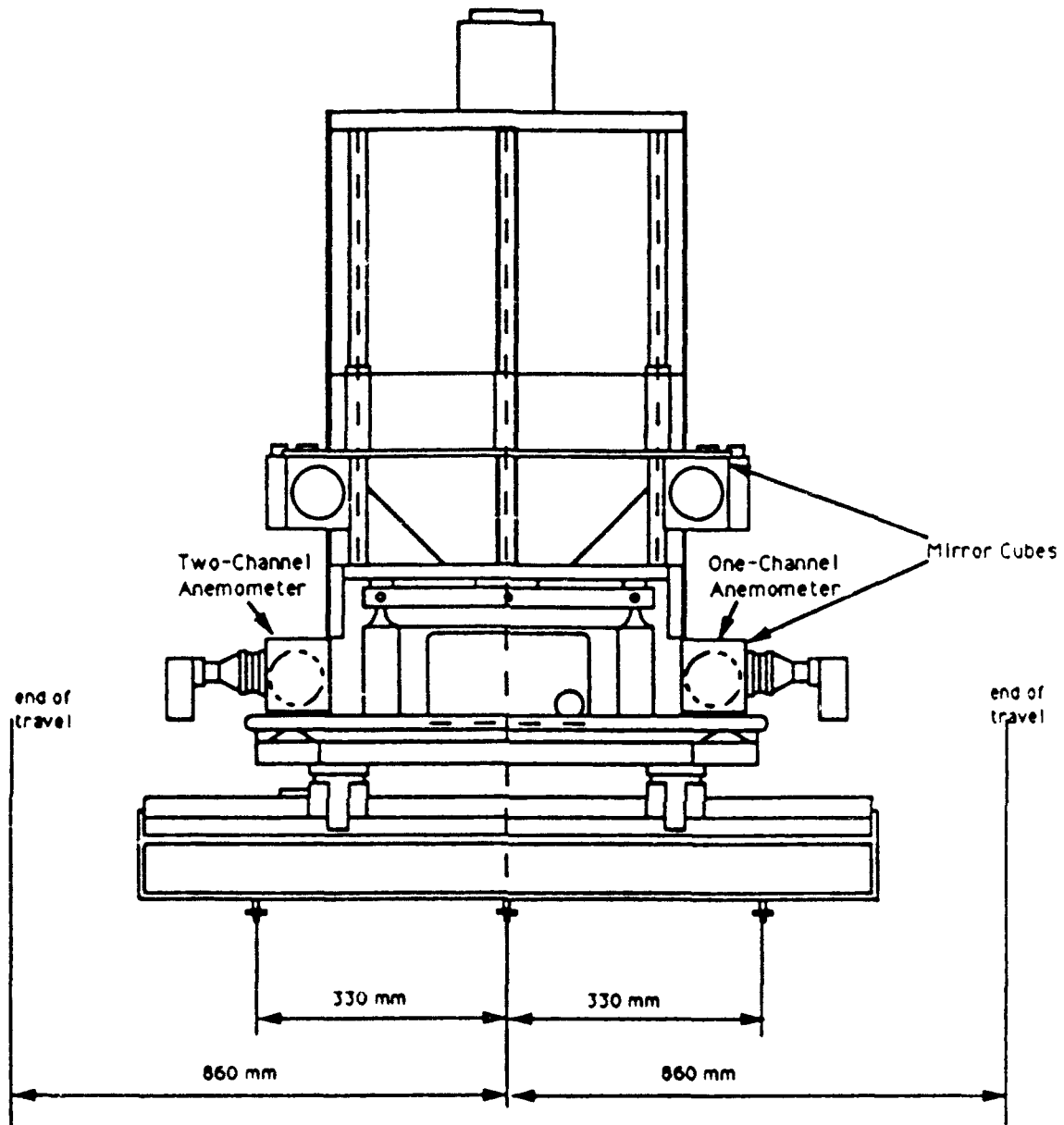
c) front view

Figure 3.3.1. Concluded.

Plexiglas Window

Test Section Door

97.79cm

66.04cm

Upstream

99.06cm

121.92cm

107.95cm

Note: Test Section is 119.38cm in width
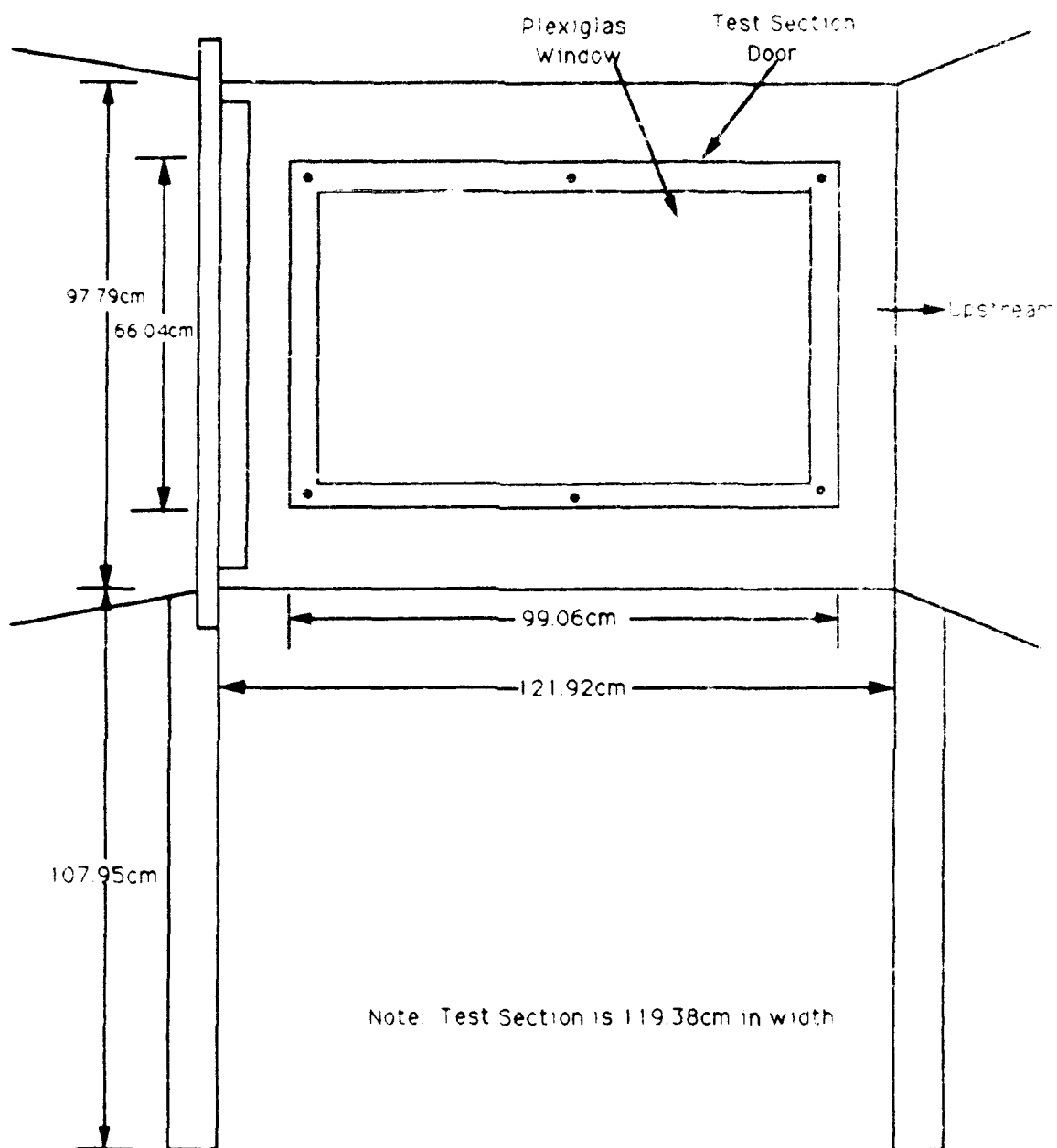
Figure 3.4.1.   Schematic of Test Section of West Virginia University Low Speed Wind Tunnel.
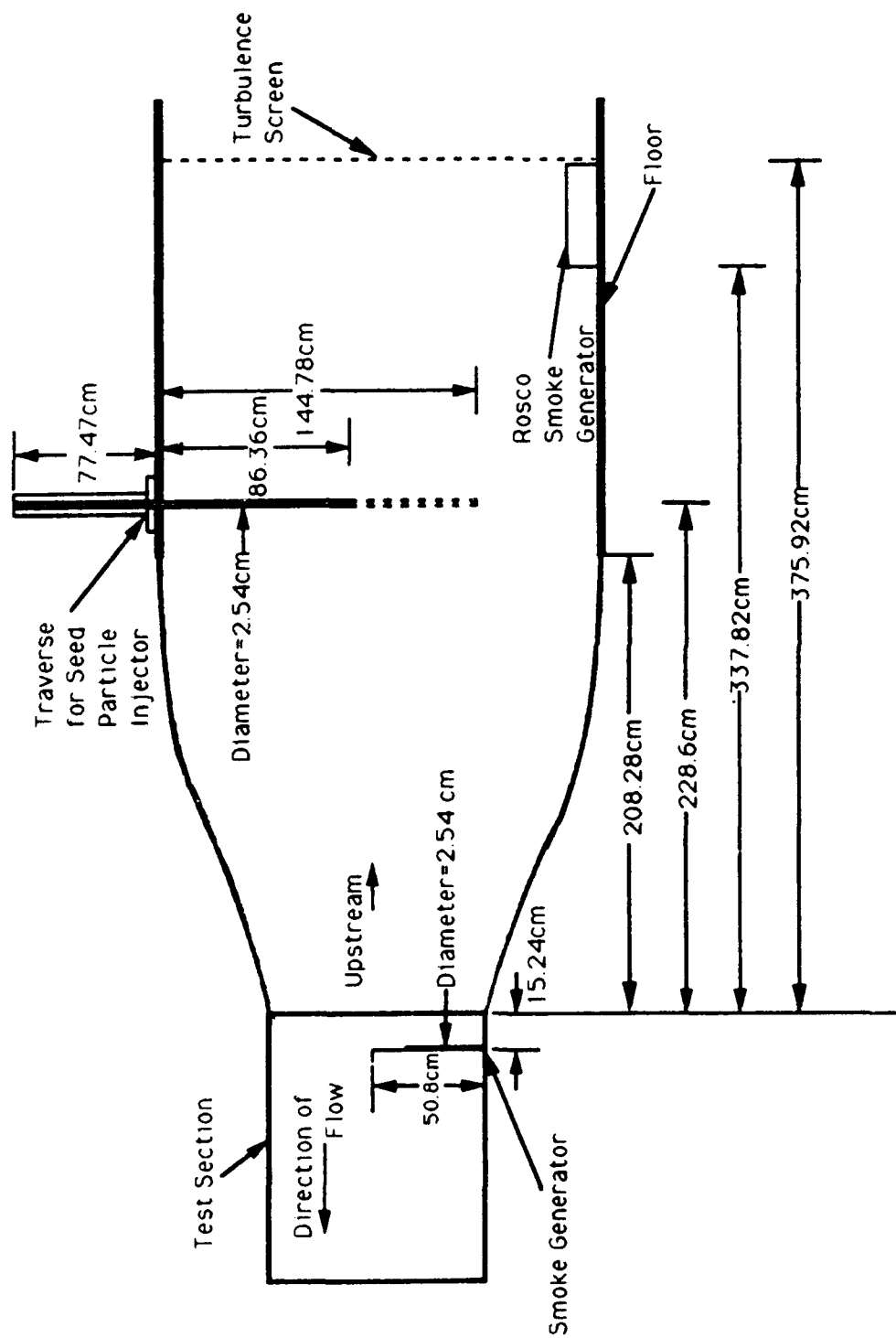
Figure 3.4.2. Schematic Showing Location of Smoke Generators in the West Virginia University Low Speed Wind Tunnel.

95
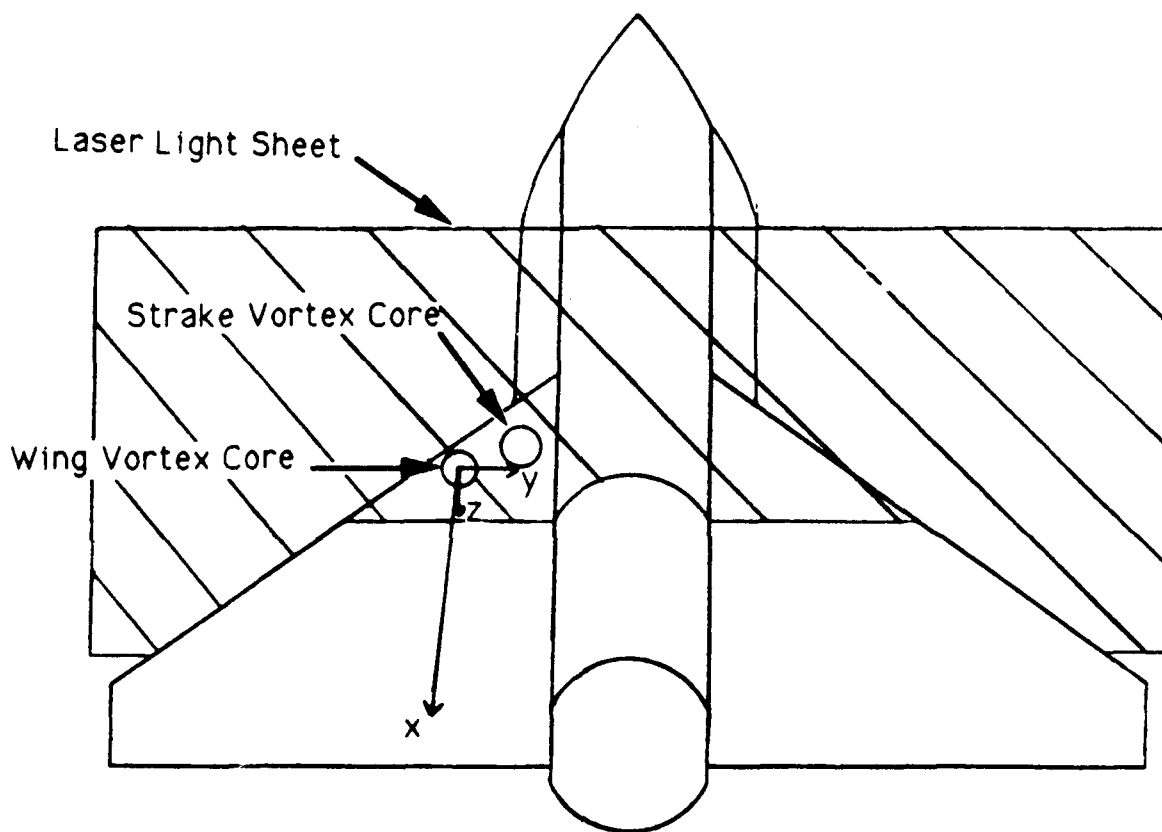
Figure 4.1.1   Schematic Showing Axis System Used To Determine Coupling.
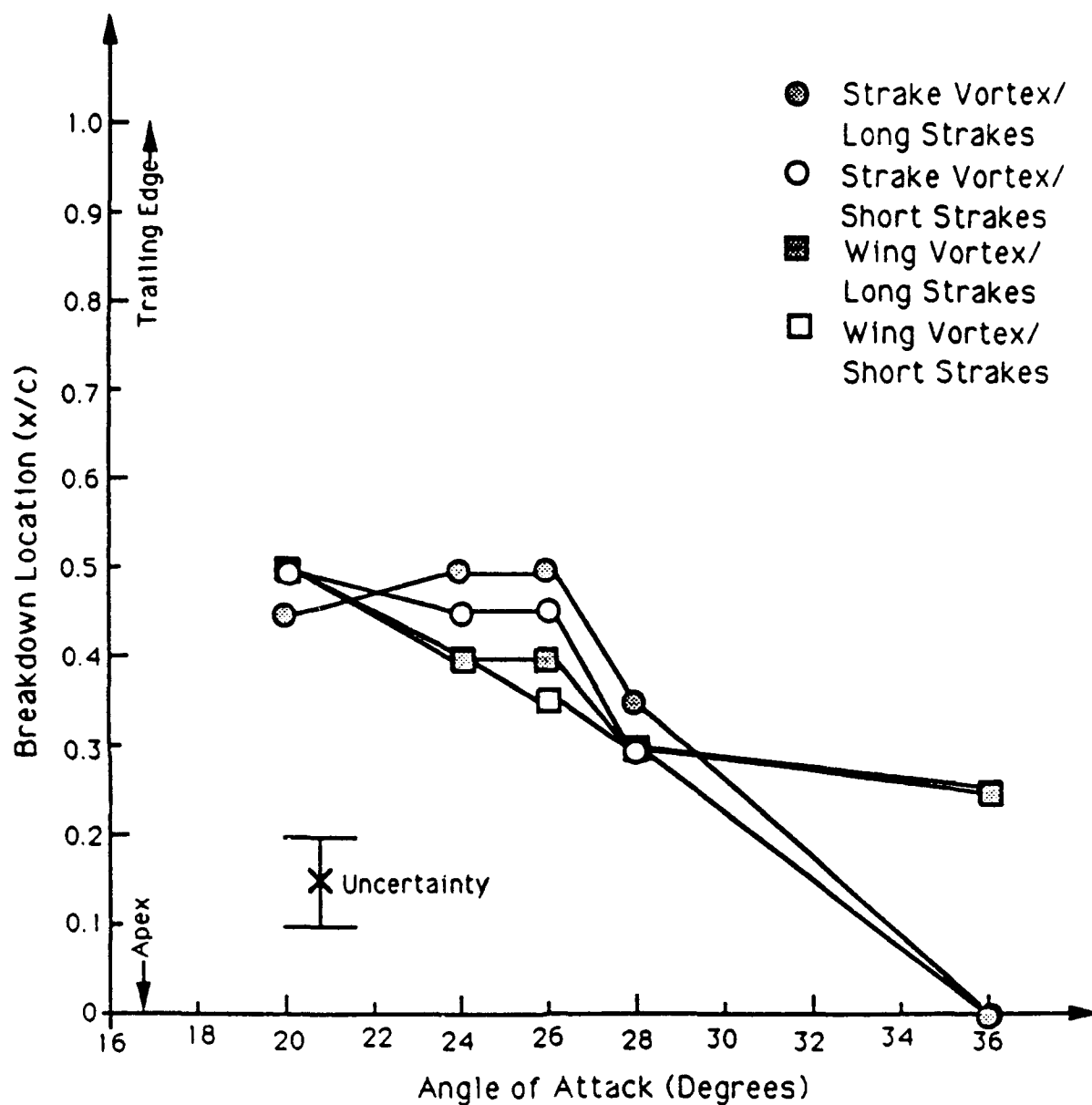
Figure 5.1.1   Vortex Breakdown Locations Versus Angle of
                Attack for Short and Long Strakes with No
                Blowing.
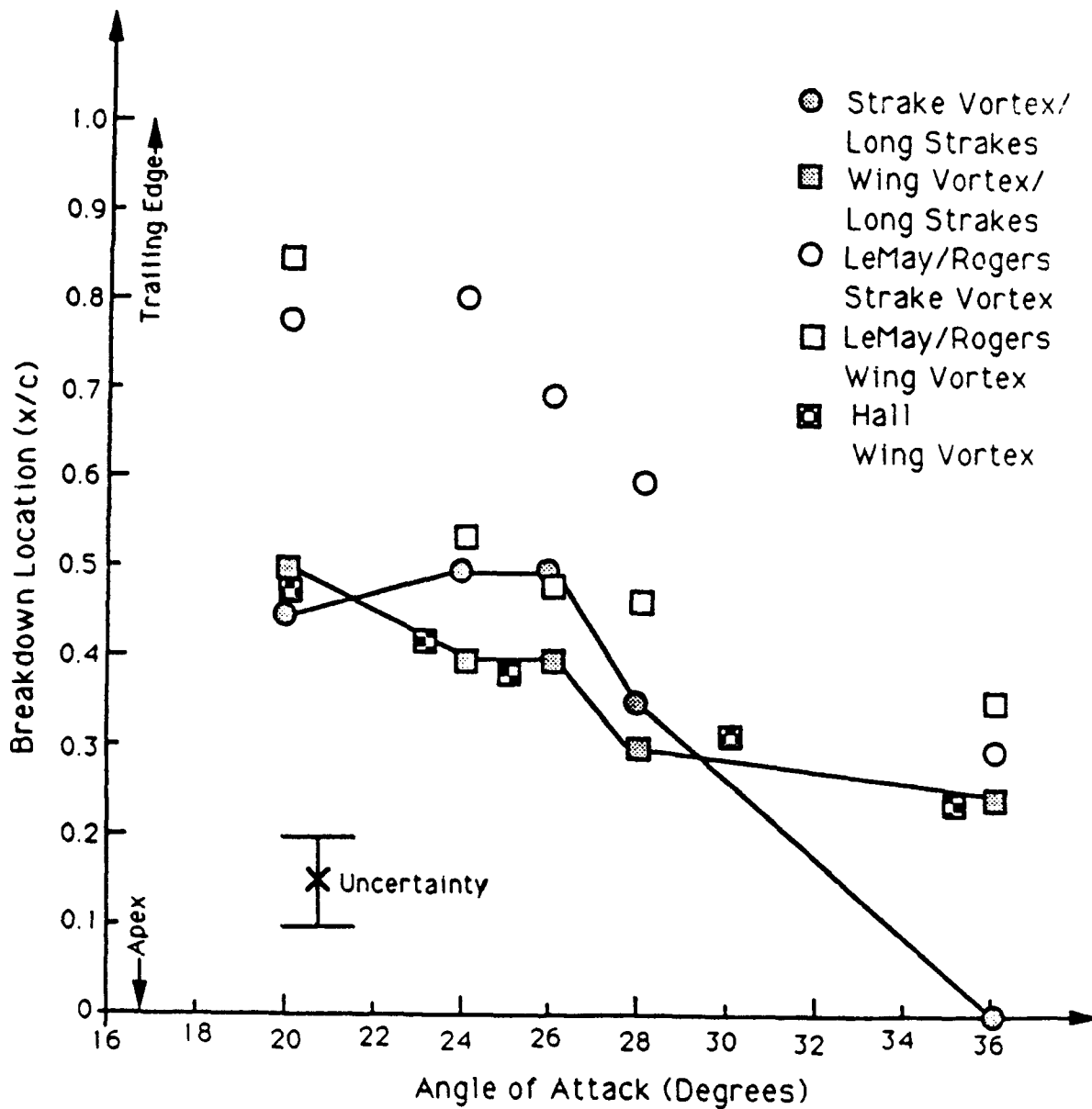
Figure 5.1.2 Comparison with Similar Investigations of Vortex Breakdown Locations Versus Angle of Attack for No Blowing.
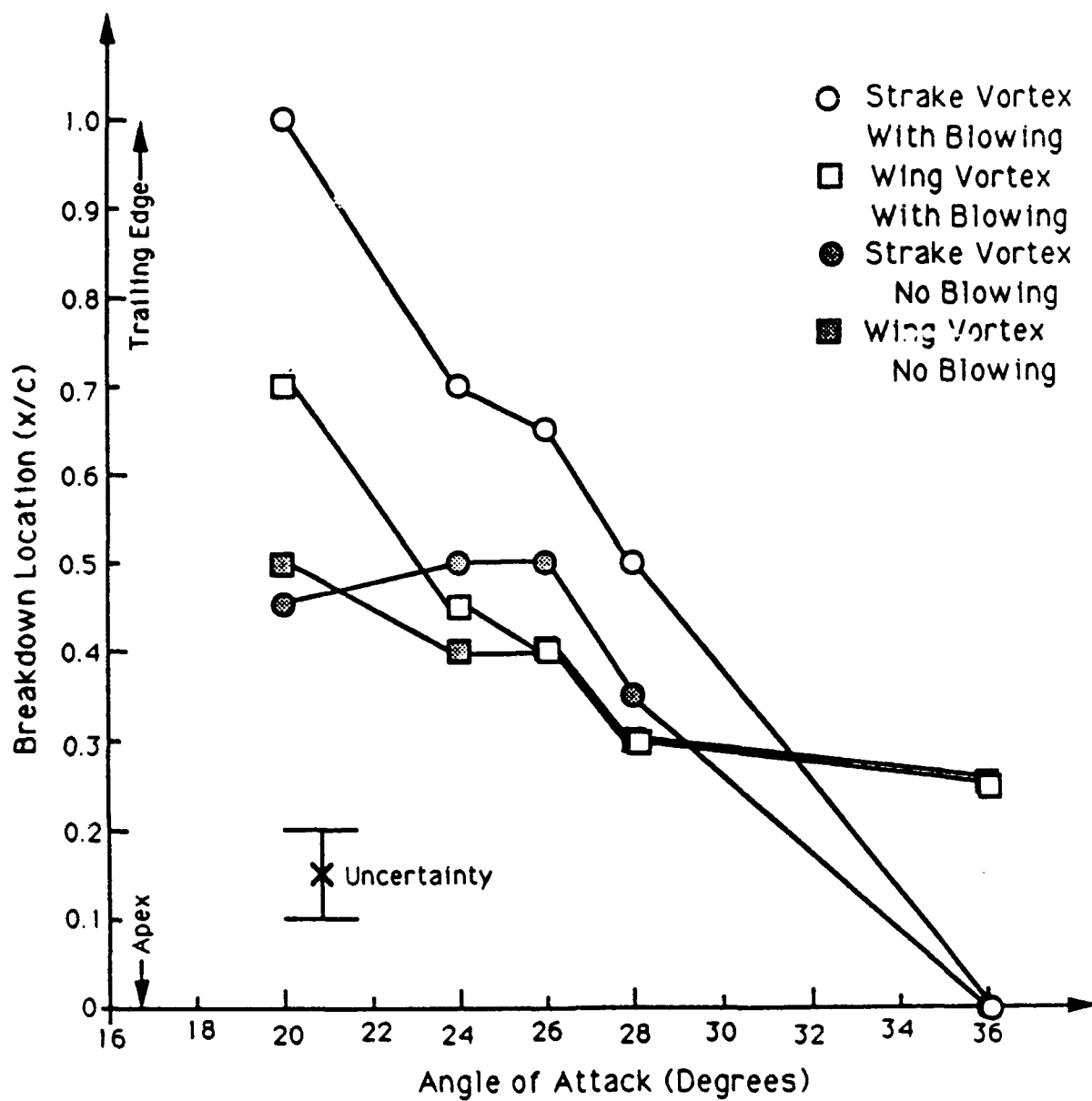
Figure 5.1.3   Vortex Breakdown Locations for Long Strakes
                Versus Angle of Attack for No Blowing and for
                Blowing Using 35 Degree Jet Angle at Blowing
                Port 1 with Jet on Strake Surface, C_μ=0.016.

99
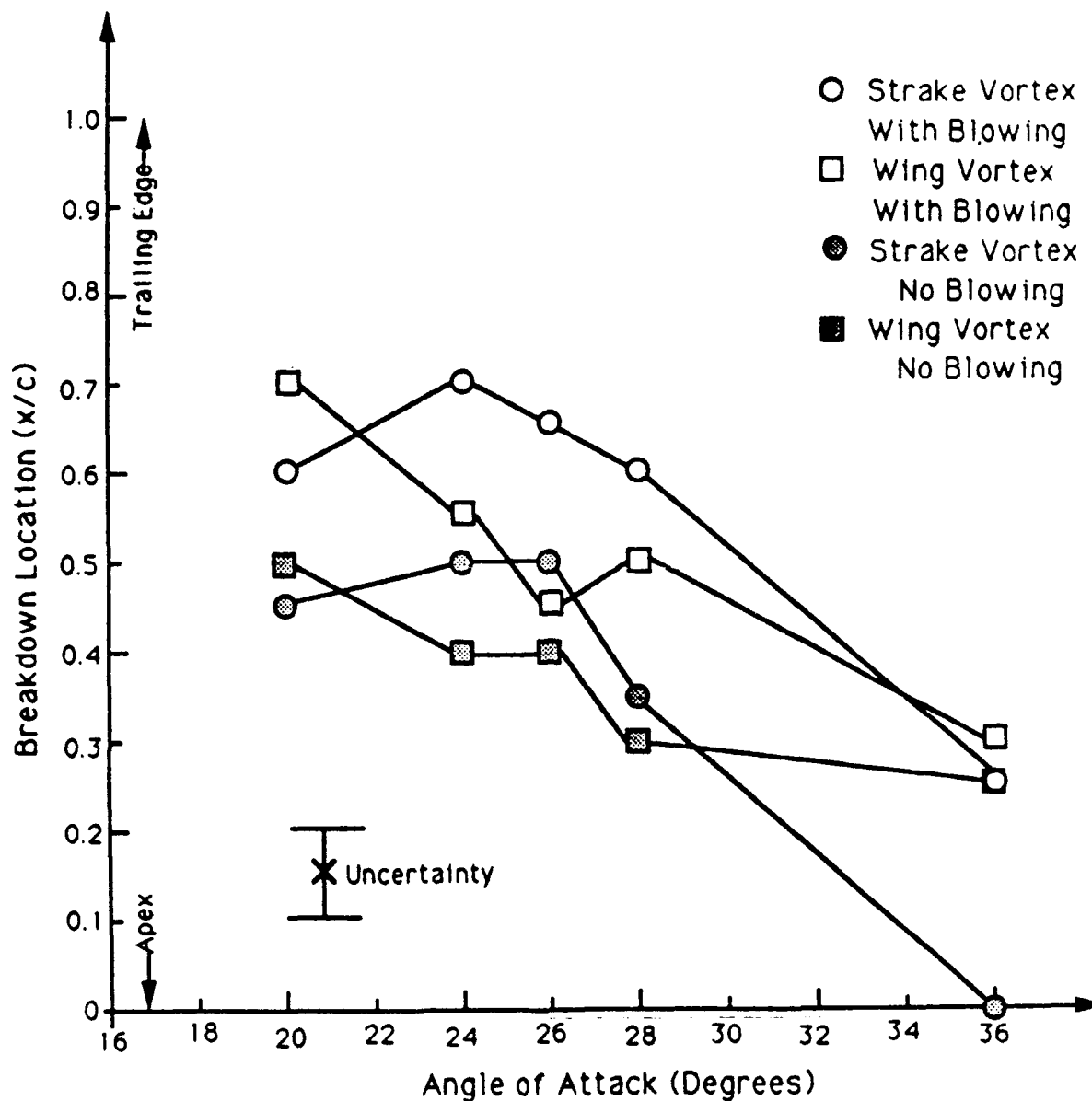
Figure 5.1.4   Vortex Breakdown Locations for Long Strakes
Versus Angle of Attack for No Blowing and for
Blowing Tangential to the Leading Edge at
Blowing Port 1 with Jet Inclination Angle of 10
Degrees, C_μ=0.016.

100
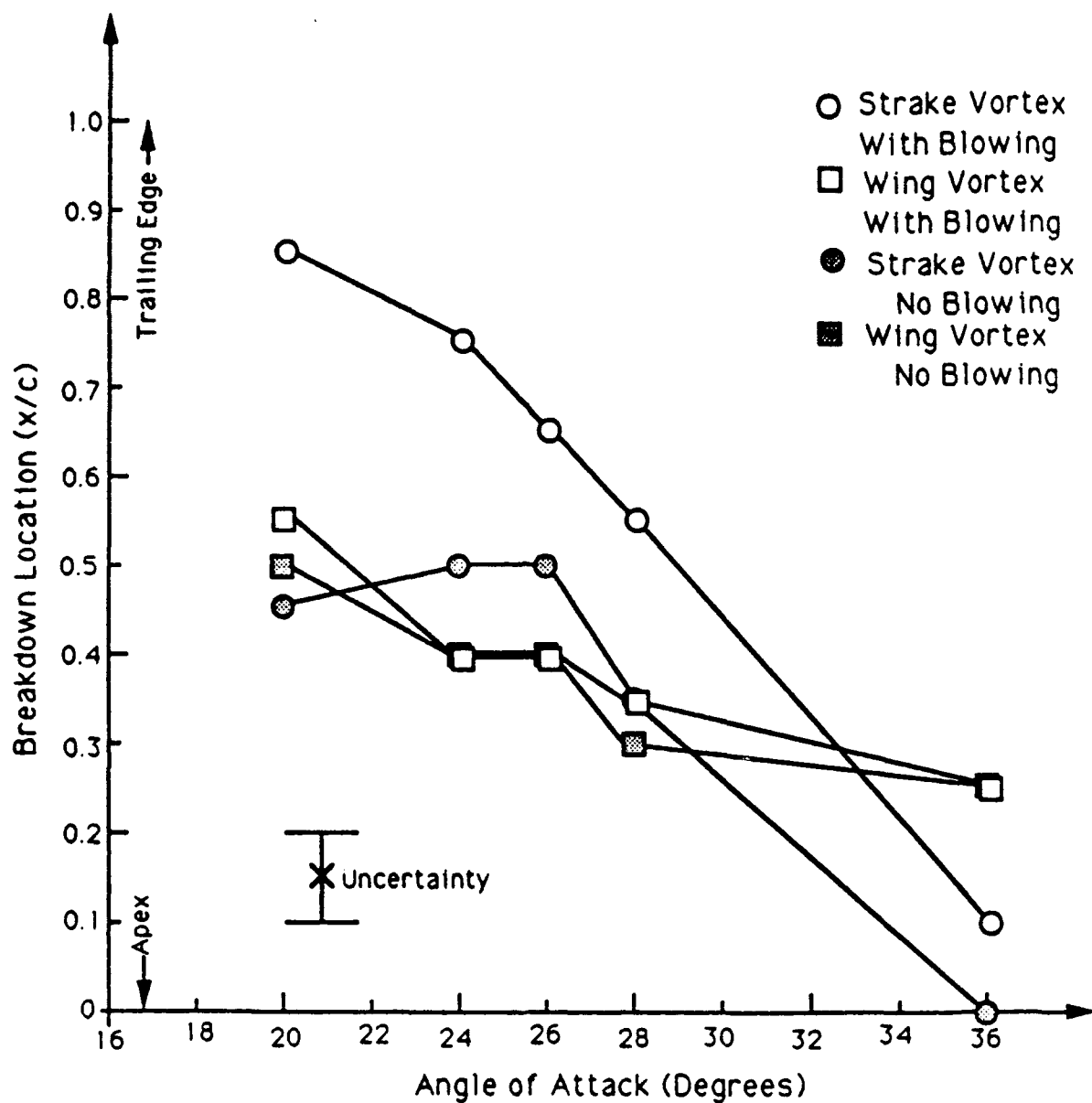
Figure 5.1.5   Vortex Breakdown Locations for Long Strakes
Versus Angle of Attack for No Blowing and for
Blowing Using 35 Degree Jet Angle at Blowing
Port 2 with Jet Inclination Angle of 30 Degrees,
C_μ=0.016.
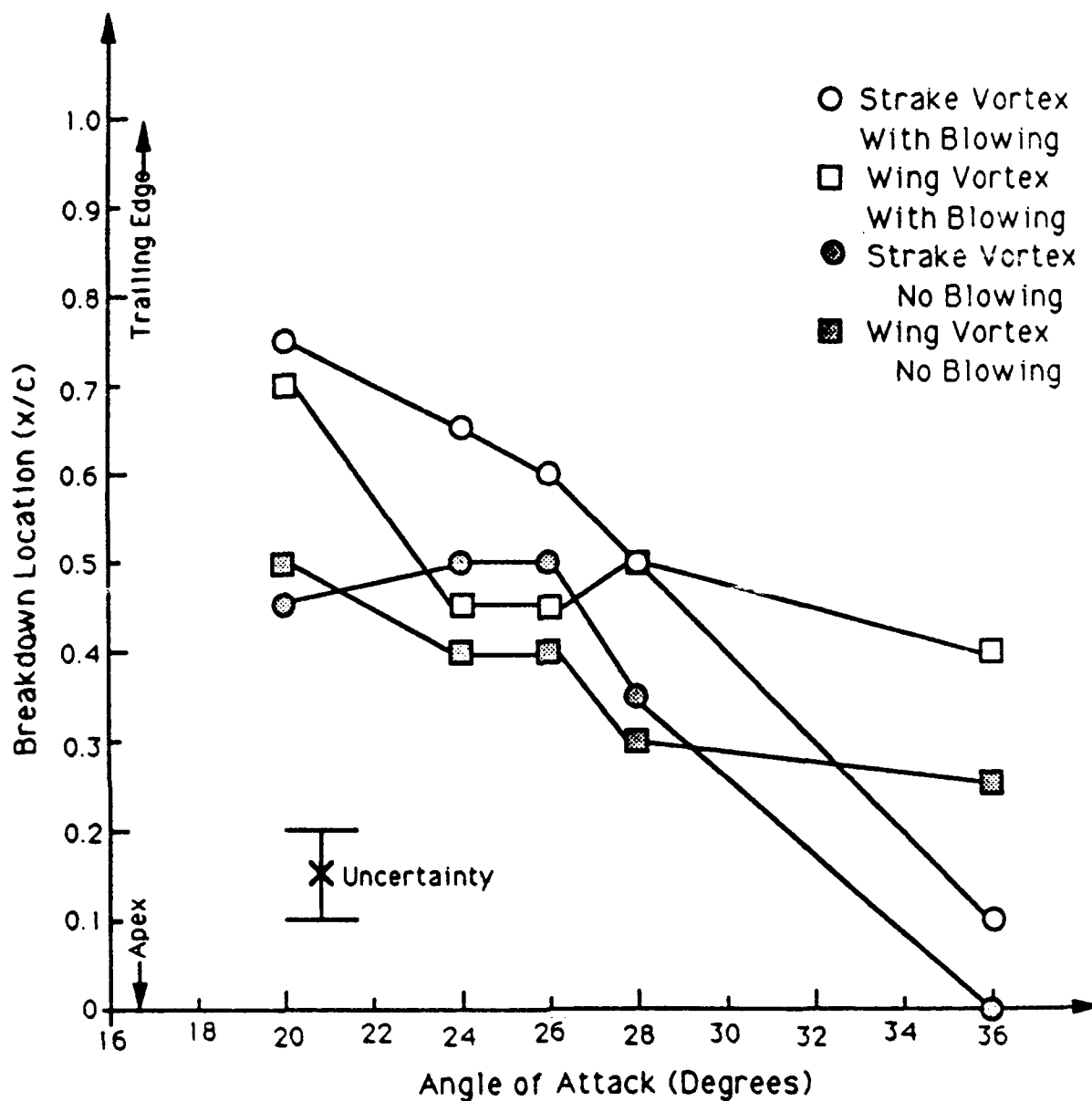
Figure 5.1.6   Vortex Breakdown Locations for Long Strakes
                Versus Angle of Attack for No Blowing and for
                Blowing Tangential to the Leading Edge at
                Blowing Port 3 with Jet on Strake Surface,
                C_μ=0.016.
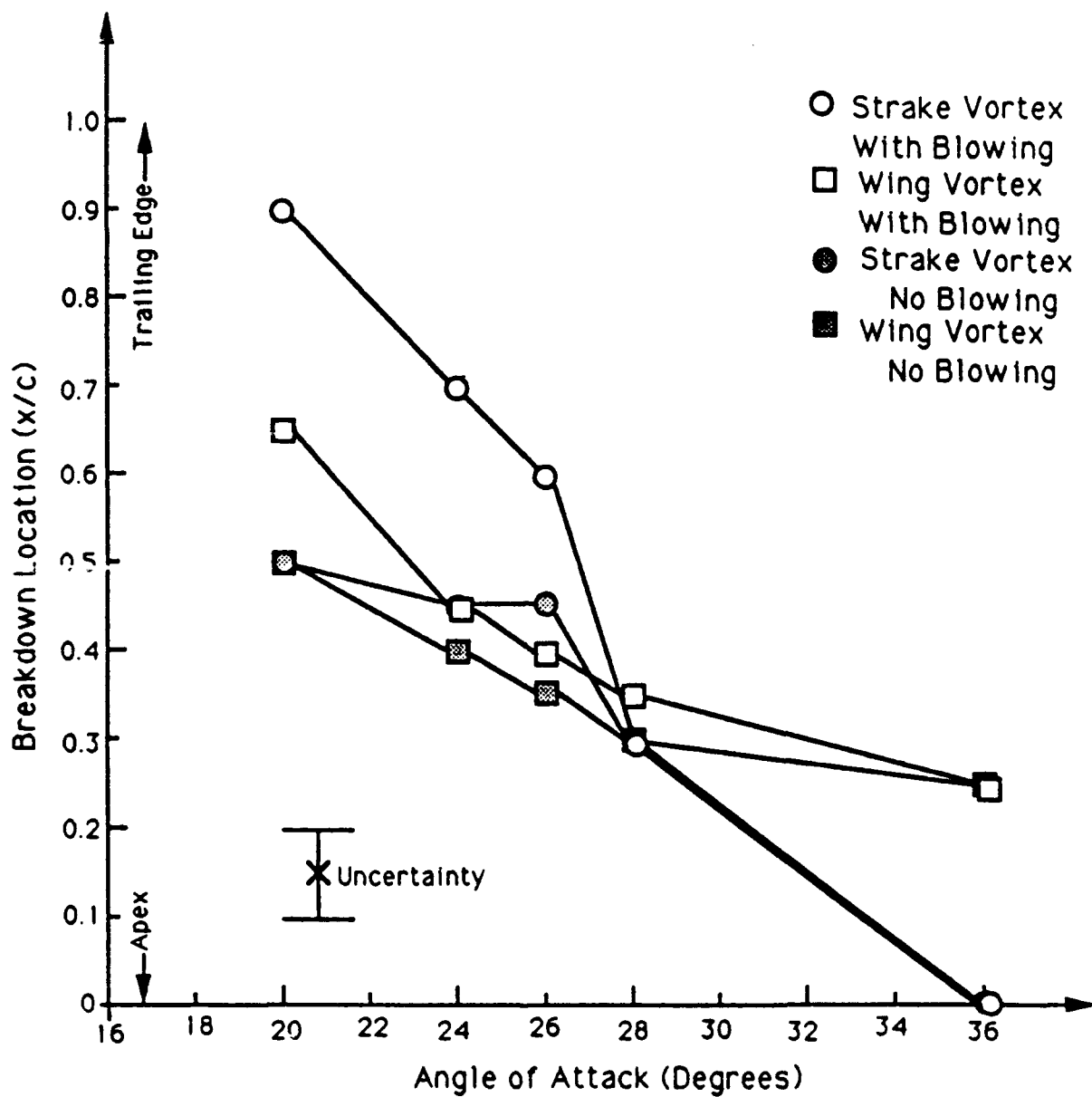
Figure 5.1.7   Vortex Breakdown Locations for Short Strakes
Versus Angle of Attack for No Blowing and for
Blowing Using 35 Degree Jet Angle at Blowing
Port 1 with Jet on Strake Surface, C_μ=0.016.
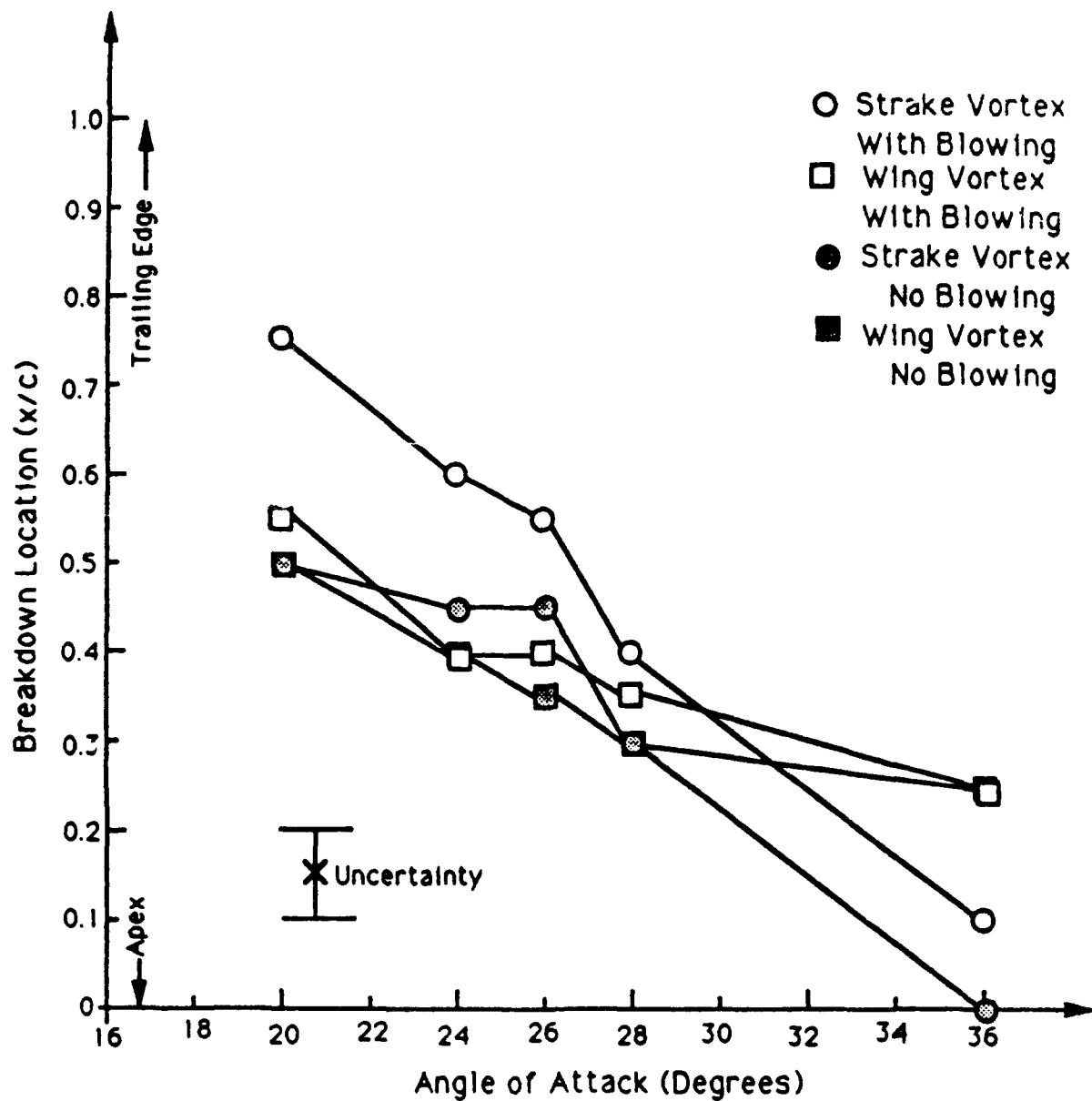
Figure 5.1.8   Vortex Breakdown Locations for Short Strakes
Versus Angle of Attack for No Blowing and for
Blowing Using 35 Degree Jet Angle at Blowing
Port 2 with Jet on Strake Surface, C_μ=0.016.
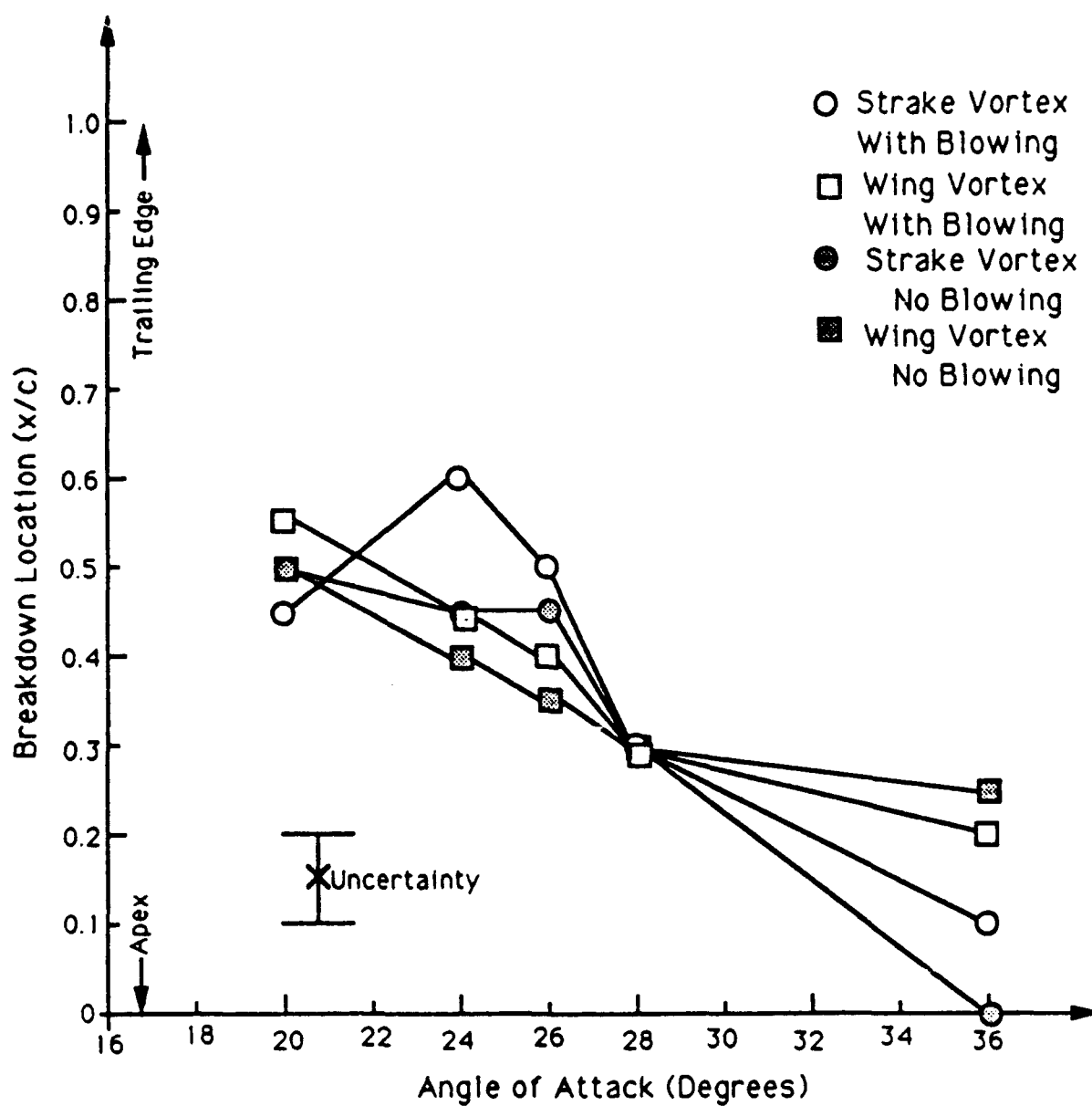
Figure 5.1.9   Vortex Breakdown Locations for Short Strakes
                Versus Angle of Attack for No Blowing and for
                Blowing Tangential to the Leading Edge at
                Blowing Port 3 with Jet Inclination Angle of 10
                Degrees, C_μ=0.016.
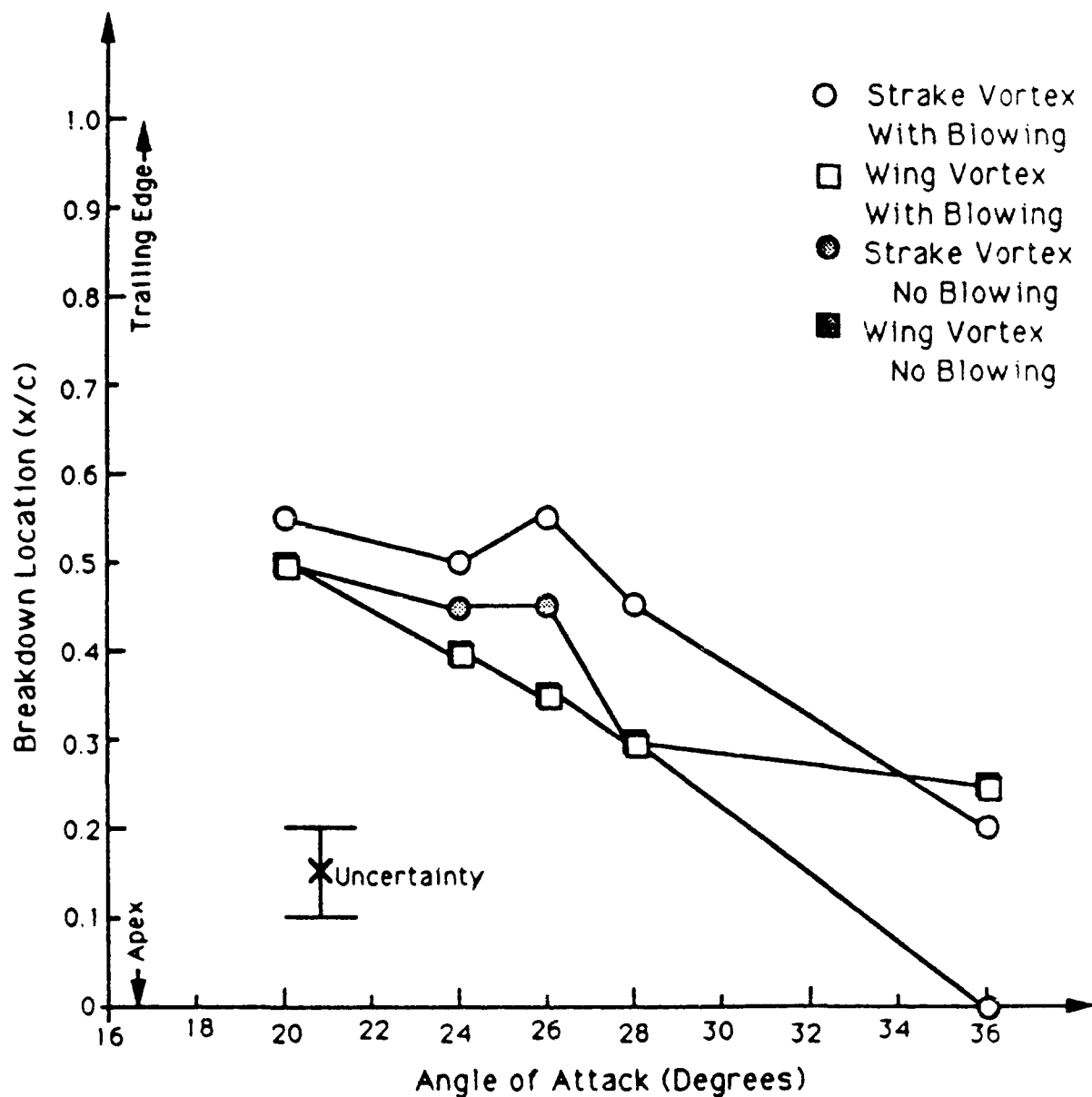
Figure 5.1.10   Vortex Breakdown Locations for Short Strakes
                 Versus Angle of Attack for No Blowing and for
                 Blowing Tangential to the Leading Edge at
                 Blowing Port 1 with Jet Inclination Angle of 0
                 Degrees, C_μ=0.016.
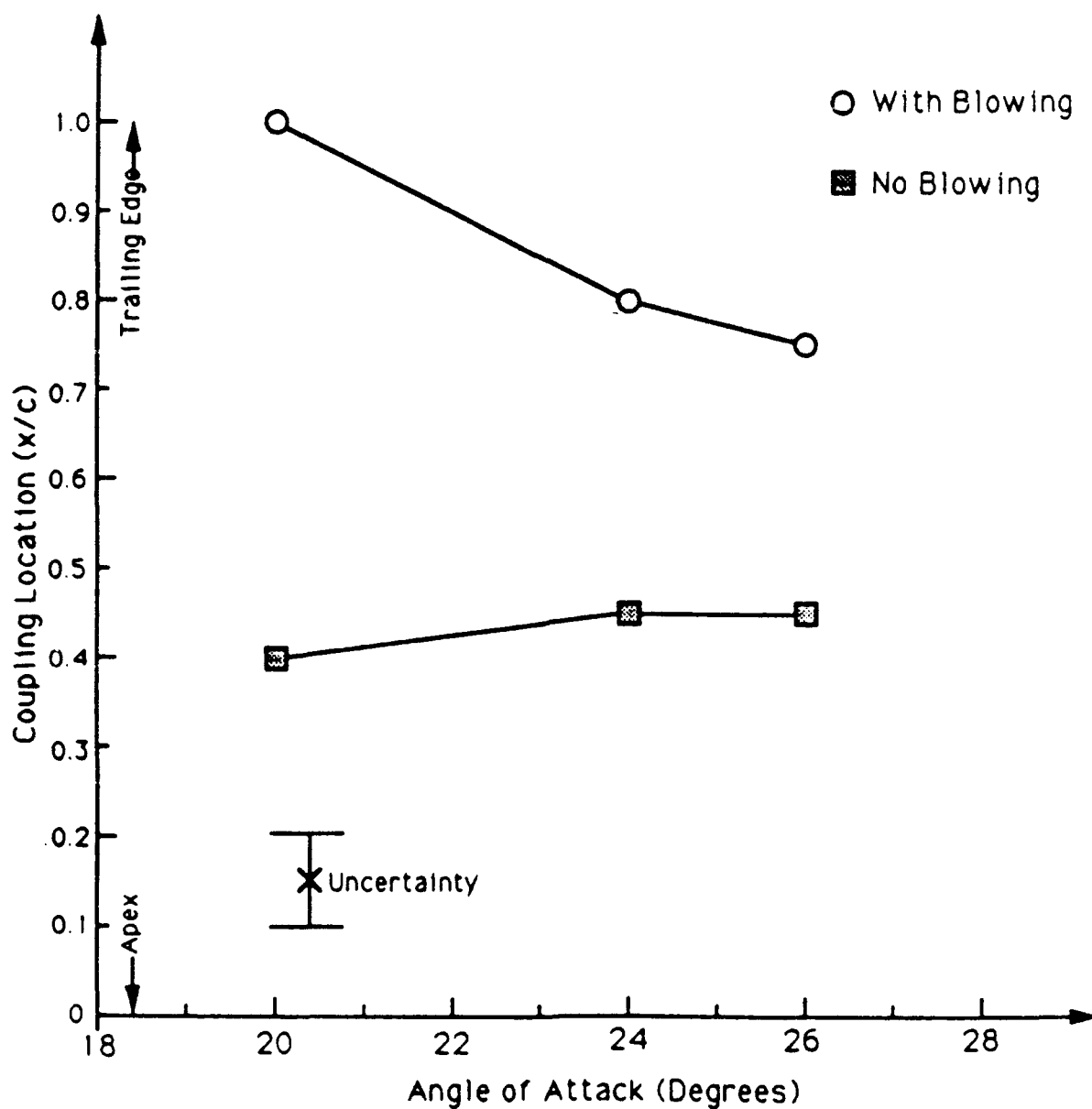
Figure 5.1.11 Vortex Coupling Locations for Long Strakes
Versus Angle of Attack for No Blowing and for
Blowing Using 35 Degree Jet Angle at Blowing
Port 1 with Jet on Strake Surface, C_μ=0.016.
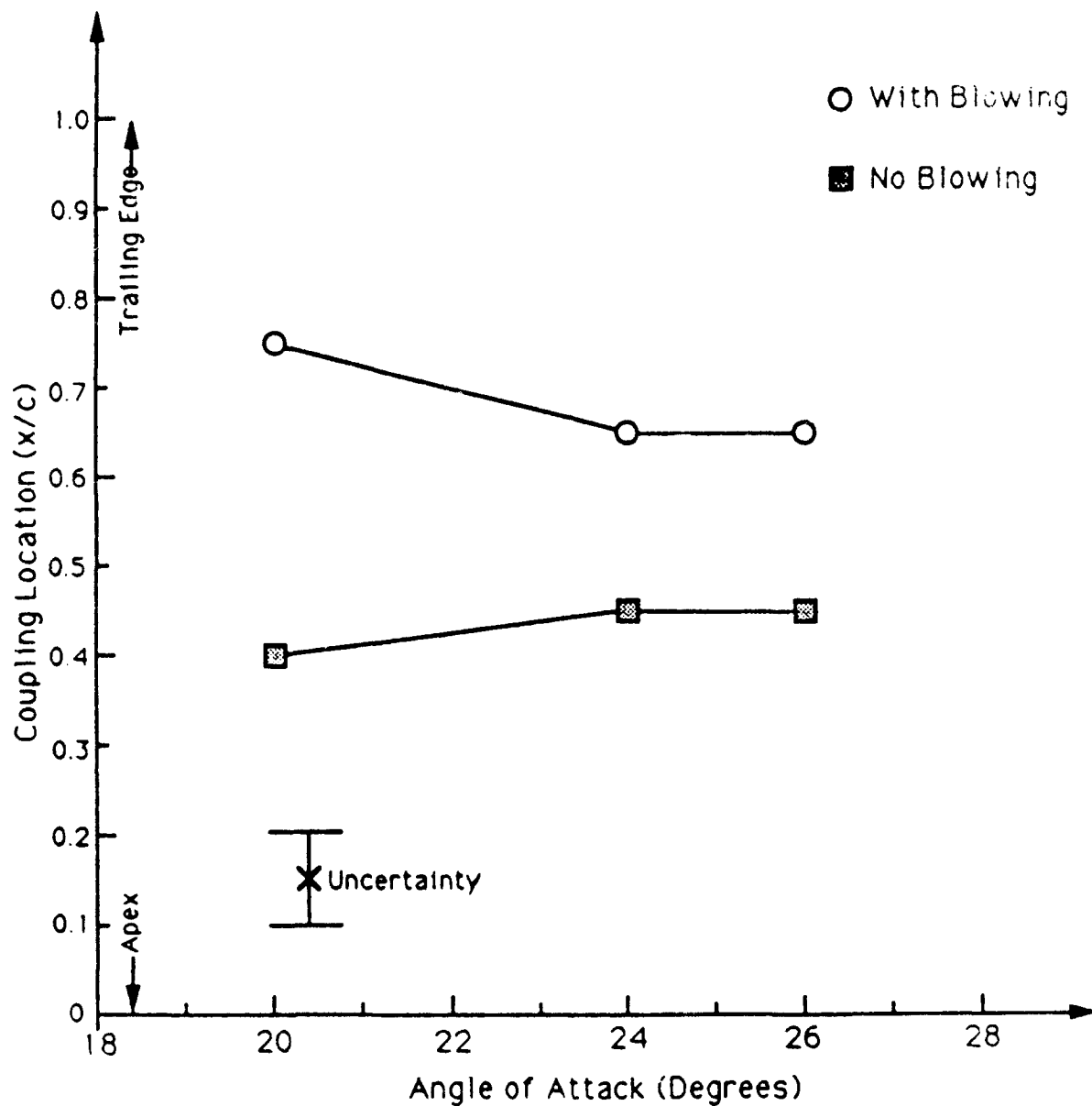
Figure 5.1.12   Vortex Coupling Locations for Long Strakes
Versus Angle of Attack for No Blowing and for
Blowing Tangential to the Leading Edge at
Blowing Port 1 with Jet Inclination Angle of 10
Degrees, C_μ=0.016.
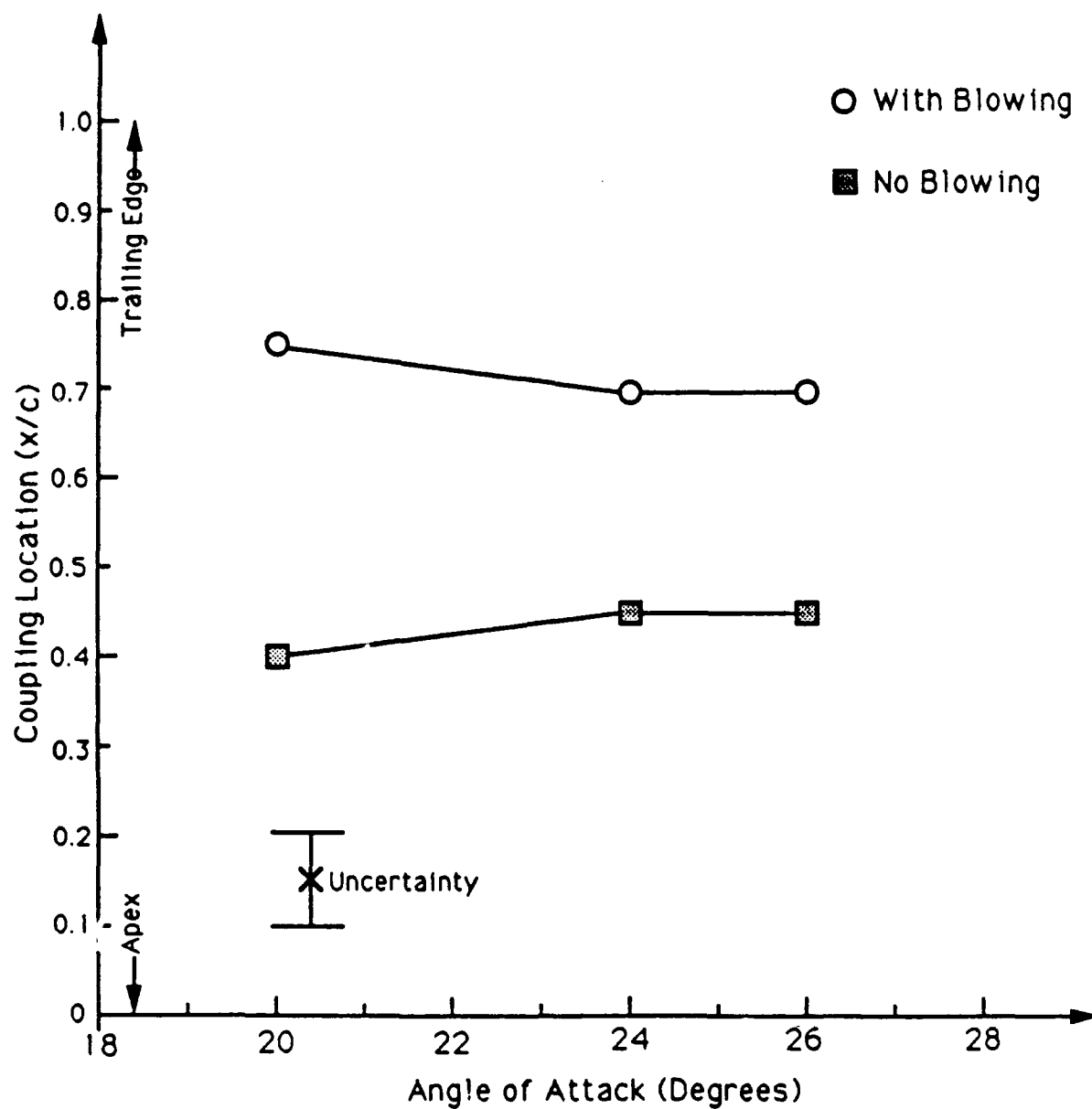
Figure 5.1.13   Vortex Coupling Locations for Long Strakes
                Versus Angle of Attack for No Blowing and for
                Blowing Using 35 Degree Jet Angle at Blowing
                Port 2 with Jet Inclination Angle of 30 Degrees,
                C_μ=0.016.
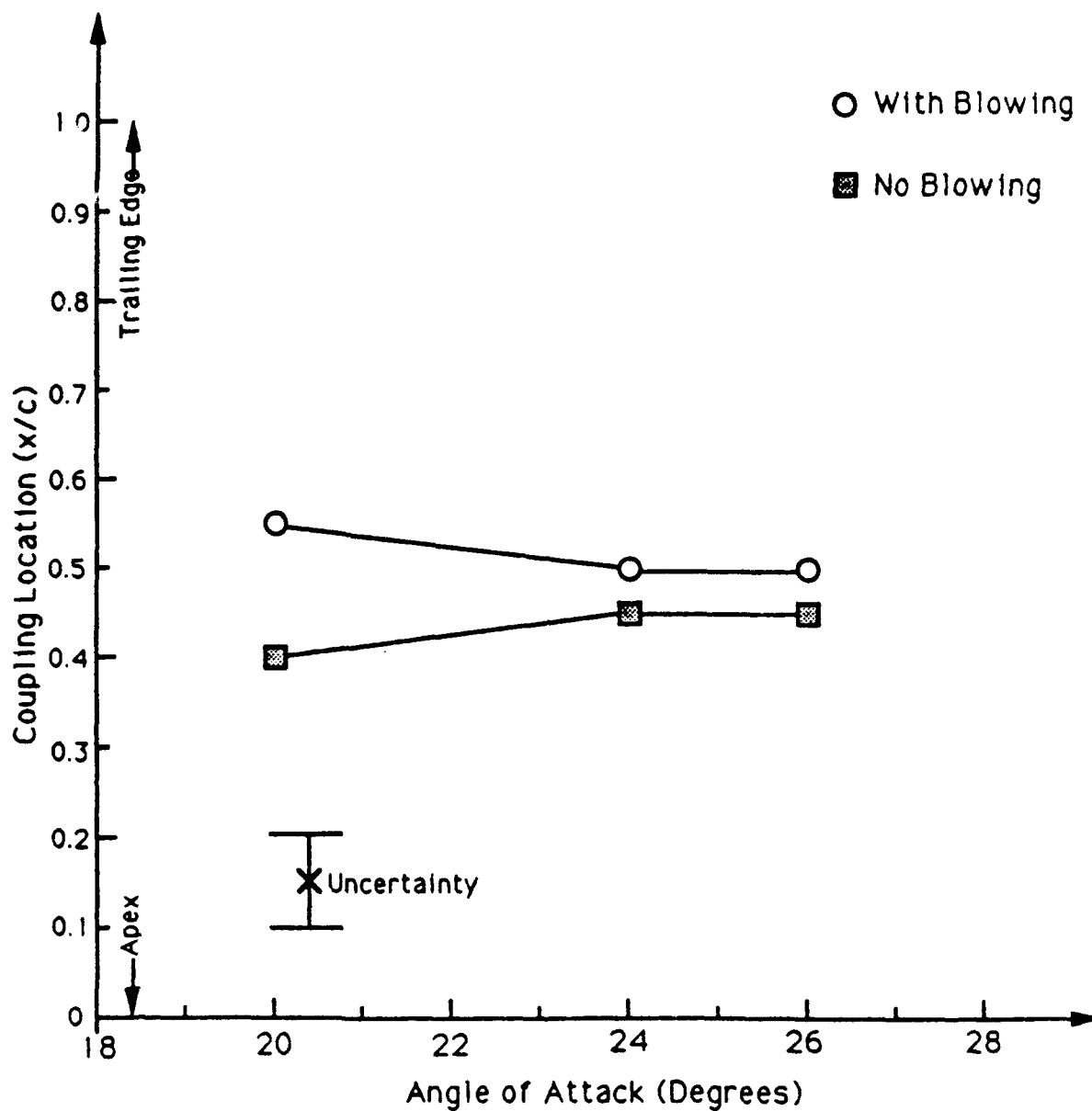
Figure 5.1.14   Vortex Coupling Locations for Long Strakes
Versus Angle of Attack for No Blowing and for
Blowing Tangential to the Leading Edge at
Blowing Port 3 with Jet on Strake Surface,
$C_\mu = 0.016$.
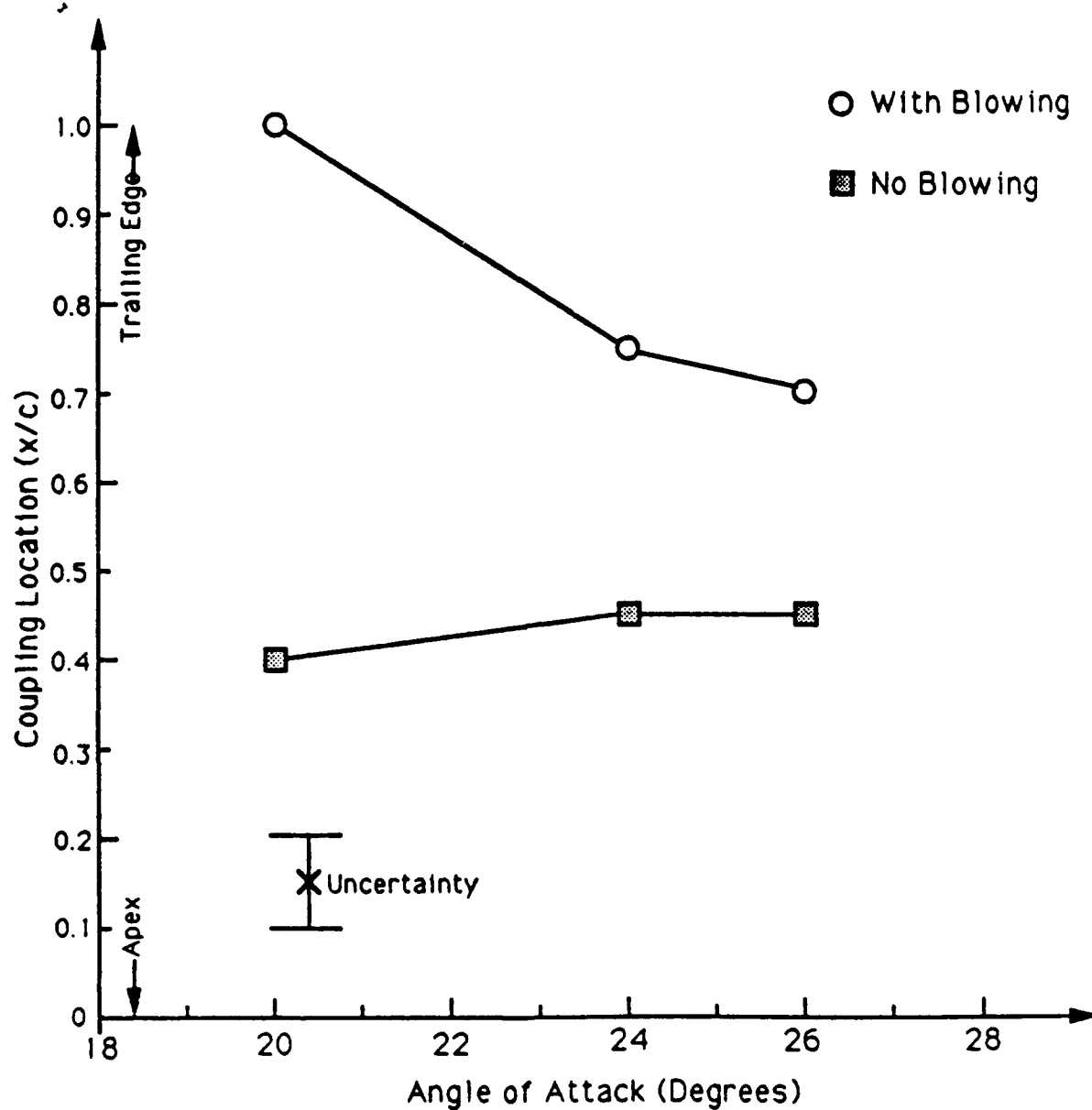
Figure 5.1.15   Vortex Coupling Locations for Short Strakes
Versus Angle of Attack for No Blowing and for
Blowing Using 35 Degree Jet Angle at Blowing
Port 1 with Jet on Strake Surface, $C_\mu = 0.016$.
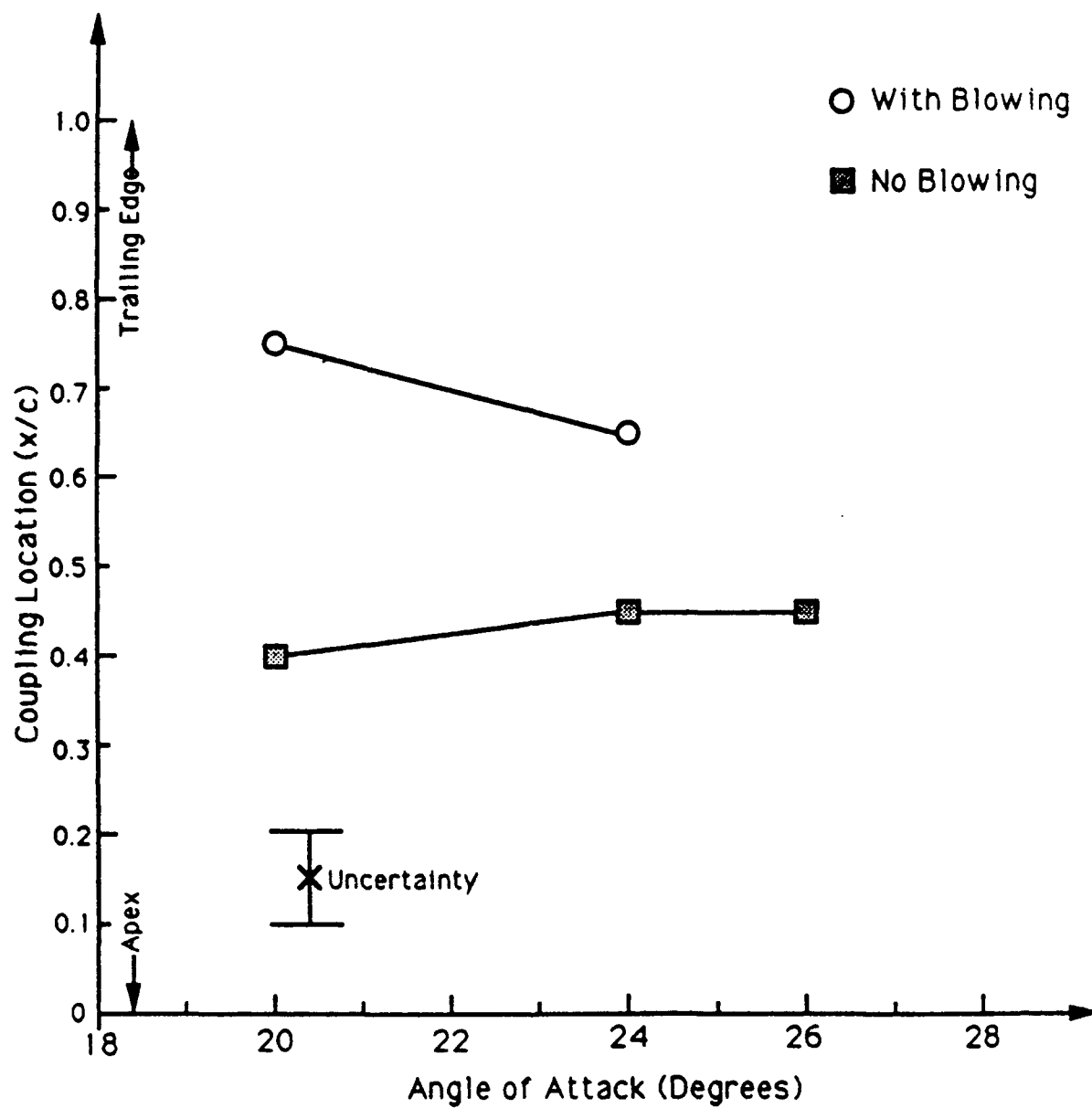
Figure 5.1.16 Vortex Coupling Locations for Short Strakes Versus Angle of Attack for No Blowing and for Blowing Using 35 Degree Jet Angle at Blowing Port 2 with Jet on Strake Surface, $C_\mu = 0.016$.

112
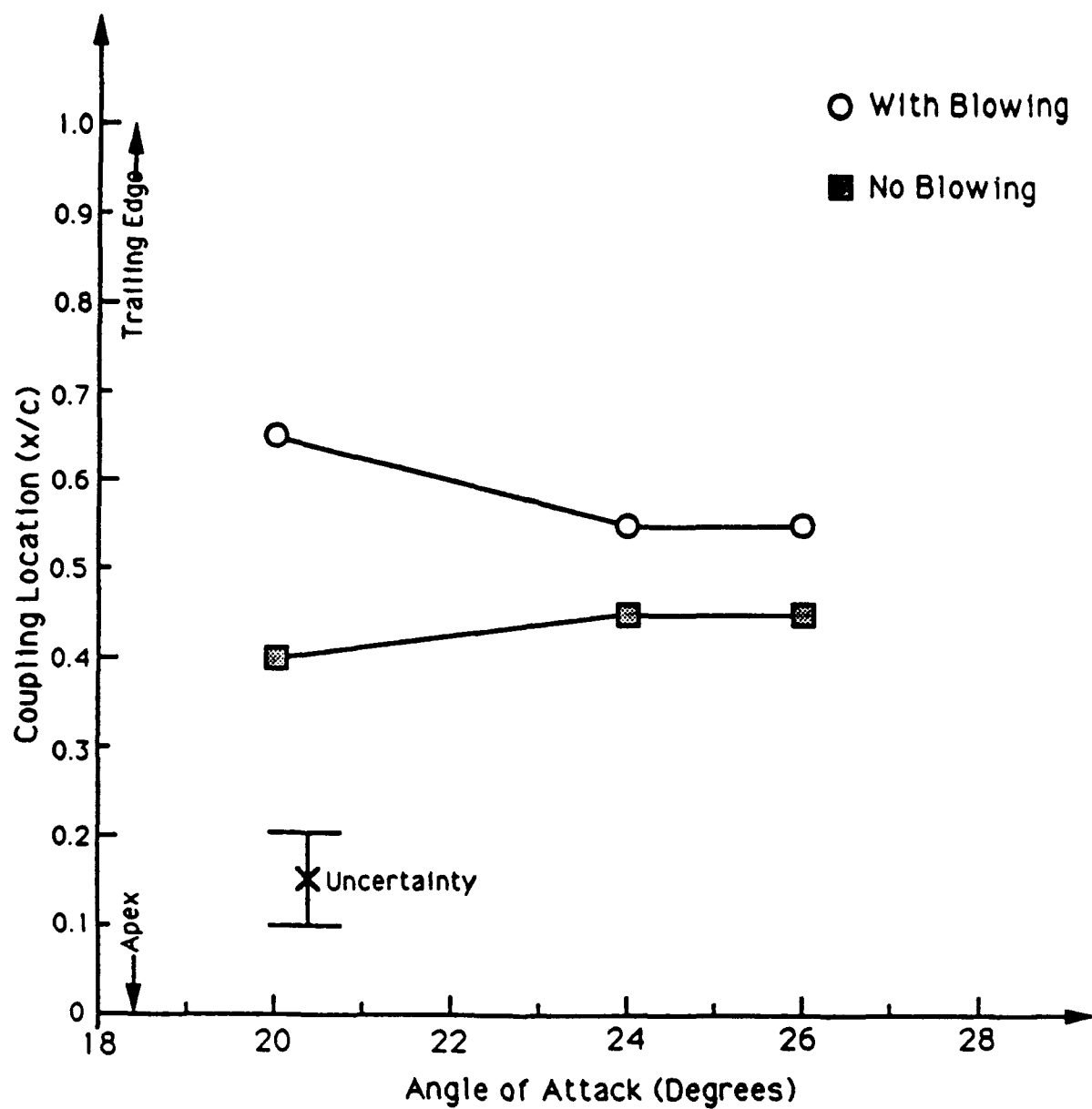
Figure 5.1.17   Vortex Coupling Locations for Short Strakes
Versus Angle of Attack for No Blowing and for
Blowing Tangential to the Leading Edge at
Blowing Port 3 with Jet Inclination Angle of 10
Degrees, C_{μ}=0.016.
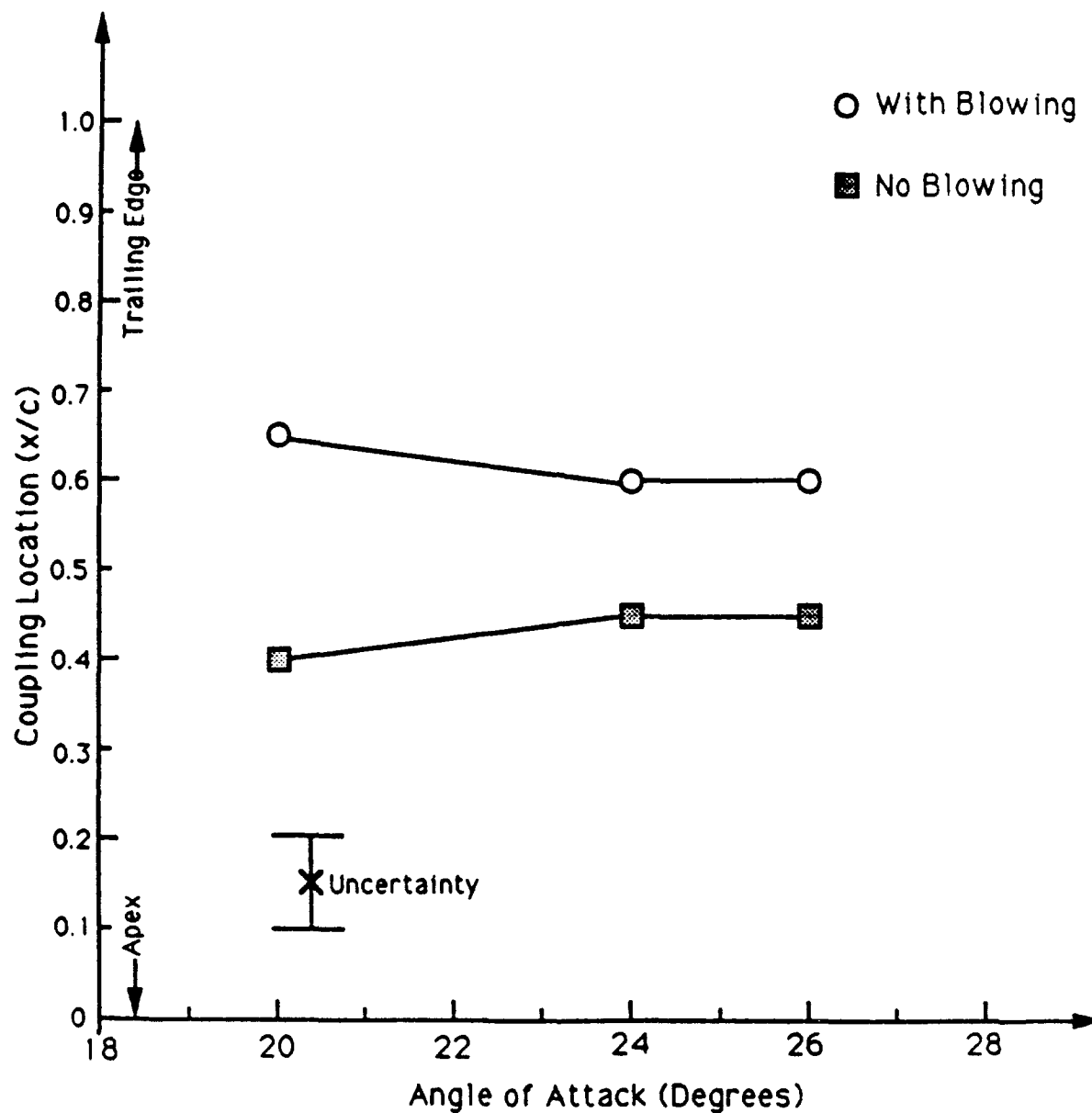
Figure 5.1.18   Vortex Coupling Locations for Short Strakes
Versus Angle of Attack for No Blowing and for
Blowing Tangential to the Leading Edge at
Blowing Port 1 with Jet Inclination Angle of 0
Degrees, $C_\mu = 0.016$.

Laser Light Sheet
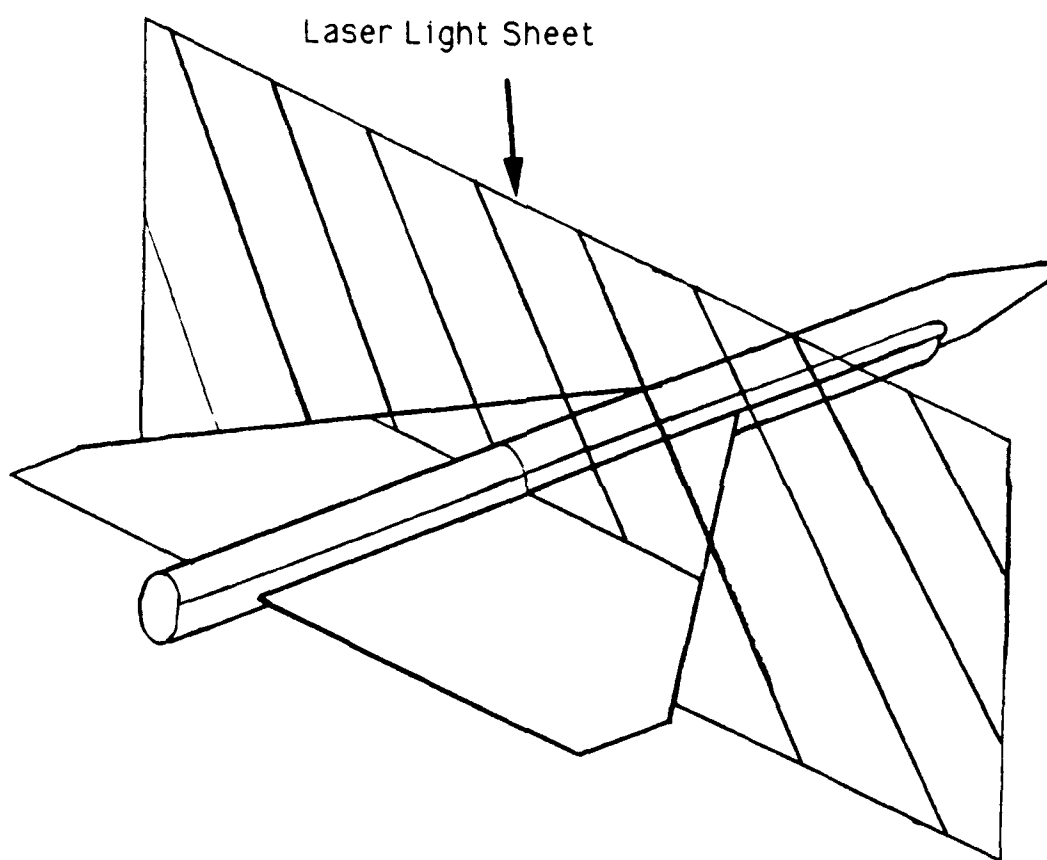
Figure 5.1.19   Schematic Showing Model Orientation for
Photographs

115
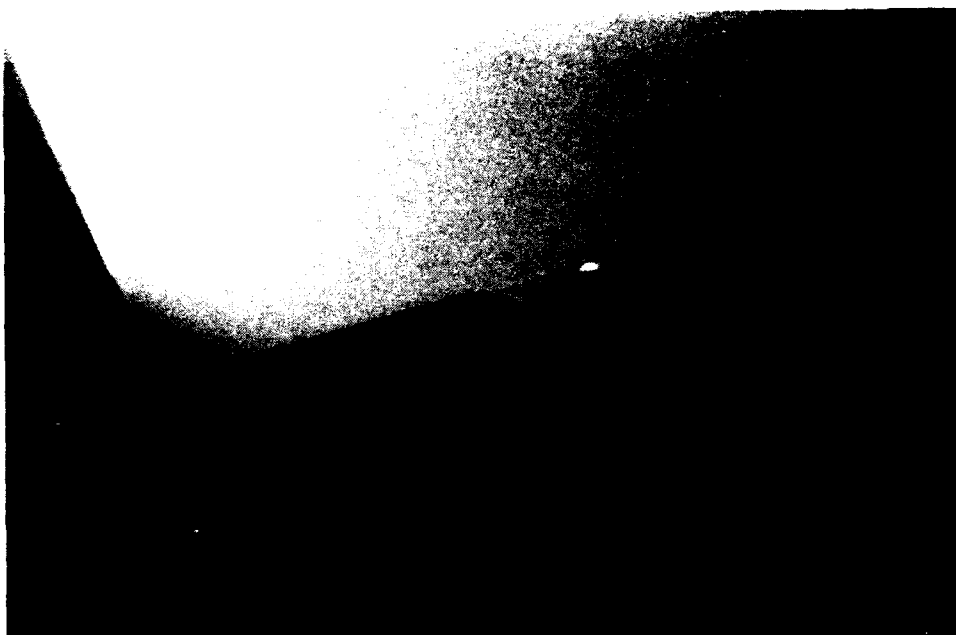
a) blowing off, X/C=0.4

b) blowing on, X/C=0.4

Figure 5.1.20   Photographs at X/C Locations of 0.4, 0.55, and
0.75 Showing Effect of Blowing at Model Angle of
Attack of 20 Degrees Using Long Strakes and 35
Degree Jet Angle at Blowing Port 1 with Jet on
Strake Surface, C_μ=0.016.

116

c) blowing off, X/C=0.55

d) blowing on, X/C=0.55

Figure 5.1.20 Continued

117
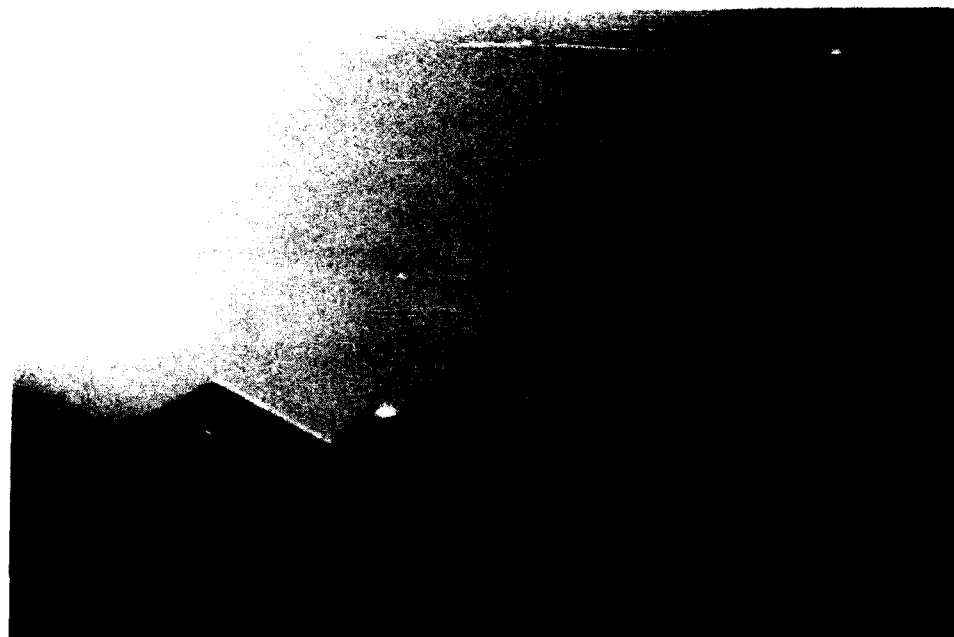
e) blowing off, X/C=0.75

f) blowing on, X/C=0.75

Figure 5.1.20   Concluded.

a) blowing off, X/C=0.35

b) blowing on, X/C=0.35

Figure 5.1.21 Photographs at X/C Locations of 0.35, 0.5, and 0.7 Showing Effect of Blowing at Model Angle of Attack of 20 Degrees Using Long Strakes and Blowing Tangential to the Leading Edge at Blowing Port 1 with Jet Inclination Angle of 10 Degrees, C_μ=0.016.

c)   blowing off, X/C=0.5

d)   blowing on, X/C=0.5

Figure 5.1.21   Continued

e) blowing off, X/C=0.7

f) blowing on, X/C=0.7

Figure 5.1.21   Concluded.

a) blowing off, X/C=0.35

b) blowing on, X/C=0.35

Figure 5.1.22 Photographs at X/C Locations of 0.35 and 0.5 Showing Effect of Blowing at Model Angle of Attack of 24 Degrees Using Long Strakes and 35 Degree Jet Angle at Blowing Port 1 with Jet on Strake Surface, C_μ=0.016.
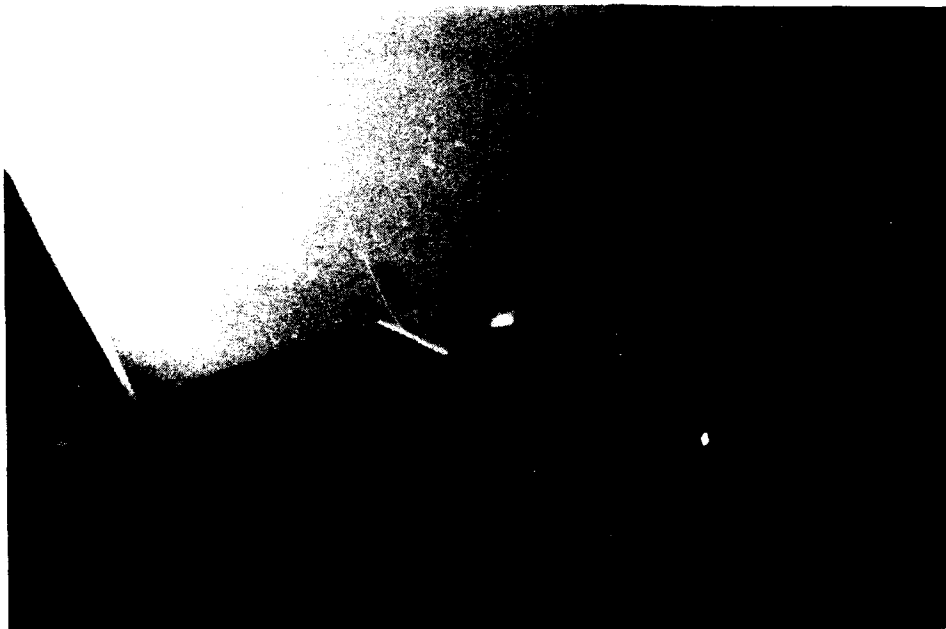
c) blowing off, X/C=0.5

d) blowing on, X/C=0.5

Figure 5.1.22   Concluded.
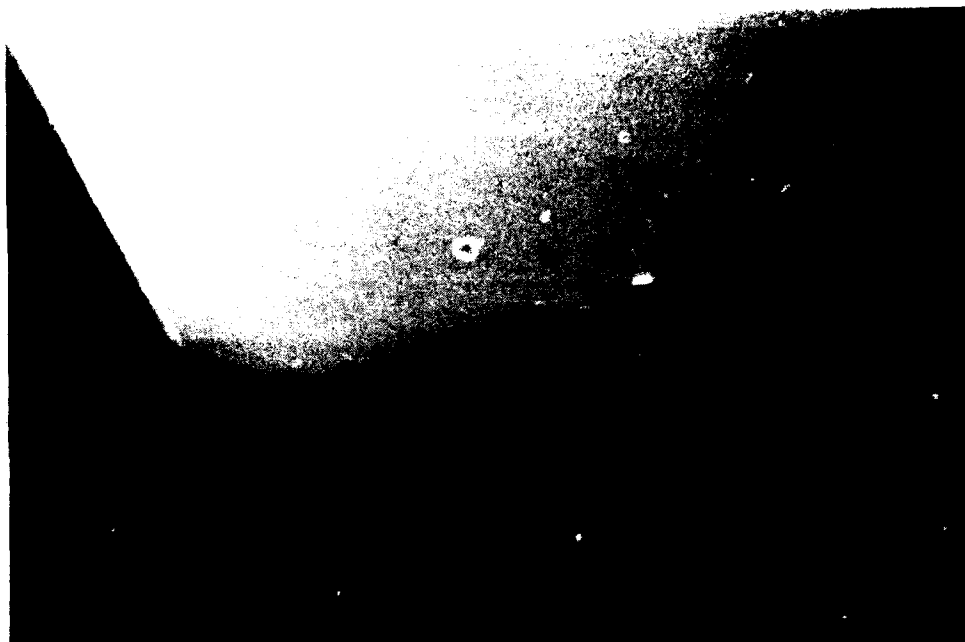
a) blowing off, X/C=0.35

b) blowing on, X/C=0.35

Figure ˉ.1.23   Photographs at X/C Locations of 0.35 and 0.5
Showing Effect of Blowing at Model Angle of
Attack of 24 Degrees Using Long Strakes and
Blowing Tangential to Leading Edge at Blowing
Port 1 with Jet Inclination Angle of 10 Degrees,
C_μ=0.016.

124
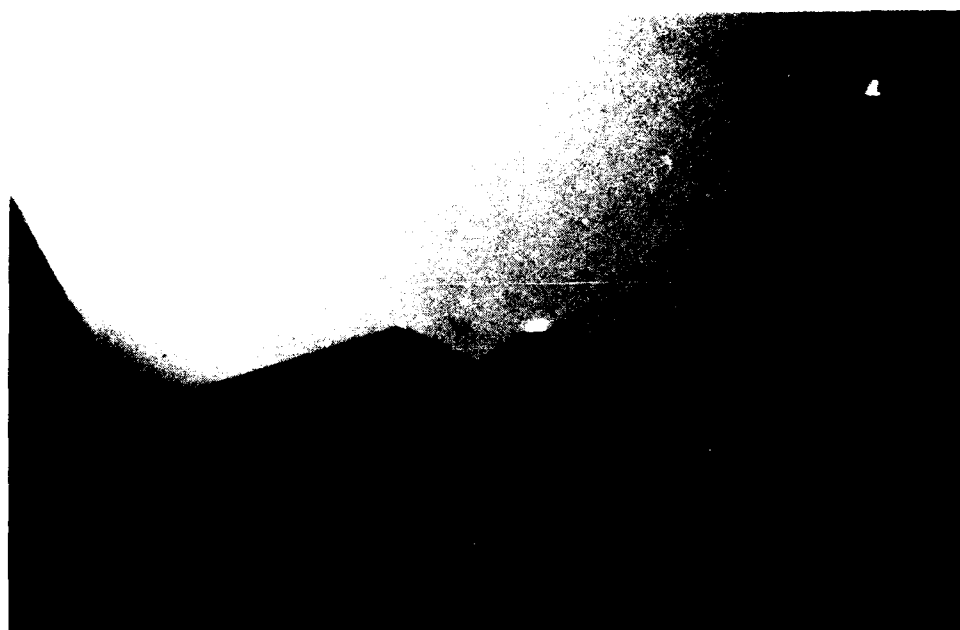
c) blowing off, X/C=0.5

d) blowing on, X/C=0.5

Figure 5.1.23 Concluded.
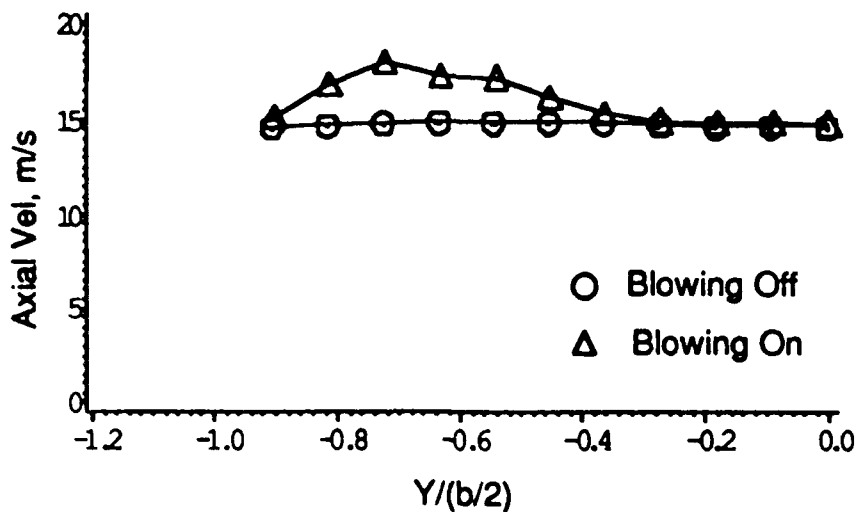
a) mean axial velocity versus spanwise locations, z/(b/2)=1.15
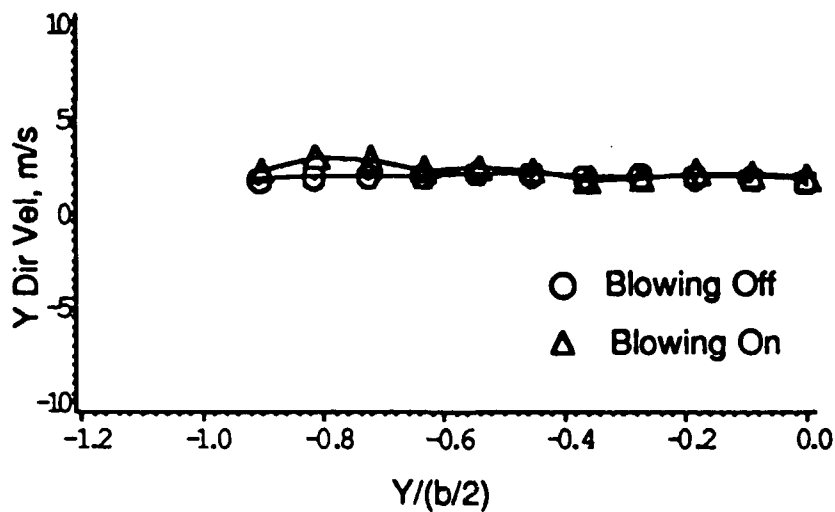
b) mean spanwise velocity versus spanwise locations, z/(b/2)=1.15

Figure 5.2.1   Mean Velocities, RMS Velocities, and Cross Correlations for No Blowing and for Blowing On with C_μ=0.016 as a Function of the Spanwise Locations at z/(b/2)=1.15.
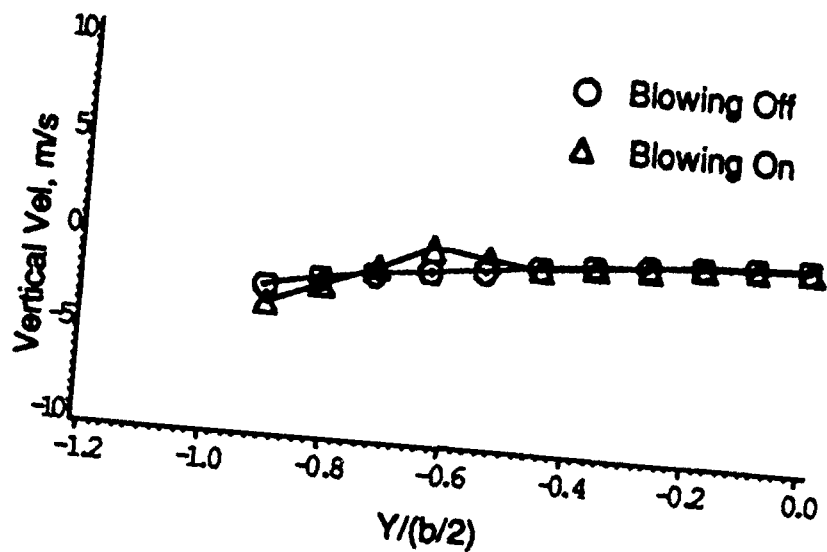
c) mean vertical velocity versus spanwise locations, z/(b/2)=1.15
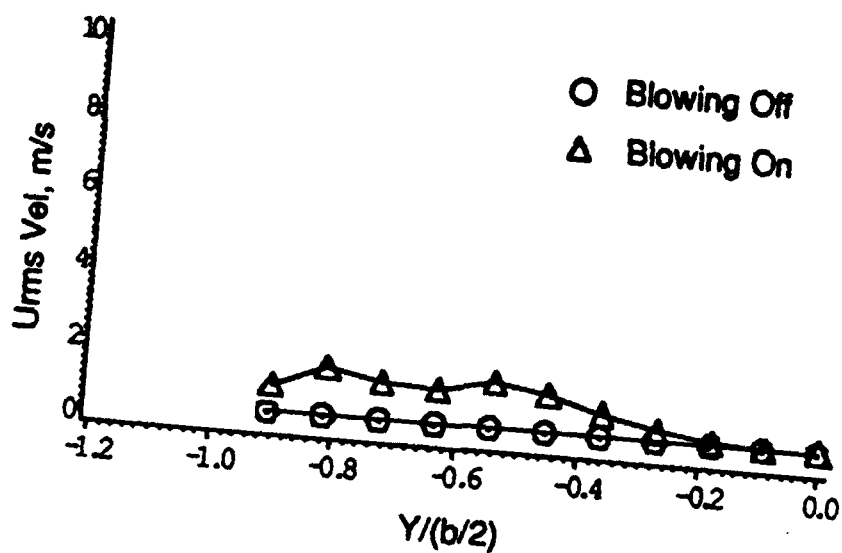
d) axial RMS velocity versus spanwise locations, z/(b/2)=1.15

Figure 5.2.1   Continued

127
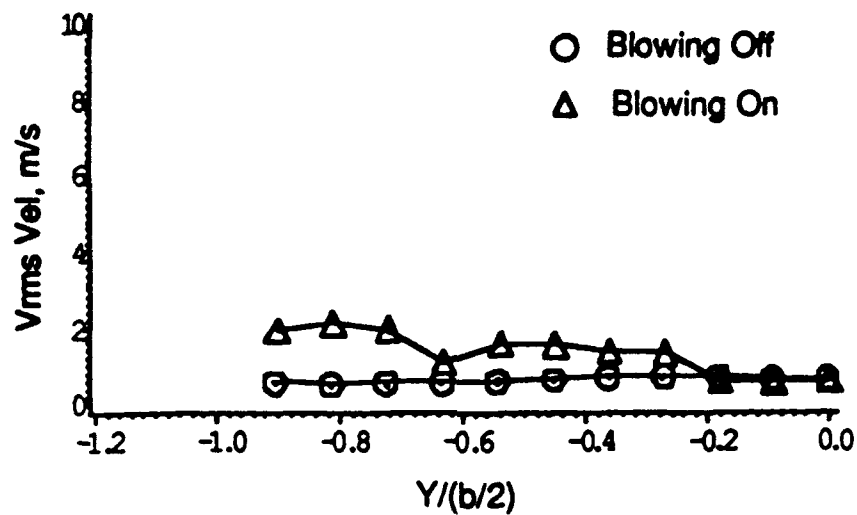
e) spanwise RMS velocity versus spanwise locations, z/(b/2)=1.15

f) vertical RMS velocity versus spanwise locations, z/(b/2)=1.15
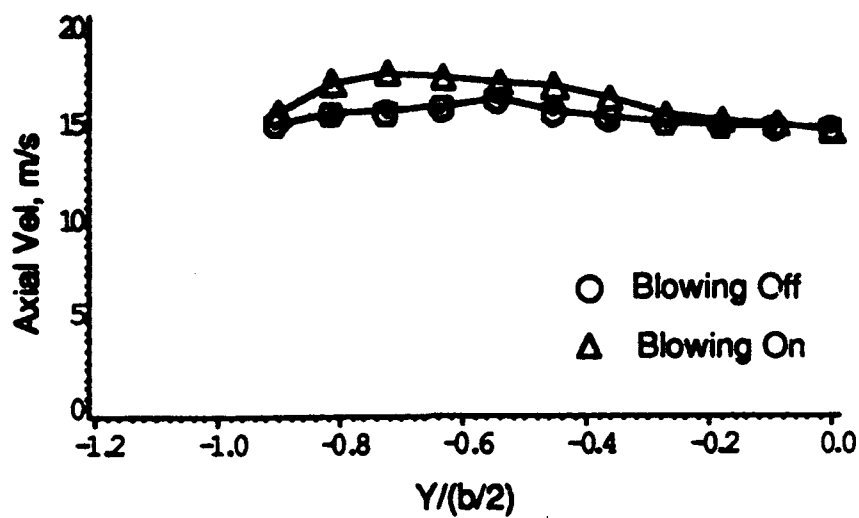
Figure 5.2.1   Continued

128
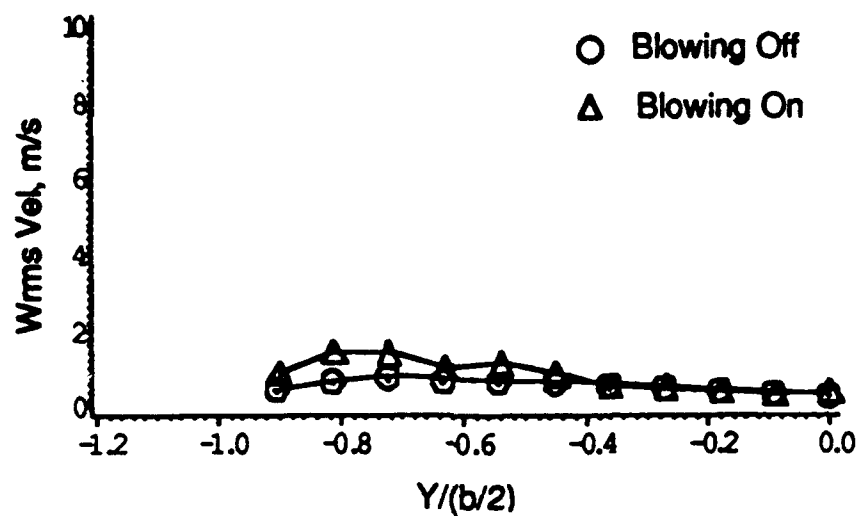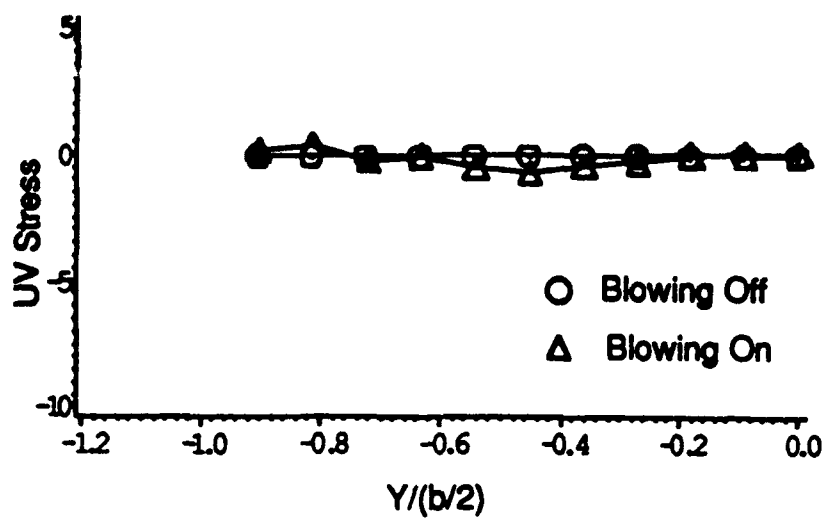
g) uv Reynolds stress versus spanwise locations, z/(b/2)=1.15

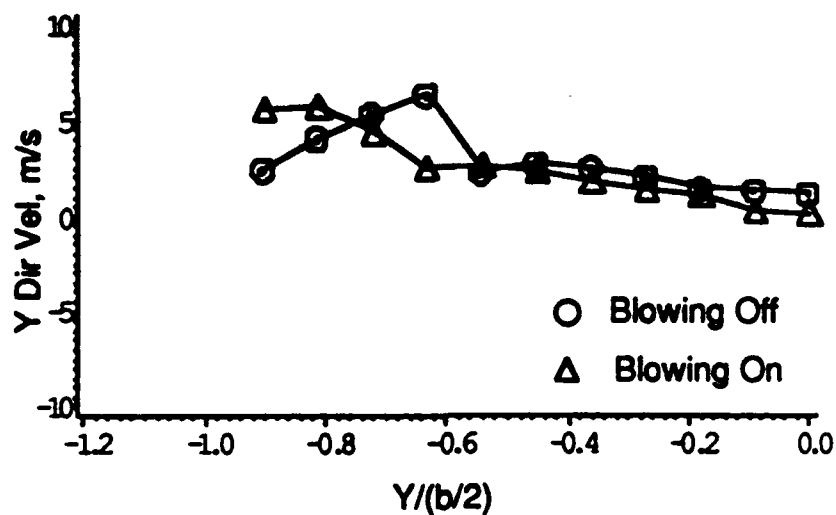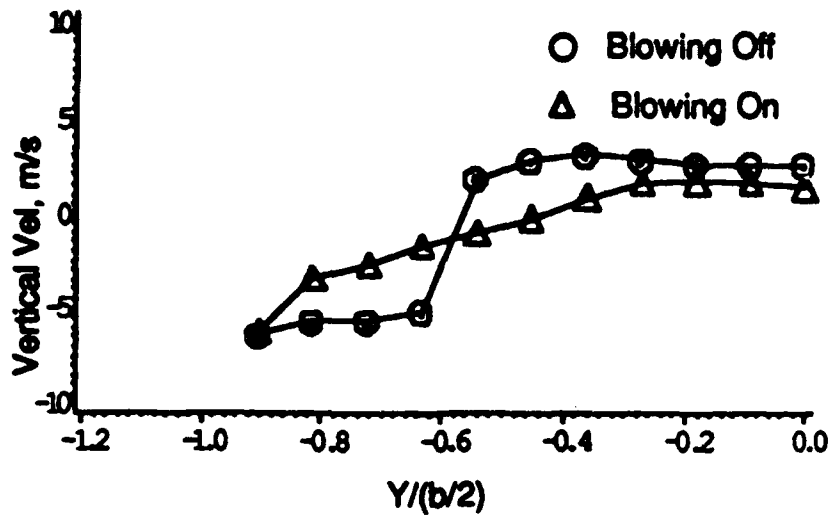h) uw Reynolds stress versus spanwise locations, z/(b/2)=1.15

Figure 5.2.1   Continued

129
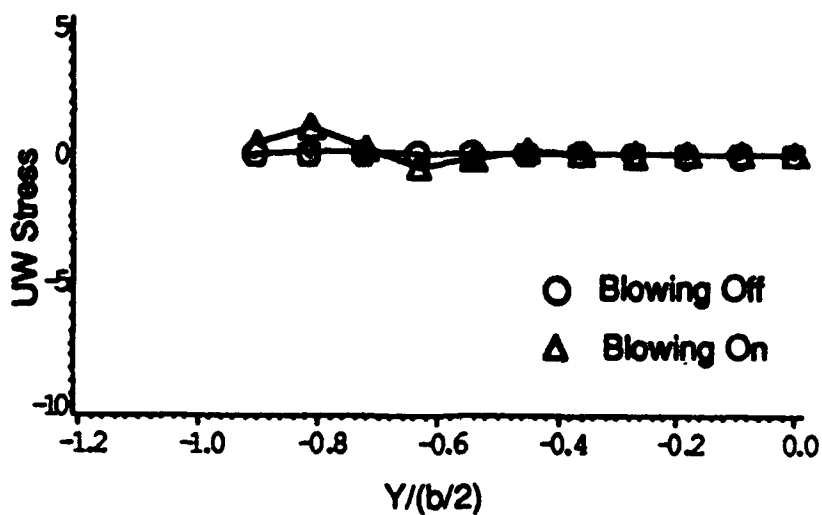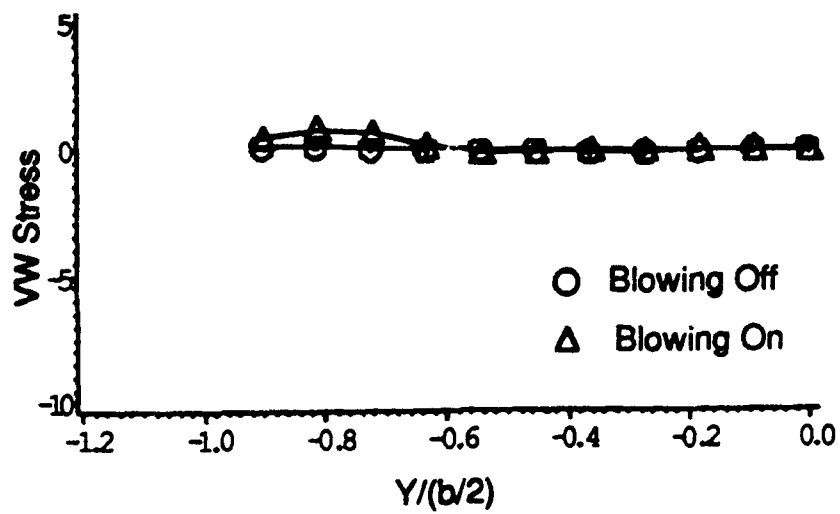
i) vw Reynolds stress versus spanwise locations, z/(b/2)=1.15

Figure 5.2.1   Concluded.

130
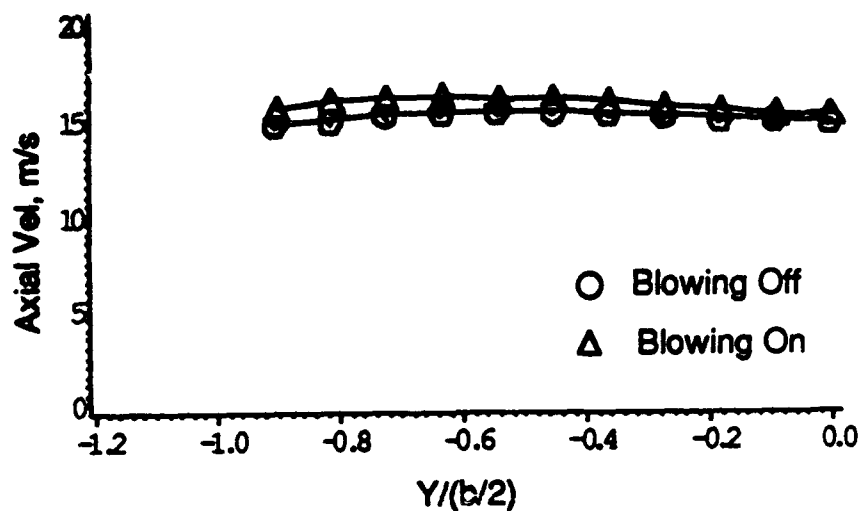
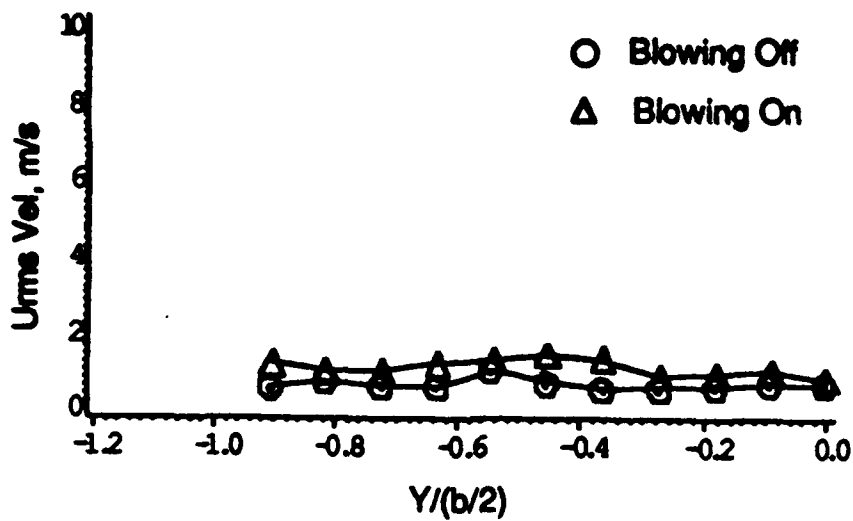a) **mean axial velocity versus spanwise locations, z/(b/2)=0.86**
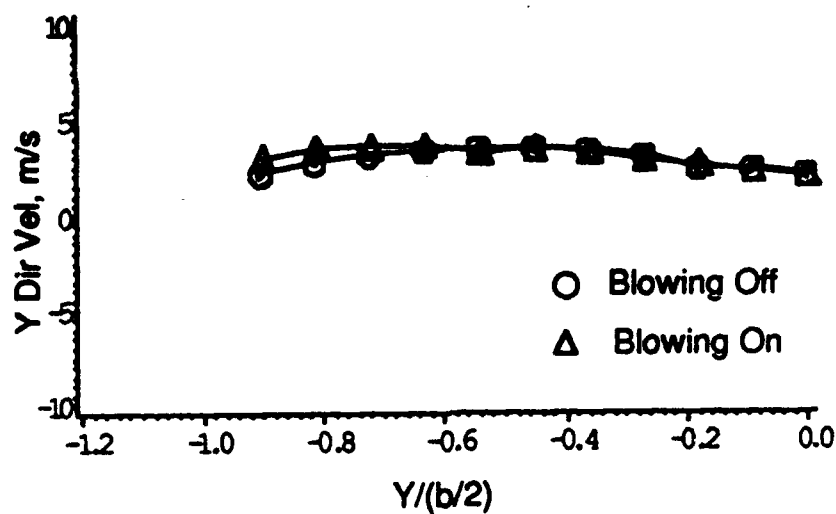
b) **mean spanwise velocity versus spanwise locations, z/(b/2)=0.86**

Figure 5.2.2   Mean Velocities, RMS Velocities, and Cross Correlations for No Blowing and for Blowing On with C_μ=0.016 as a Function of the Spanwise Locations at z/(b/2)=0.86.
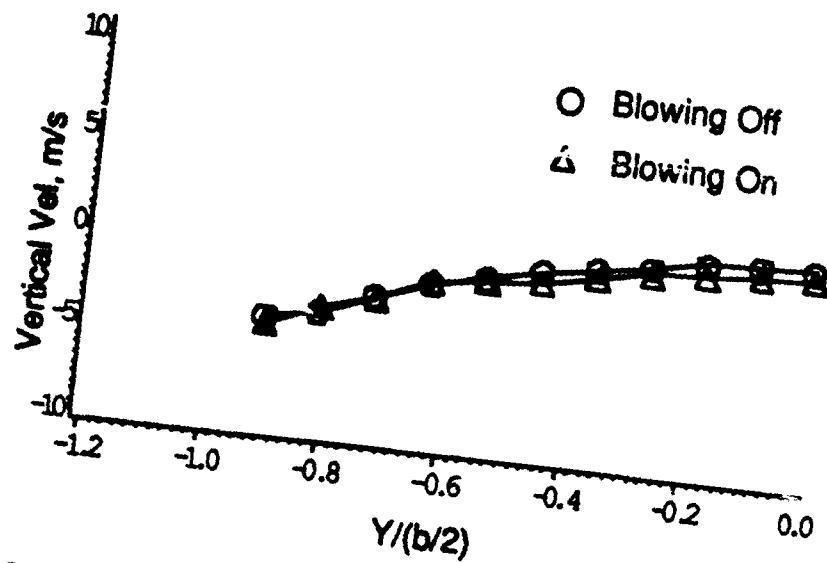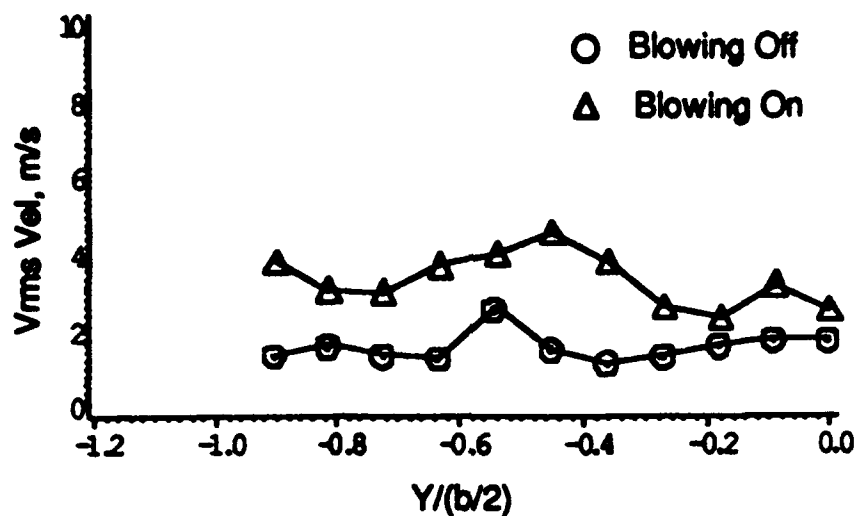
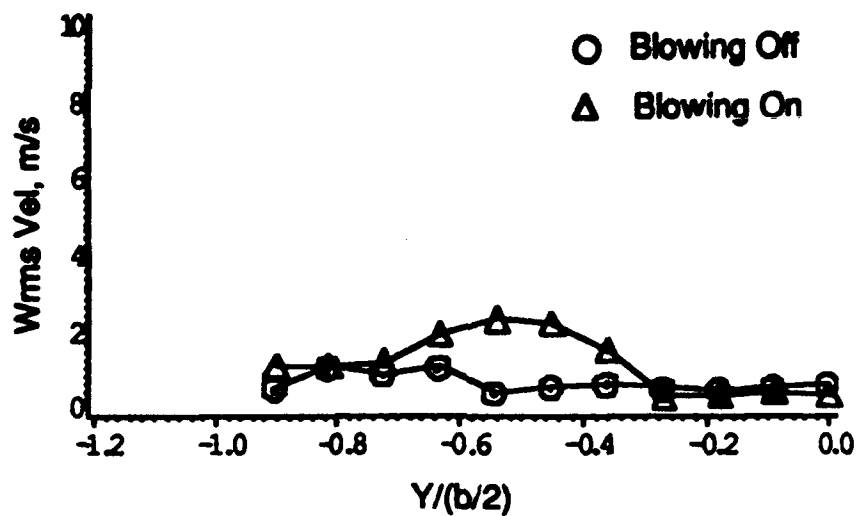c) mean vertical velocity versus spanwise locations, z/(b/2)=0.86
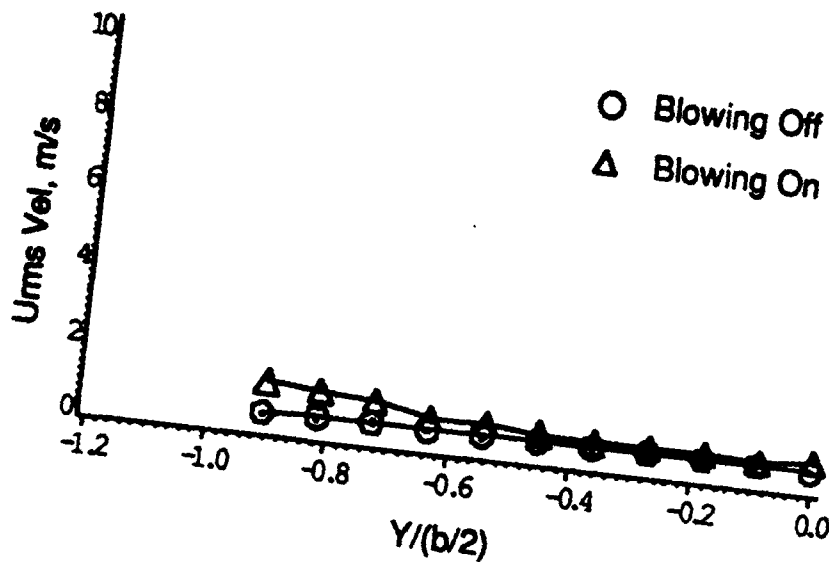
d) axial RMS velocity versus spanwise locations, z/(b/2)=0.86

Figure 5.2.2   Continued
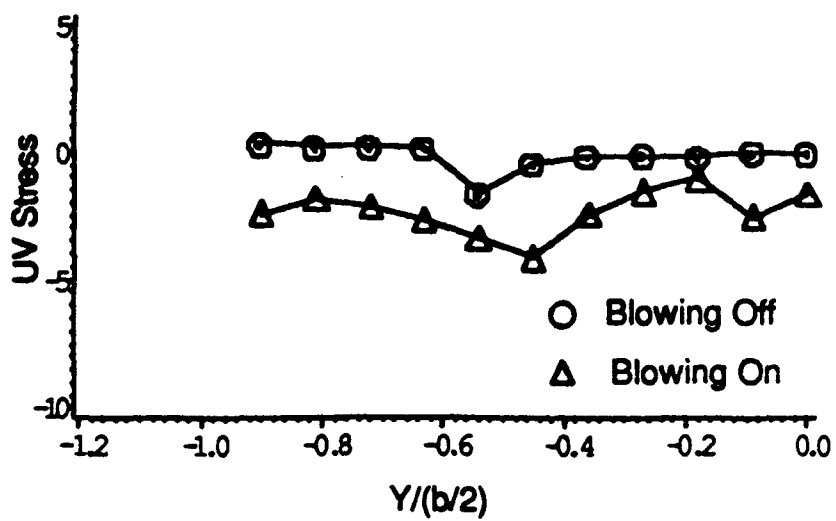
132
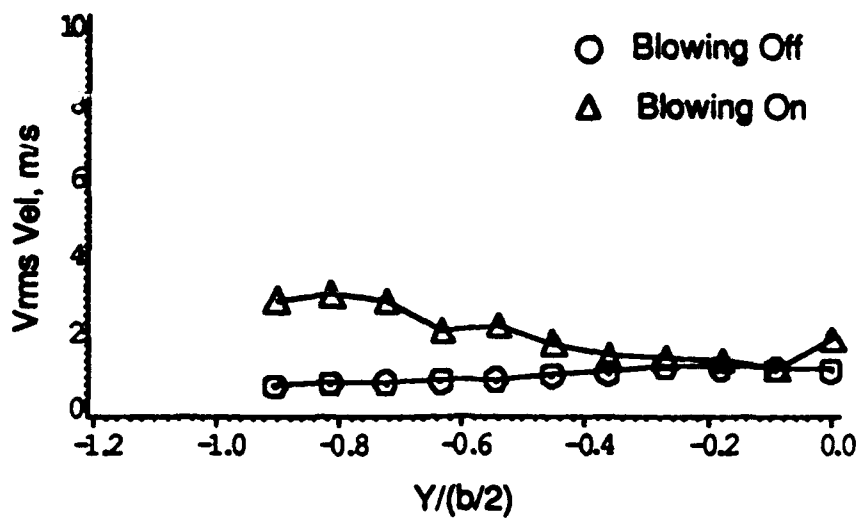
e) spanwise RMS velocity versus spanwise locations, z/(b/2)=0.86

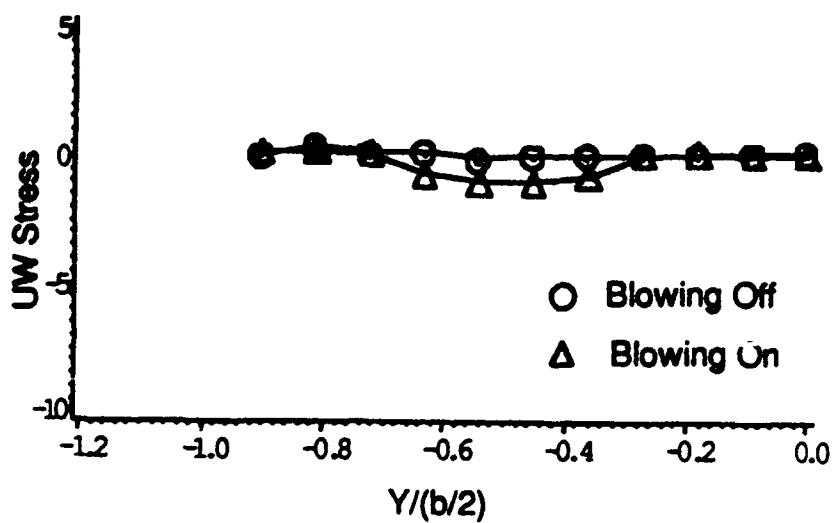
f) vertical RMS velocity versus spanwise locations, z/(b/2)=0.86

Figure 5.2.2   Continued

133
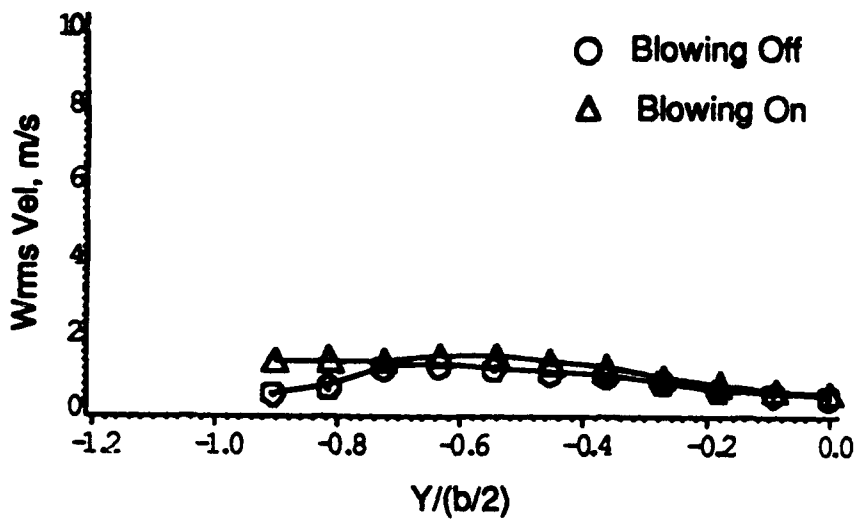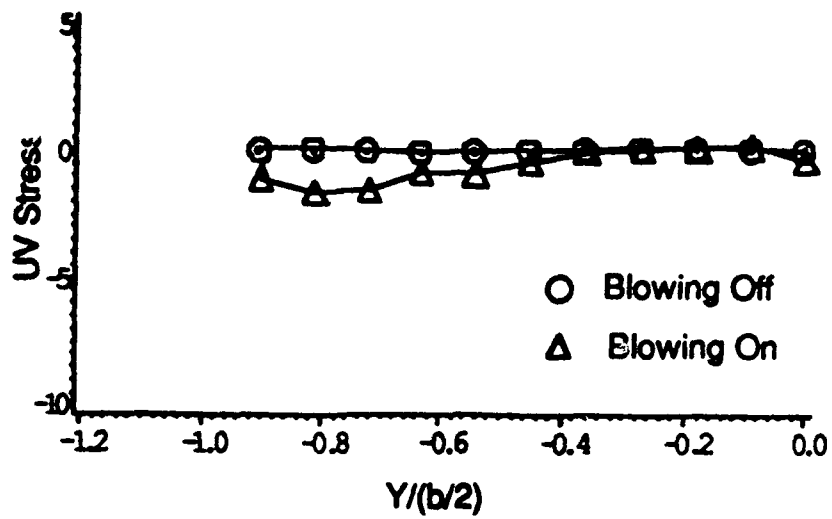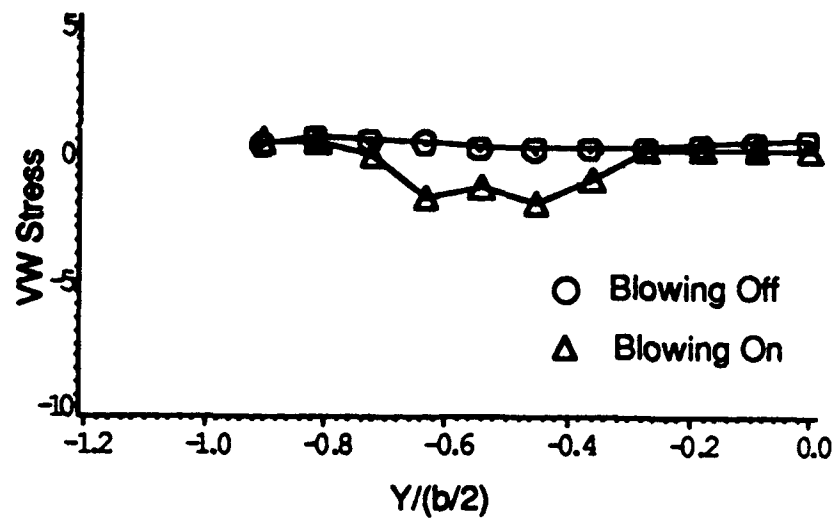
g) uv Reynolds stress versus spanwise locations, z/(b/2)=0.86
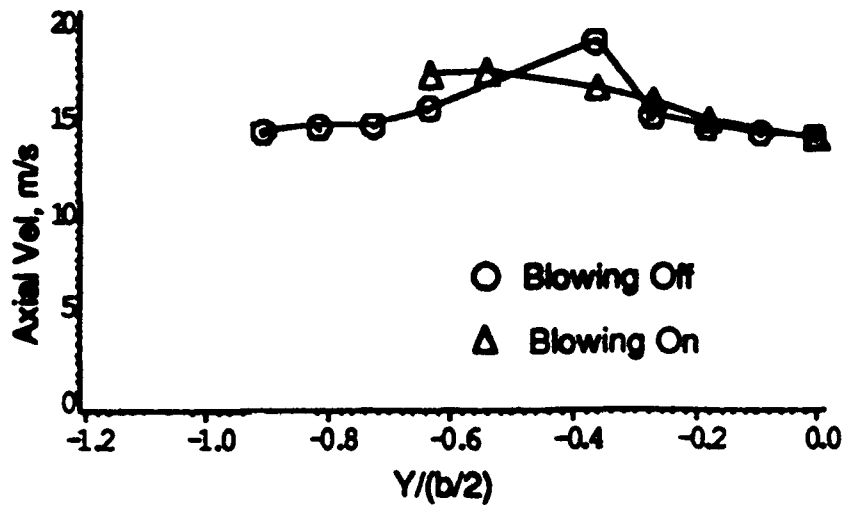

h) uw Reynolds stress versus spanwise locations, z/(b/2)=0.86

Figure 5.2.2   Continued

134
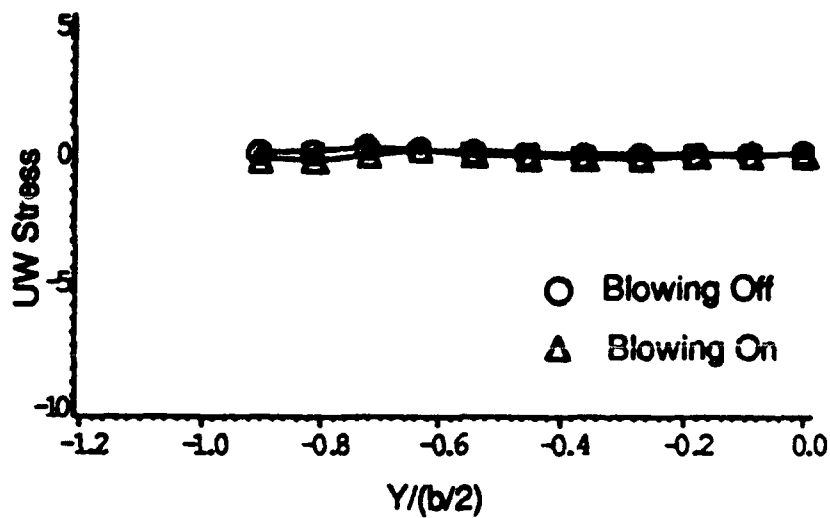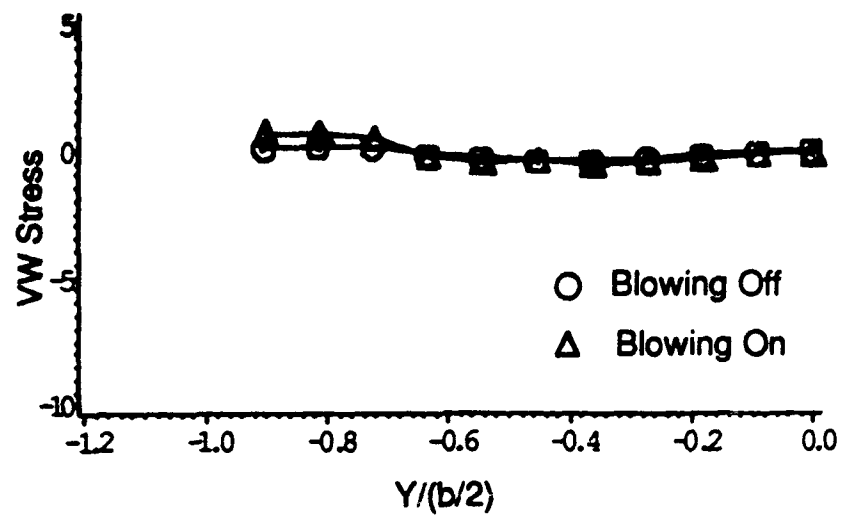
i) vw Reynolds stress versus spanwise locations, z/(b/2)=0.86

Figure 5.2.2   Concluded.
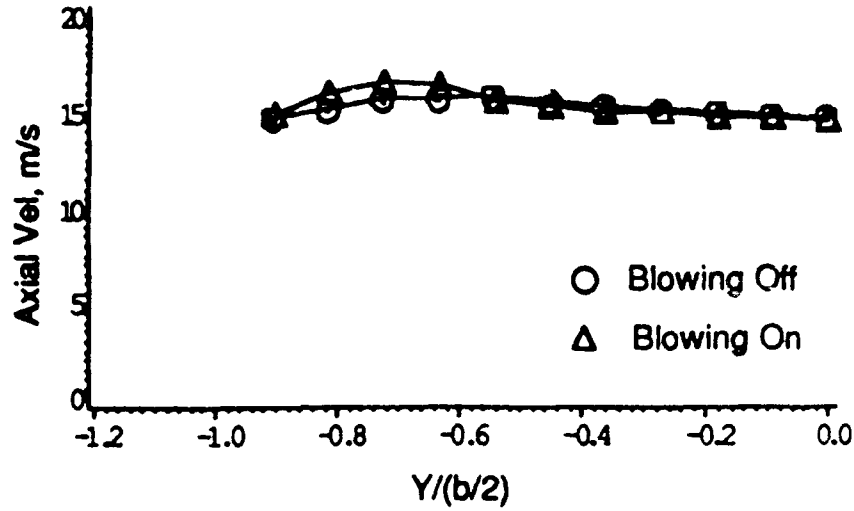
a) mean axial velocity versus spanwise locations, z/(b/2)=0.72
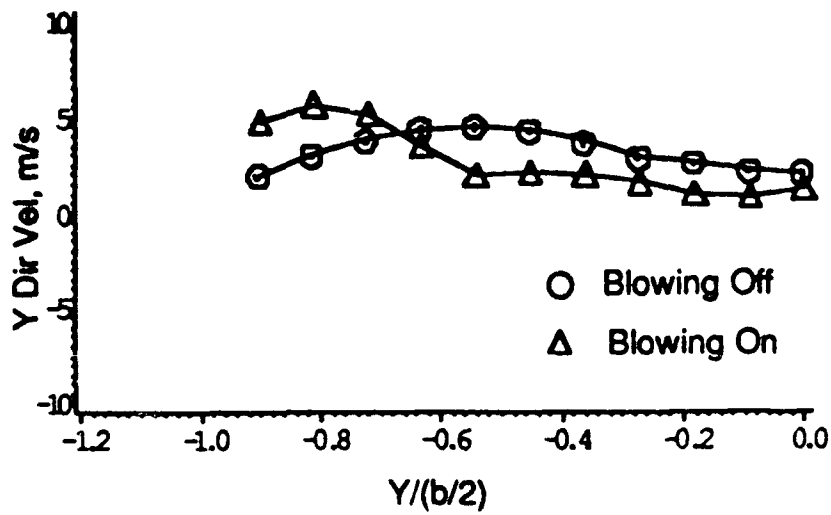
b) mean spanwise velocity versus spanwise locations, z/(b/2)=0.72

Figure 5.2.3   Mean Velocities, RMS Velocities, and Cross Correlations for No Blowing and for Blowing On with C_μ=0.016 as a Function of the Spanwise Locations at z/(b/2)=0.72.
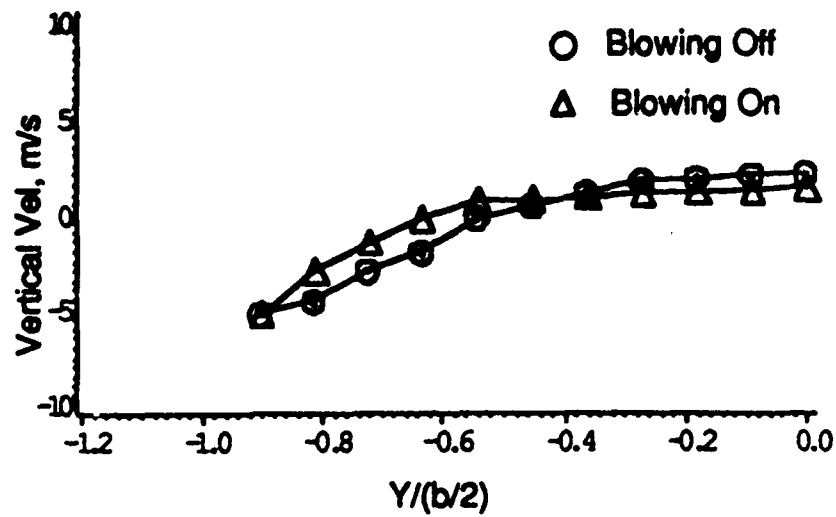
c) mean vertical velocity versus spanwise locations,
    z/(b/2)=0.72
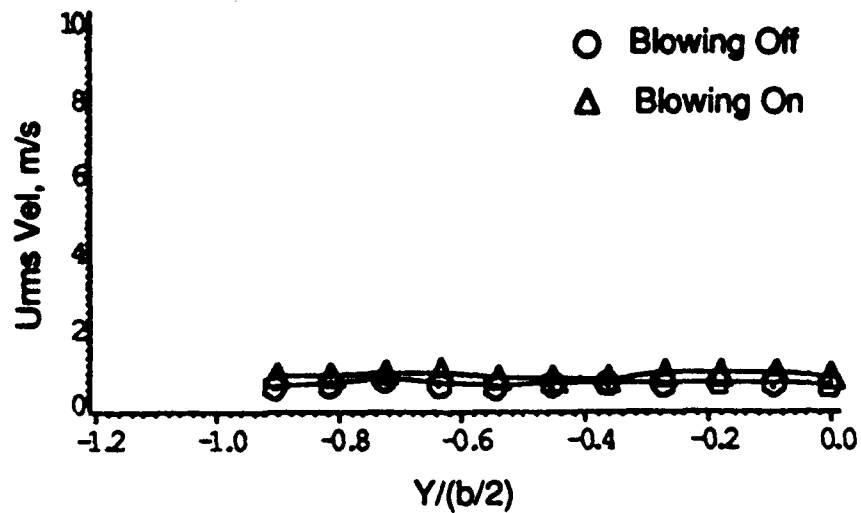
d) axial RMS velocity versus spanwise locations, z/(b/2)=0.72

Figure 5.2.3   Continued
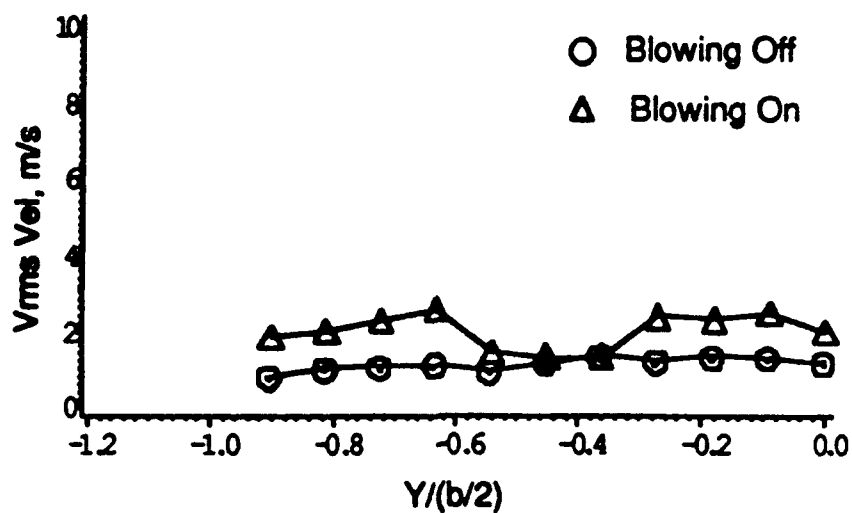
e) **spanwise RMS velocity versus spanwise locations,**
    z/(b/2)=0.72
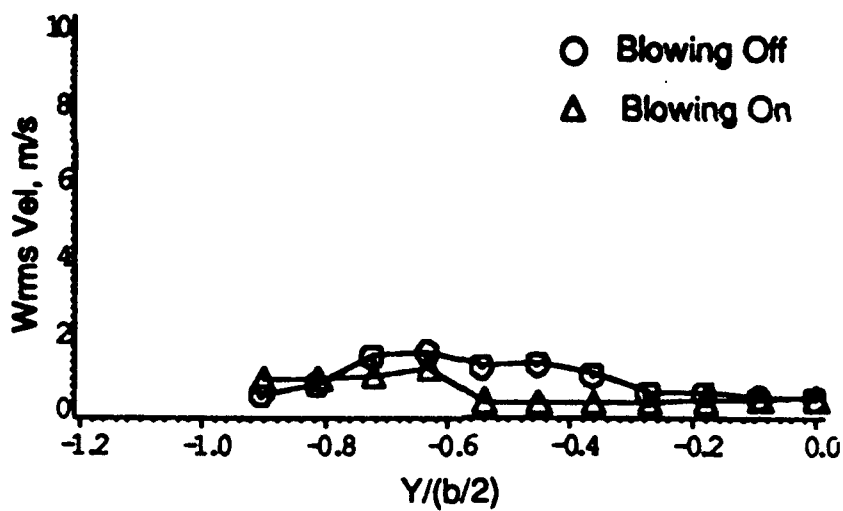
f) **vertical RMS velocity versus spanwise locations,**
    z/(b/2)=0.72

Figure 5.2.3   Continued

138
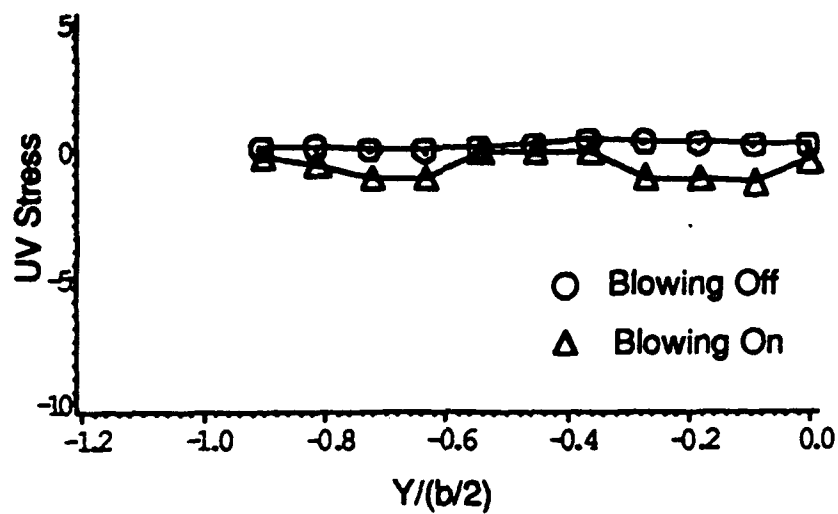
g)   uv Reynolds stress versus spanwise locations, z/(b/2)=0.72

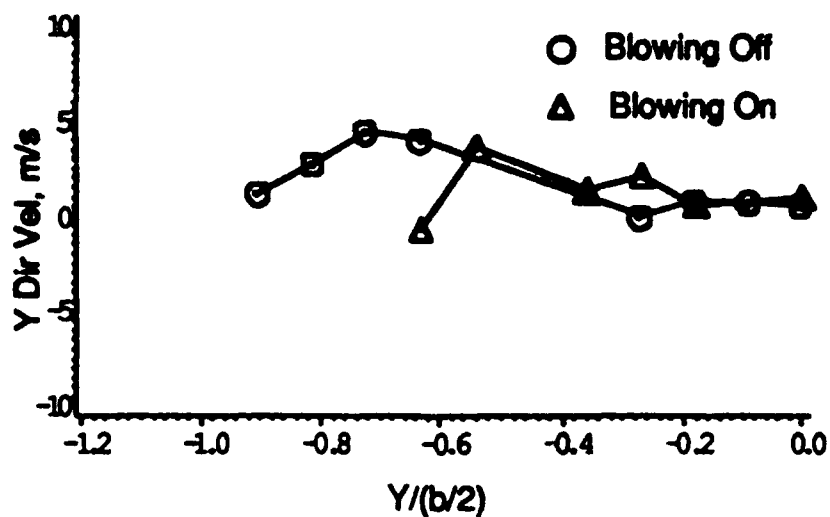h)   uw Reynolds stress versus spanwise locations, z/(b/2)=0.72
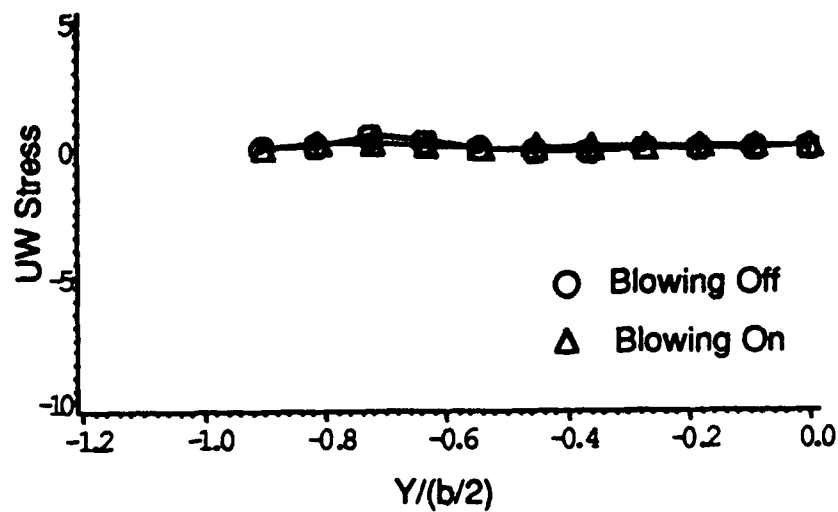
Figure 5.2.3   Continued
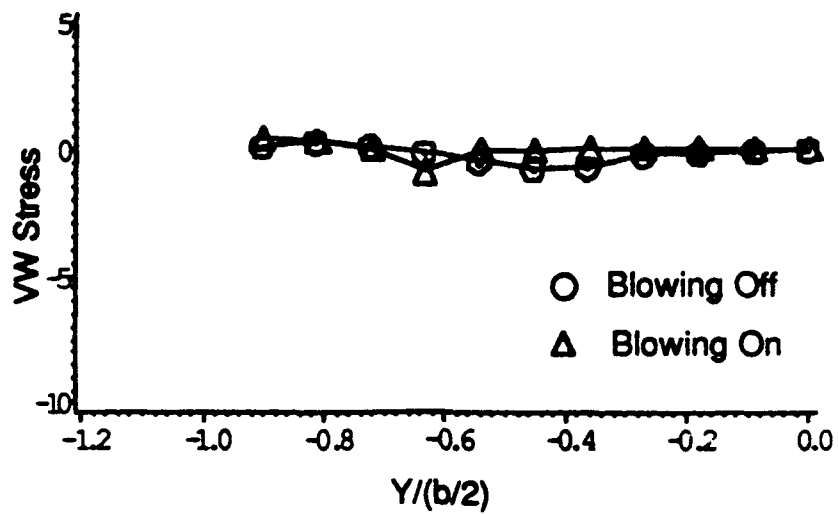
i)   vw Reynolds stress versus spanwise locations, z/(b/2)=0.72

Figure 5.2.3   Concluded.
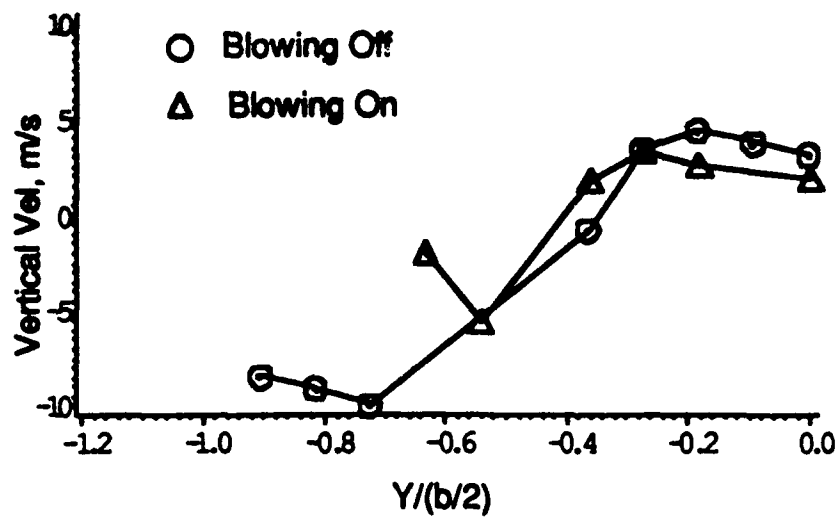
a)   mean axial velocity versus spanwise locations, z/(b/2)=0.57
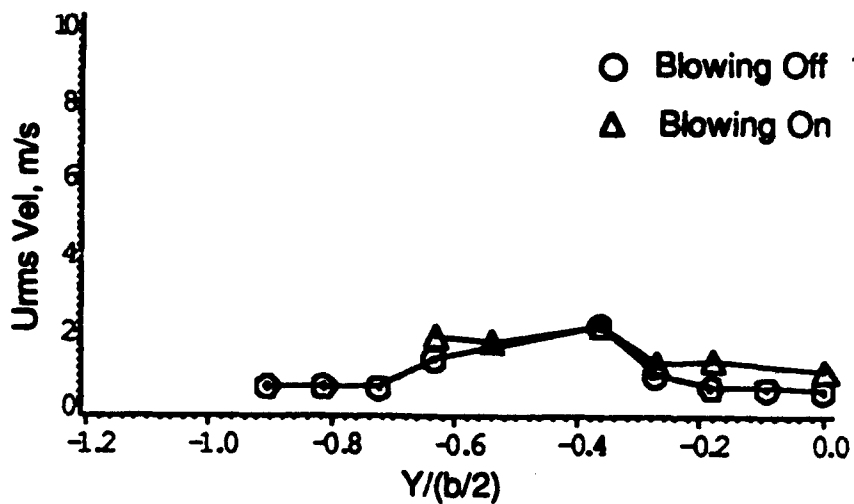

b)   mean spanwise velocity versus spanwise locations,
     z/(b/2)=0.57

Figure 5.2.4   Mean Velocities, RMS Velocities, and Cross
                Correlations for No Blowing and for Blowing On
                with C_μ=0.016 as a Function of the Spanwise
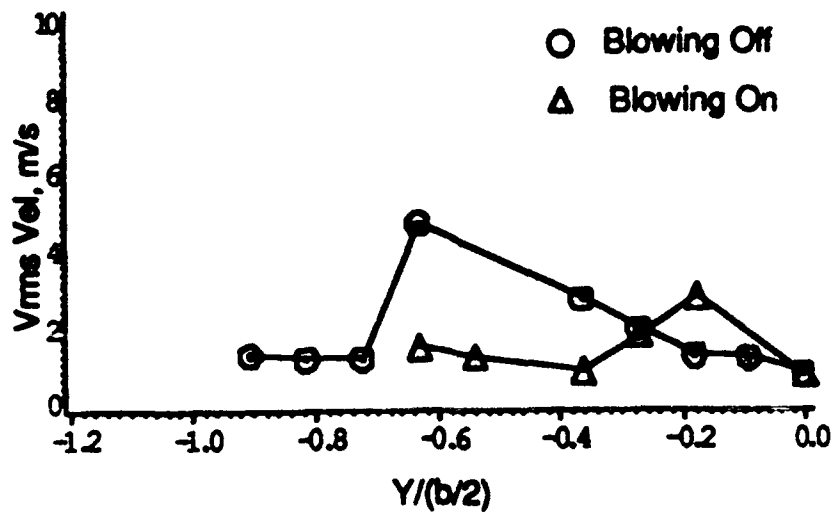   Locations at z/(b/2)=0.57.

141

c)   mean vertical velocity versus spanwise locations,
     z/(b/2)=0.57
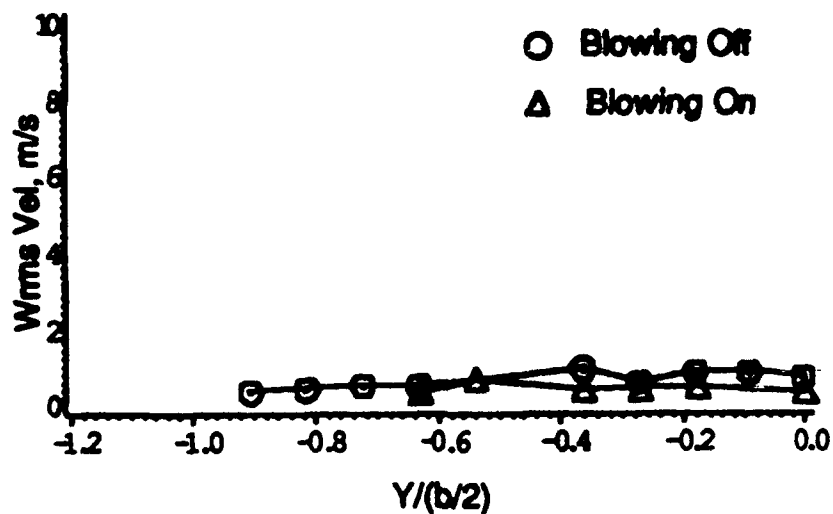

d)   axial RMS velocity versus spanwise locations, z/(b/2)=0.57
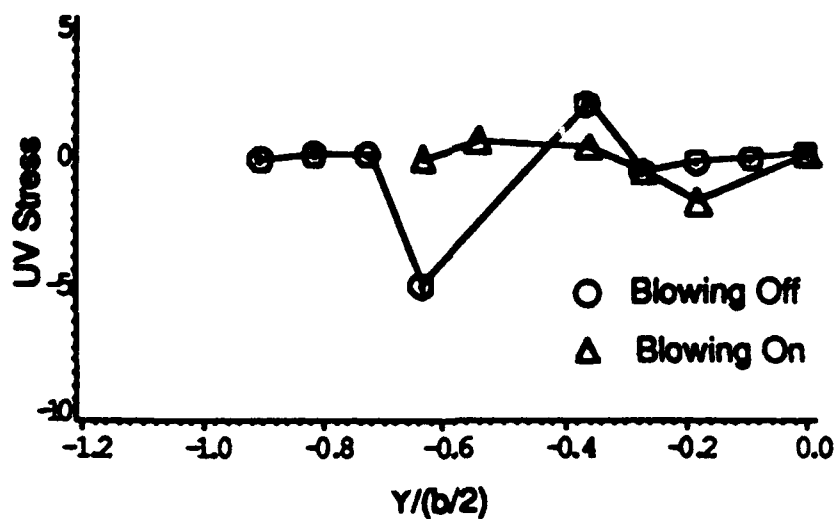
Figure 5.2.4   Continued

e)   spanwise RMS velocity versus spanwise locations,
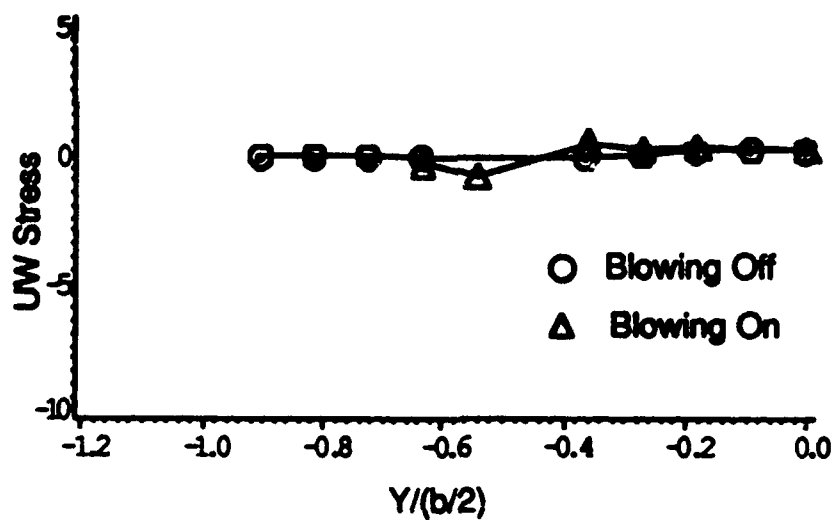   z/(b/2)=0.57

f)   vertical RMS velocity versus spanwise locations,
     z/(b/2)=0.57

Figure 5.2.4   Continued

143

g) uv Reynolds stress versus spanwise locations, z/(b/2)=0.57

h) uw Reynolds stress versus spanwise locations, z/(b/2)=0.57

Figure 5.2.4   Continued

144

i)   vw Reynolds stress versus spanwise locations, z/(b/2)=0.57

Figure 5.2.4   Concluded.

a)   mean axial velocity versus spanwise locations, z/(b/2)=0.43

b)   mean spanwise velocity versus spanwise locations,
     z/(b/2)=0.43

Figure 5.2.5   Mean Velocities, RMS Velocities, and Cross
                 Correlations for No Blowing and for Blowing On
                 with C_μ=0.016 as a Function of the Spanwise
                 Locations at z/(b/2)=0.43.

146

c) mean vertical velocity versus spanwise locations,
    z/(b/2)=0.43

d) axial RMS velocity versus spanwise locations, z/(b/2)=0.43

Figure 5.2.5   Continued

e) spanwise RMS velocity versus spanwise locations, z/(b/2)=0.43

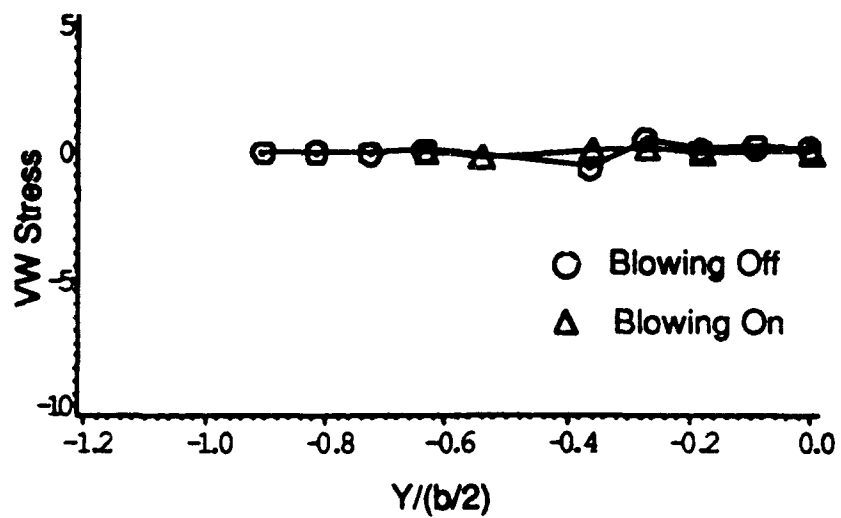f) vertical RMS velocity versus spanwise locations, z/(b/2)=0.43

Figure 5.2.5   Continued

148

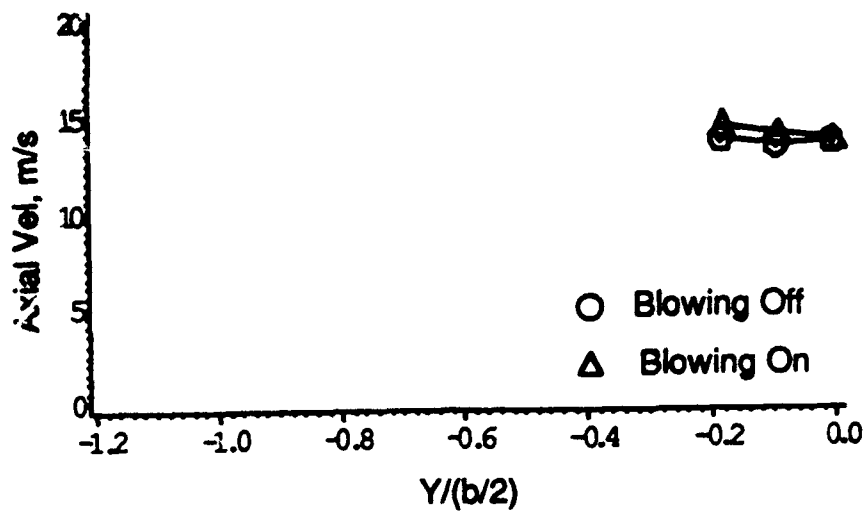g) uv Reynolds stress versus spanwise locations, z/(b/2)=0.43

h) uw Reynolds stress versus spanwise locations, z/(b/2)=0.43
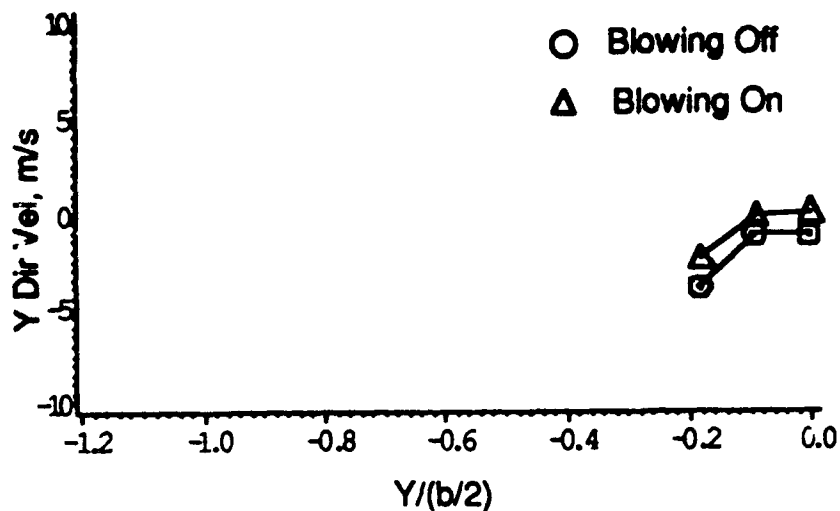
Figure 5.2.5   Continued

149

i)   vw Reynolds stress versus spanwise locations, z/(b/2)=0.43
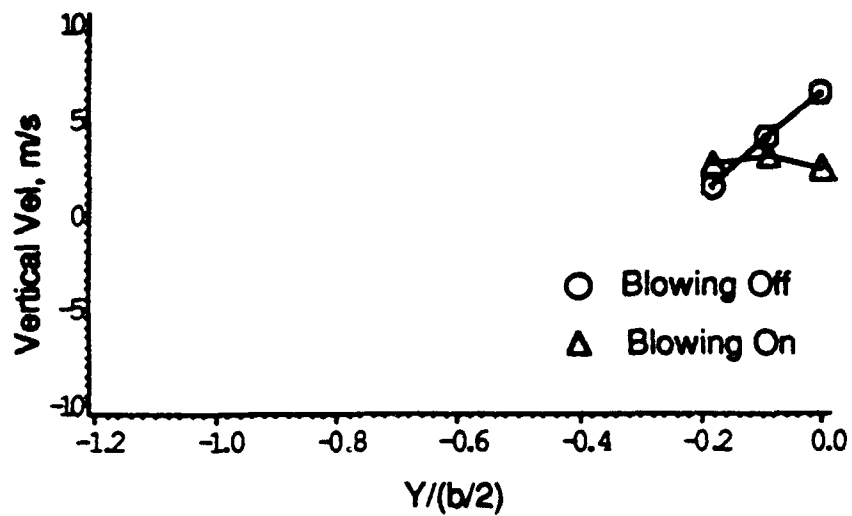
Figure 5.2.5   Concluded.

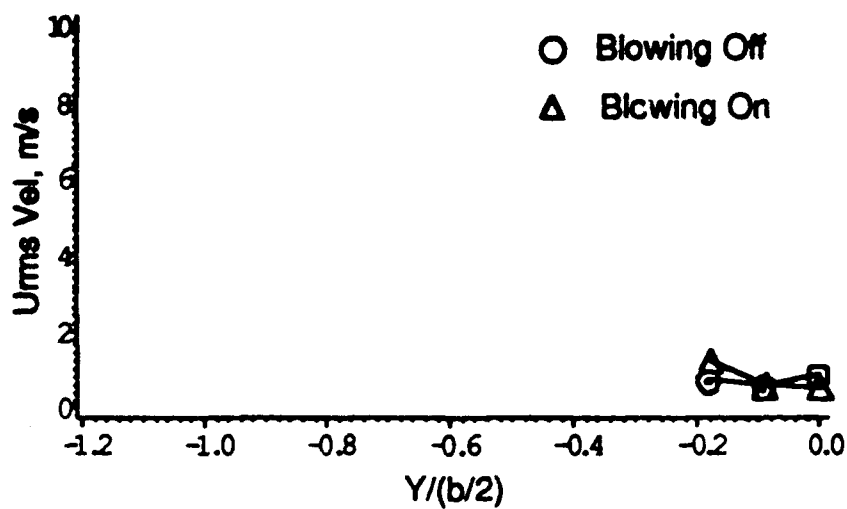a) mean axial velocity versus spanwise locations, z/(b/2)=0.29

b) mean spanwise velocity versus spanwise locations,
    z/(b/2)=0.29

Figure 5.2.6   Mean Velocities, RMS Velocities, and Cross
               Correlations for No Blowing and for Blowing On
               with C_μ=0.016 as a Function of the Spanwise
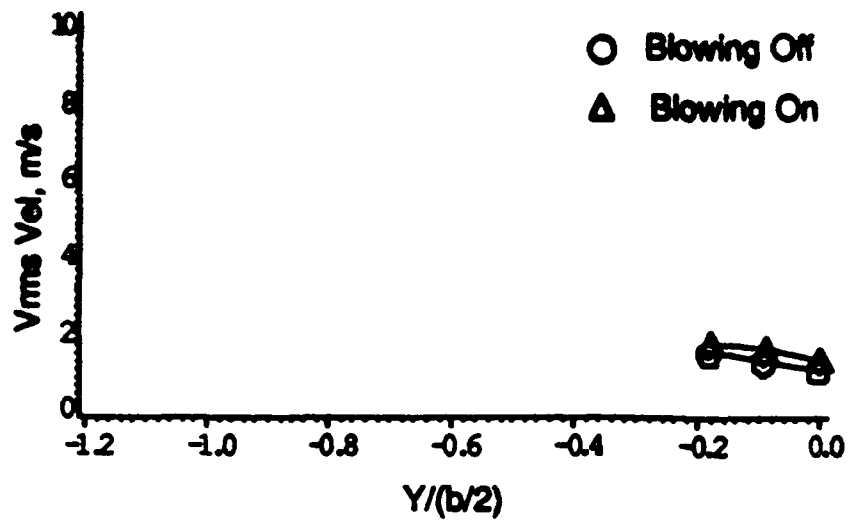   Locations at z/(b/2)=0.29.

151

c) mean vertical velocity versus spanwise locations,
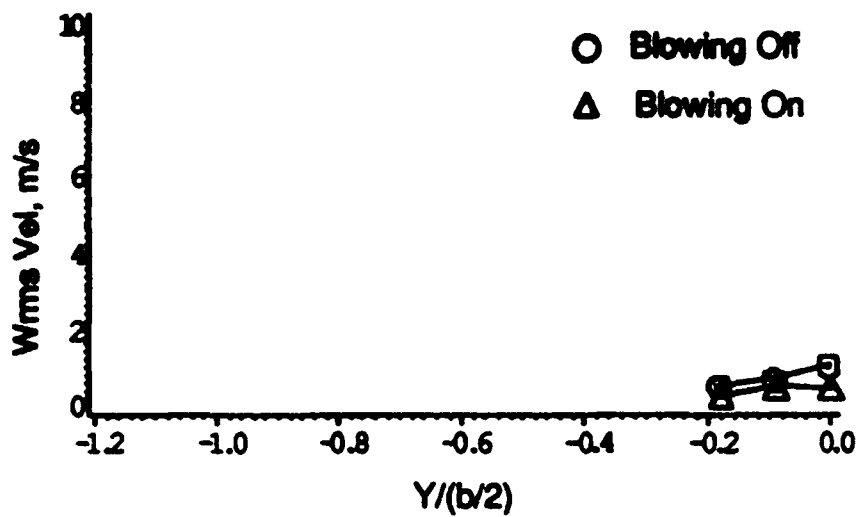   z/(b/2)=0.29

d) axial RMS velocity versus spanwise locations, z/(b/2)=0.29
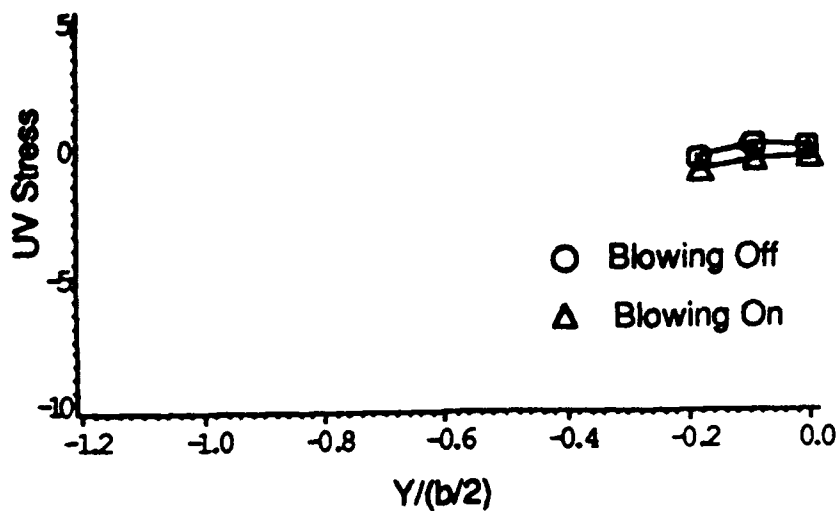
Figure 5.2.6   Continued

152

e)   spanwise RMS velocity versus spanwise locations,
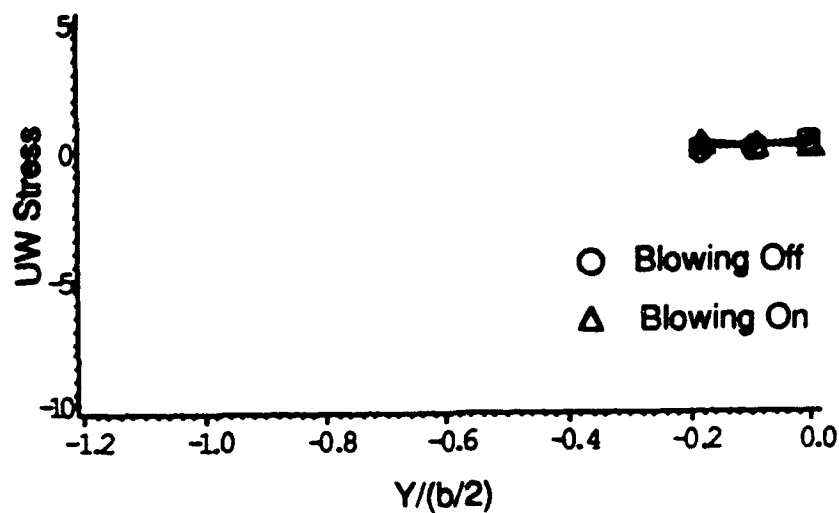   z/(b/2)=0.29

f)   vertical RMS velocity versus spanwise locations,
     z/(b/2)=0.29

Figure 5.2.6   Continued

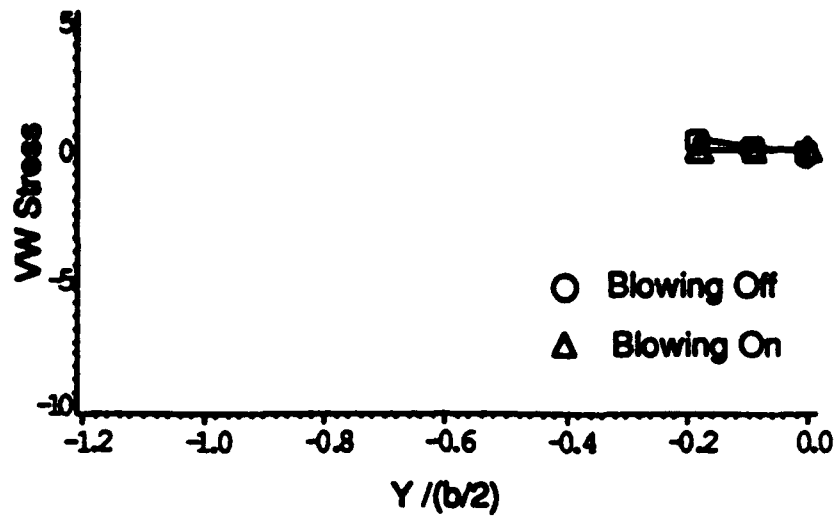g) uv Reynolds stress versus spanwise locations, $z/(b/2)=0.29$

h) uw Reynolds stress versus spanwise locations, $z/(b/2)=0.29$

Figure 5.2.6   Continued

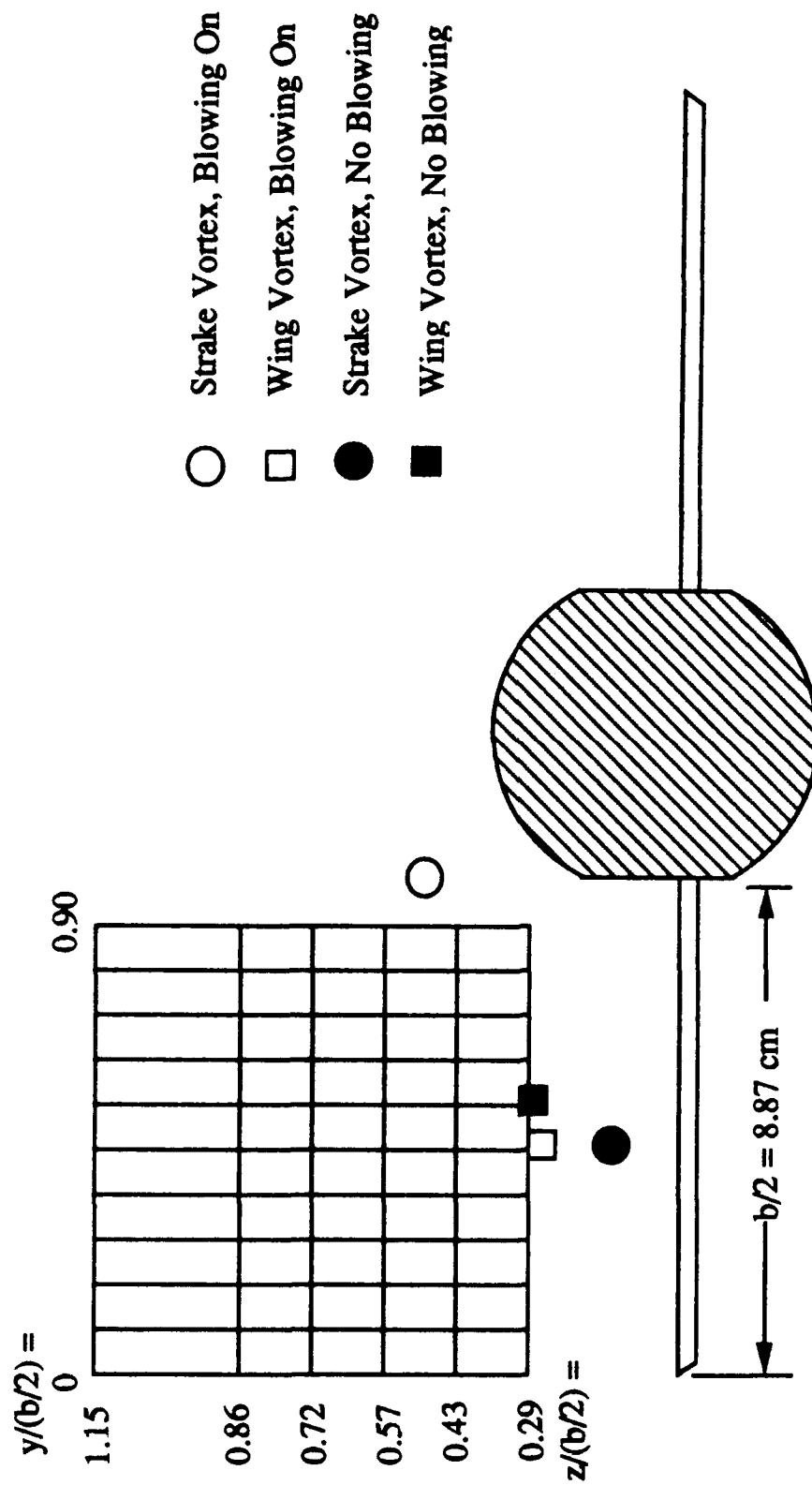i) vw Reynolds stress versus spanwise locations, z/(b/2)=0.29

Figure 5.2.6   Concluded.

Figure 5.2.7 Location of Laser Doppler Velocimetry Measurement Grid and Vortex Core Locations at X/C = 0.45, α = 20°, as Viewed from Downstream, Showing Local Exposed Semispan.

APPENDIX A: PRINCIPLES OF LASER DOPPLER ANEMOMETRY

This section provides a brief overview of the basic principles of laser Doppler anemometry, a more comprehensive view of this subject can be found in Durst, et al (30). Laser anemometers are non-contact optical instruments used for the investigation of fluid flow velocity fields in gases and liquids. Laser anemometers offer additional unique advantages in comparison with other fluid flow instrumentation, such as no calibration, a well-defined directional response, high spatial and temporal resolution, and multi-component bi-directional measurement capability.

Special properties of the gas ion laser make it well suited for measurements of many mechanical properties. Among these special properties of the gas laser are spatial and temporal coherence. The temporal coherence describes the period of time during which the laser frequency remains constant. The distance over which a laser stays in constant phase with itself is known as the coherence length. Spatial coherence describes the ability of the laser light field to form interference fringes in space. As a result of the spatial coherence of the gas laser, an intersection of two laser beams at an angle in the flow field yields a pattern of plane interference fringes at the beam crossing (called the measuring volume). The fringes are areas of maximum and minimum light intensity caused by constructive and destructive interference of the laser beam

wavefronts. The measuring volume has regions of low light intensity and regions of high light intensity, and the distance between the fringes is constant and is given by

$$d_f = \lambda / (2\sin\phi/2) \qquad\qquad (A.1.1)$$

where λ = wavelength of laser light

$\phi/2$ = half angle between beams

d_f = fringe spacing

See Figure A.1.1 for a sketch of the fringe patterns of the measuring volume.

The measuring volume created by the two coherent and monochromatic laser beams has the shape of an ellipsoid. For reference purposes, the edges of the ellipsoid are defined as the point where the amplitude of the Doppler signal is $1/e^2$ of its centerline value. The dimensions of the ellipsoidal measuring volume are:

$$d_e\text{-}2 = 4 \ \lambda \ f/(\pi \ D_e\text{-}2) \qquad\qquad (A.1.2)$$

$$d_m = d_e\text{-}2/\cos(\phi/2) \qquad\qquad (A.1.3)$$

$$l_m = d_e\text{-}2/\sin(\phi/2) \qquad\qquad (A.1.4)$$

where   f = focal length of transmitting lens

$D_e\text{-}2$ = diameter of laser beam entering transmitting lens

Particles moving through the fringe pattern within the measuring volume create a scattered light intensity variation. Figure A.1.2 shows a typical laser Doppler signal. The scattered light intensity variation is of a Gaussian shape and the phase of the scattered light waves depend on the particle velocity and of the direction of the scattered light waves. By

collecting the scattered light with a photodetector, the light intensity variation is converted by the photodetector into a voltage signal with a varying amplitude. The velocity of the particle can be determined by using the resulting Doppler frequency of the scattered light, f_D, and the fringe spacing by using the following relationship:

$$V = f_D d_f \qquad (A.1.5)$$

This relationship assumes a properly designed optical system where the laser beam waists are exactly at the crossing point.

One weakness of such a system is that the system cannot distinguish reverse flow from forward flow. This ambiguity is remedied by using a Bragg cell to introduce a fixed frequency shift between the two laser beams. Optical and electronic frequency shifting are used for their inherent ability to shift the frequency up or down as desired. This variable shifting of the frequency is convenient for the measurement of highly fluctuating and reversing flows characteristic of highly turbulent flow fields. Variable frequency shifting is done by first superimposing a constant frequency shift on one of the incident laser beams prior to the crossing with the other laser beam in the measuring volume. The photomultiplier output signal is then mixed with a variable shift generator signal and fed to the counter processor. With this technique, it is possible to obtain a constant and linear relationship between the detected frequency and the velocity from one sense of velocity through zero into the opposite sense of velocity.

Shifted Beam

Direction of Moving Fringes

1/2 θ

θ
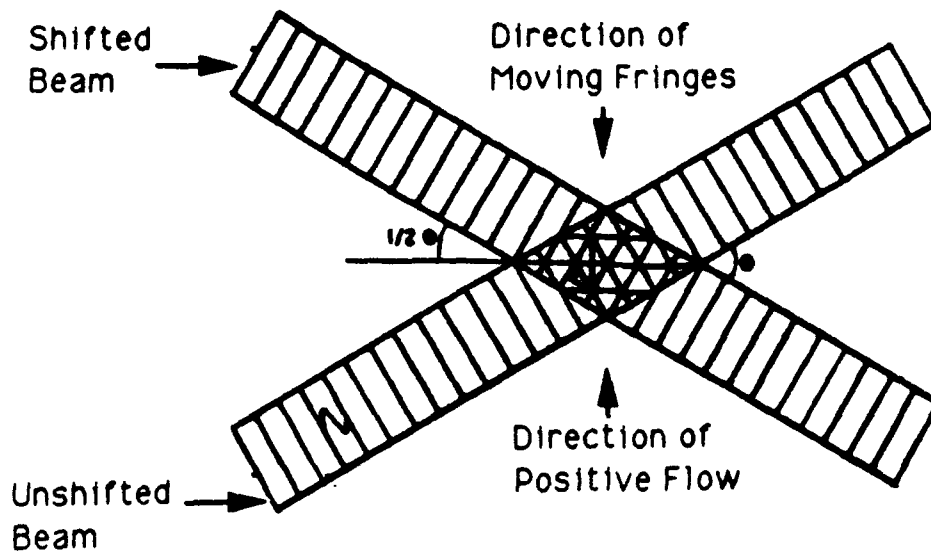
Direction of Positive Flow

Unshifted Beam

Figure A.1.1 Fringe pattern within the measuring volume at the intersection of two laser beams.
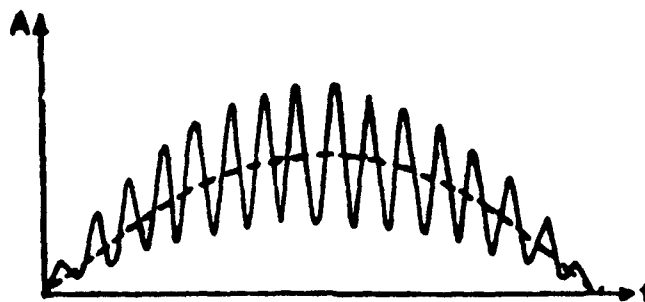

Figure A.1.2 Typical laser Doppler signal created as a particle passes through measuring volume.

APPENDIX B: LIST OF EQUIPMENT

Laser
 Spectra Physics
 Model 2020
Laser Power Supply
 Spectra Physics
 Model 2560

Optics
 Dantec
 55X Modular Optics
 Model 55N10 Bragg Cell Frequency Shifter
 Model X27 Beam Splitter
 Model X32 Beam Displacer
 Model X30 Back Scatter Section
 Model X08 Photomultiplier Section
 Model X31 Pinhole Section
 Model X32 Beam Translator
 Model X12 Beam Expander

LDA Counter Processor
 Dantec
 Model 55L90A

Buffer Interface
 DANTEC
 Model 57G20

Coincidence Filter
 DANTEC
 Model 57G149

PDP 11/23
 Digital Equipment Corporation
 Model 11E23-FE

Rotameters
 Dwyer
 Series RMB, 0 - 0.57 cubic m/hr (0 - 20 SCFH)
 Series RMC, 0 - 2.83 cubic m/hr (0 - 100 SCFH)

Smoke Generator
 Rosco Laboratories
 Model 1500

Smoke Simulation Fluid
 Rosco Laboratories

Video Camera
 Olympus
 Model VX-303

Video Cassette Recorder
 Olympus
 Model VC-103

Power Supply
 Calrad
 Model 45-738

35mm Camera
 Olympus

VITA

Robert Allen Roach was born in Takoma Park, Maryland on March 3, 1966 to Robert L. and Carol S. Roach. Upon moving to Weston, West Virginia in 1972, he was educated in the public school system and graduated from Lewis County High School in 1984. After graduation he attended West Virginia University where he obtained the degree of Bachelor of Science in Aerospace Engineering in May, 1988, and completed the requirements for the degree of Master of Science in Aerospace Engineering in May, 1991. He is currently pursuing a Ph. D. in Aerospace Engineering at Virginia Polytechnic Institute and State University located in Blacksburg, Virginia, with an anticipated graduation date in 1993.